The Evolution of Craton Margin Geometry Through Time

by

Deirdre Mallyon

A thesis submitted in partial fulfillment of the requirements for the degree of

Master of Science

in

Geophysics

Department of Physics
University of Alberta

Abstract

In western Canada, the Archean-aged cratonic core of the North American continent is flanked on its western edge by the Cordillera, which forms the back arc region of the Cascadia subduction zone. The boundary between these two geologic provinces is expressed at the surface by a system of NNW-SSE trending strike-slip faults, known as the Rocky Mountain Trench and Tintina Fault. Striking contrasts are observed between the craton in the east and Cordillera in the west; surface heat flow increases from an average of ~45 mW/m^2 to ~75 mW/m^2, lithosphere thickness decreases from ~60 km to ~250 km and decreases in seismic shear wave velocities of ~80 m/s are observed. Interestingly, the lateral transition between these contrasts in the lithosphere is estimated to occur over lateral distances of less than ~100 km.

In addition to these observations, new geophysical data collected in western Canada suggests that the geometry of the craton margin shows significant along-strike (i.e. north-south) variation; transitioning from dipping eastward below the continental interior, to dipping westward below the back arc, with a vertical transition occurring between ~52 and 53°N. Motivated by these new observations, the present study uses thermally-mechanically coupled geodynamic models in order to: 1) determine the necessary rheological and density structure of the craton lithosphere that facilitates/maintains vertical and west dipping craton margin geometries; 2) investigate the influence of geodynamic processes such as gravitational instability, large-scale mantle flow and crustal shortening on the evolution of craton margin geometry; and 3) determine whether vertical and westward dipping craton margin geometries are transient over times scales of tens of millions of years, or long-lived features that persist hundreds of millions of years.

The results of the numerical modelling experiments show that vertical and west-dipping craton margin geometries can be both produced and maintained; however, the craton mantle lithosphere must be strong and buoyant relative to the surrounding mantle. Vertical structures are observed when the relative effective viscosity is increased by a factor of 15 or more and the compositional density is reduced by ~10-20 kg/m^3, whereas west-dipping geometries are observed when relative effective viscosity is increased by a factor of 5 or more, and when compositional density is reduced by ~30-40 kg/m^3. The influence of large-scale mantle flow on the craton margin is strongly dependent on the direction of flow compared to the influence of flow velocity. Vertical and west-dipping craton margin geometries are enhanced when flow is directed from the interior of the craton toward its outer margin. Conversely, flow that is directed from the back arc region toward the craton enhances erosion of the craton margin, resulting in craton margins that dip toward the interior of the continent. Vertical craton margins are readily maintained in crustal shortening experiments; however, west-dipping craton margins are largely absent. Overall, the results of this study suggest that vertical and west-dipping craton margins are both transient and long-lived features.

Acknowledgements

I would like to thank my supervisors, Dr. Claire Currie and Dr. Doug Schmitt, for their unwavering support, guidance and patience throughout the last two years. I have learned more from you than I could ever have imagined, and I am truly grateful to have had the privilege to work with you. To my supervisory committee, Dr. Jeff Gu and Dr. Richard Marchand; thank you for taking the time to review my work. I sincerely value the unique perspectives you brought to my work. Thank you to Yunfeng Chen; your seismic tomography models provided this inspiration for this study, and I don't know how I would have survived GMT without your wise and generous council.

Alasdair, you believed in me when I couldn't believe in myself. I could never have made it through this without you; your love and support kept me sane and your superior culinary skills kept me alive. Thank you to my family, who were and always have been there for me, I wouldn't be who I am, or where I am if it weren't for you. To my office mates and fellow U of A students, thank you for two years of wonderful friendship and support. In particular I would like to thank Olivia for being a much needed shoulder to lean on and a brilliant brain to pick, I feel sincerely fortunate to have you in my corner.

Table of Contents

List of Tables

List of Figures

Chapter 1: Introduction

1.1 Structure of the Continental Lithosphere in Western Canada

Continental lithosphere is an amalgamation of blocks with differing ages, composition and structure that have been sutured together by, and have survived, repeated episodes of deformation over billions of years. The stable interior regions of continents are referred to as cratons, and are characterized by lithosphere that is 1 Ga or older, and has a thickness of ~100 to 200 km, or more. In contrast, oceanic lithosphere is relatively simple; it is created by seafloor spreading at mid-ocean ridges and is then subducted back into the mantle, reaching a maximum age a few hundred million years and a maximum thickness of ~7 km. Geoscientists have long sought to explain why cratonic material survives over billions of years, while oceanic lithosphere is continually recycled at subduction zones. In many regions, cratons are surrounded by younger belts of hotter, and therefore weaker, lithosphere referred to as mobile belts [*Hyndman et al.*, 2005]. These mobile belts act as buffers by concentrating deformation, consequently shielding the craton from plate boundary forces [*Moresi and Solomatov*, 1998; *Lenardic et al.*, 2000; *Hyndman et al.*, 2005]. Lithosphere that is both thin and hot are key characteristics shared among mobile belts, and are attributed to either their recent or current or position in a continental back arc environment [*Hyndman et al.*, 2005; *Currie and Hyndman*, 2006].

This thesis focuses on geodynamic processes that occur at the margin of the cratonic lithosphere in western Canada. Here, the western edge of the Archean-to Proterozoic-aged North American craton is flanked along its western edge by the Cordillera, a Paleozoic mobile belt. Based on seismic data from western Canada, it is estimated that the craton lithosphere is ~250 km thick, compared to the Cordillera lithosphere which is estimated to be only ~60 km thick

[*Hammer et al.*, 2010; *Kao et al.*, 2013; *Bao et al.*, 2014; *Gu and Shen*, 2015]. However, as illustrated in Figure 1.1, given that its crust is ~35 km thick, the surface elevation of the Cordillera is anomalously high. This anomalous elevation is attributed to a high thermal gradient as inferred from slow seismic velocities and high surface heat flow (~75 mW/m^2 compared to ~45 mW/m^2 in the craton) [*Hyndman and Lewis*, 1999; *Hammer and Clowes*, 2007].

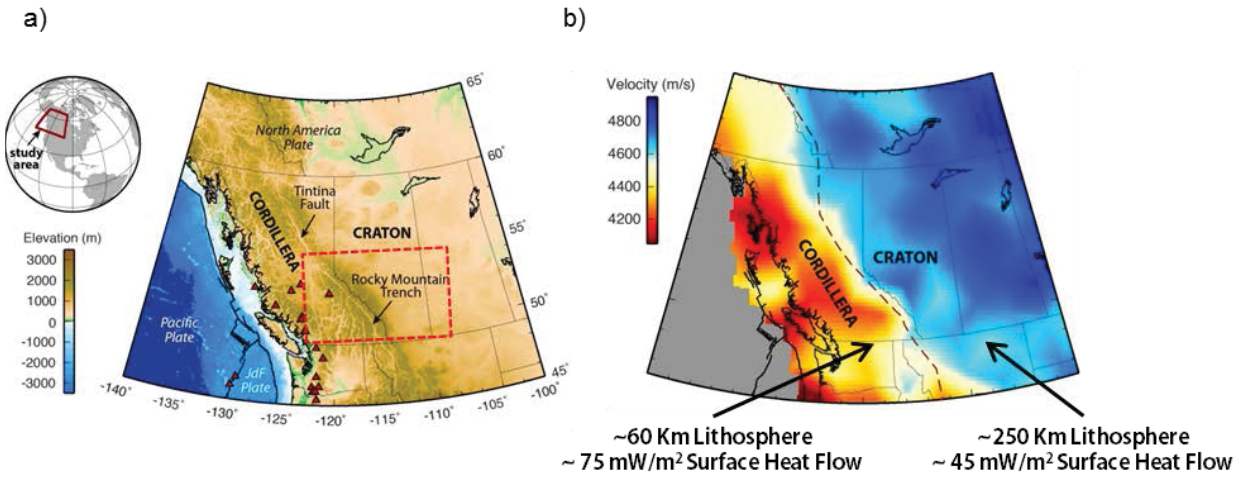

Figure 1.1: a) Topographic map showing the relative surface elevation between the Cordillera and North American craton in western Canada and the surface expressions of the Rocky Mountain Trench and Tintina Fault, which are thought to form the boundary between the Cordillera and craton lithosphere. The red dashed box shows the region modelled in this study. b) A plot of shear wave velocities at 90 km depth showing the increase in velocity that occurs at the Cordillera-craton boundary. Note that in addition to increased shear wave speeds, increased lithosphere thickness and decreased surface heat flow are also observed across the boundary.

The surface expression of the boundary between the Cordillera and the North American craton is shown in Figure 1.1a. It is defined by the Tintina Fault and the Rocky Mountain Trench, two major dextral strike slip faults that have a combined length of more than 2600 km [*Wyld et al.*, 2006]. Remarkably sharp contrasts in various geophysical a observations, including seismic velocities, surface heat flow and lithosphere thickness are observed across this boundary, occurring over lateral distances of ~100 km [*Bedle and Van Der Lee*, 2009; *Mercier et al.*, 2009; *Bao et al.*, 2014]. Thus, a significant change in lithosphere thickness occurs at the Cordillera-craton boundary.

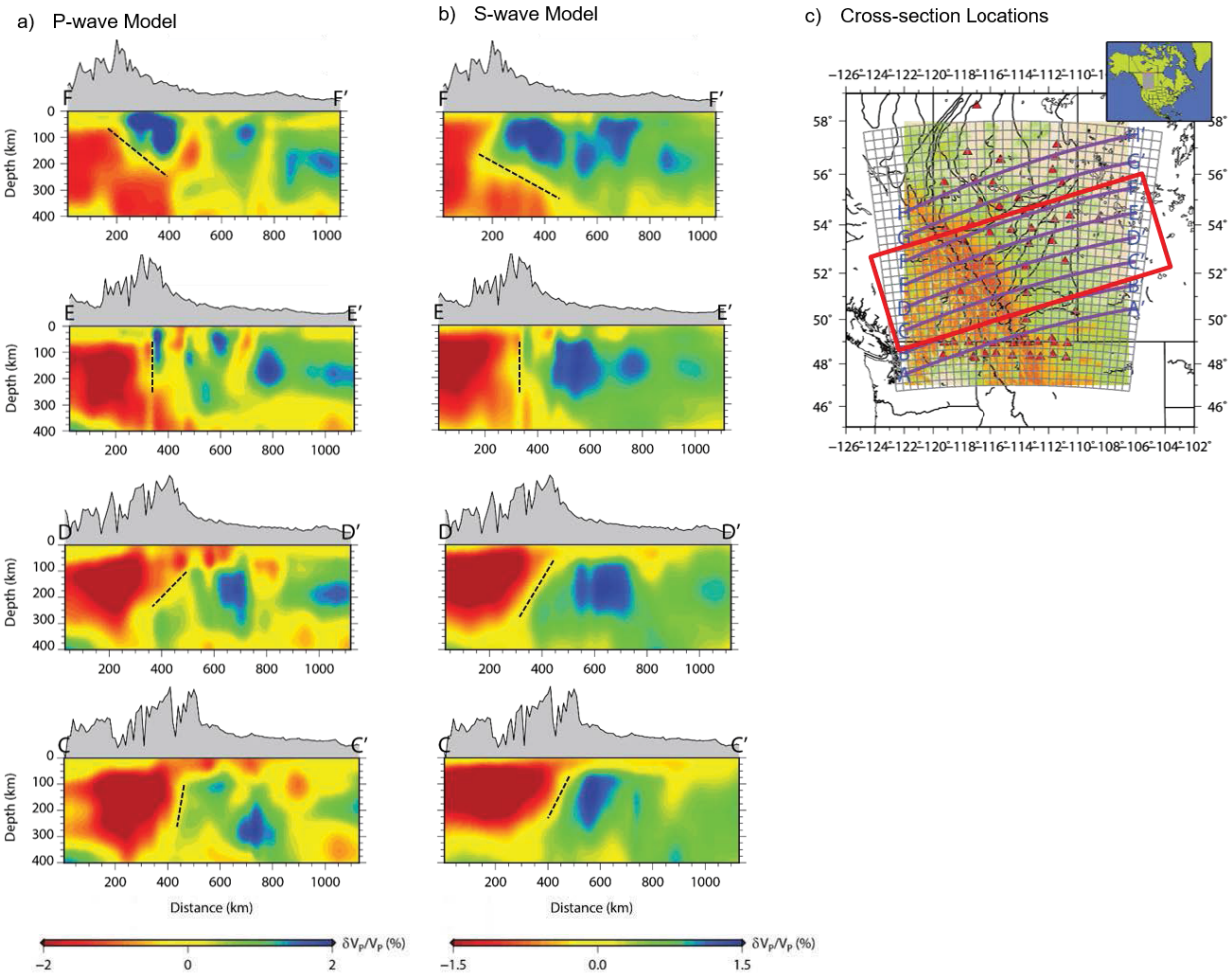

Figure 1.2: a) Cross-sections through the S-wave tomography models of *Chen et al.* [submitted manuscript 2016]. Warm colours denote regions of low relative velocities, and cool colours denote regions of high relative velocities. The black dashed line is added to show the interpreted dip of the craton margin. b) same as in a) but for the P-wave velocity model. c) regional map showing cross-section locations in a) and b).

New body wave seismic tomography models from *Chen et al.* [submitted manuscript, 2016] use teleseismic events from 63 recording stations in western Canada to image the craton edge in western Canada. Their models suggest that the geometry of the craton margin shows significant along-strike variation. North of ~53°N, profile F-F' in Figure 1.2a and 1.2b shows a zone of relatively high velocity perturbation lying immediately adjacent to a low velocity perturbation that dips steeply eastward (i.e. below the interior of the continent) at an angle of approximately 65-75°. South of ~51°N this low velocity perturbation dips westward toward the Cordillera, as shown in profiles C-C' and D-D', at an angle of ~ 95-105° or more (relative to an

eastward orientation). The transition between the observed eastward and westward dipping low velocity perturbations occurs between 52-53°N, where the craton margin is approximately vertical. Taken in combination with surface elevation and heat flow data from western Canada, these fast and slow velocity perturbations are interpreted by *Chen et al.* [submitted manuscript, 2016] as the craton mantle lithosphere and hot asthenospheric material underlying the Cordillera lithosphere, respectively. Interestingly, this westward dipping low-velocity structure imaged along the southern segment of the craton margin (Figure 1.2a and b, profiles C-C' and D-D') has been previously observed in seismic tomography models from other authors [*Mercier et al.*, 2009; *Bao et al.*, 2014].

Electrical conductivity models of *Rippe et al.* [2013], shown in Figure 1.3, were constructed using long period magnetotelluric data. The models record a sharp lateral transition between high conductivity (~1×10^{-2} S/m) below the Cordillera and low conductivity in the adjacent cratonic mantle lithosphere (~1×10^{-3} S/m). The structure of the low conductivity region associated with the craton is sub-vertical in the northern profile (Figure 1.3a), which is located at a latitude of ~53°N. In the southern profile (Figure 1.3c) the low conductivity structure dips westward (i.e. below the Cordillera) at a latitude of ~51°N. Electrical conductivity is sensitive to temperature, compositional changes as well as the presence of fluids or partial melt. *Rippe et al.* [2013] interpret the high electrical conductivity observed below the Cordillera as requiring both high temperatures, and the presence of olivine that is ~50 to 100% saturated with hydrogen ions or ~4% partial melt. Agreement between models from these two independent geophysical methods concerning the presence of vertical and west-dipping structures below western Canada supports the interpretation from *Chen et al.* [submitted manuscript, 2016] of along-strike variation of the geometry of the craton margin.

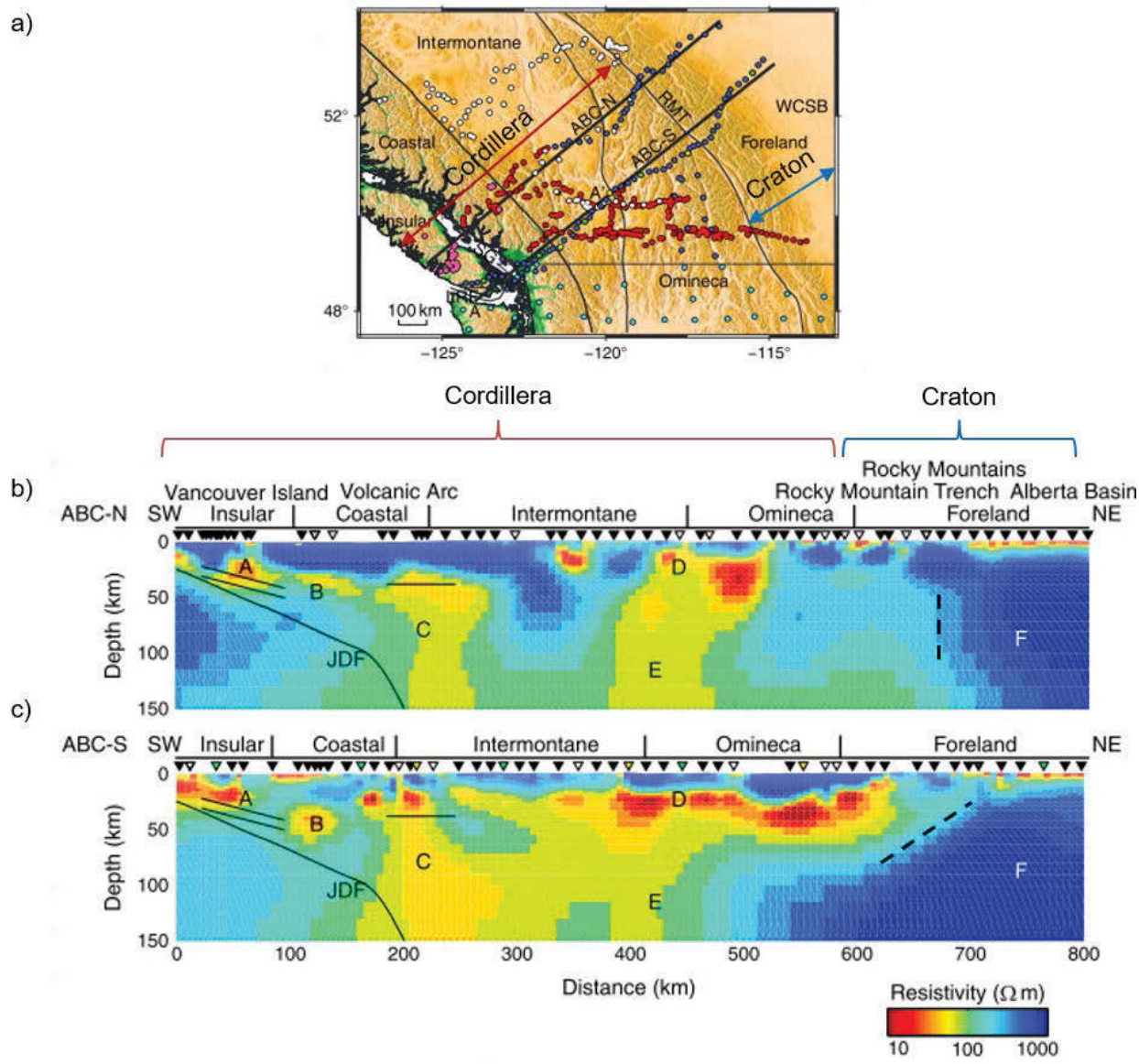

Figure 1.3: a) Locations of cross-sections for the electrical conductivity models of *Rippe et al.* [2013]. b) Northern cross-section through the electrical conductivity models of *Rippe et al.* [2013] showing the sub-vertical conductivity structure of the craton margin. c) Same as in b) but for the southern profile, showing a change to a westward-dipping conductivity structure at the craton margin. Note that a dashed black line is used in a) and b) to emphasize the conductivity structure at the craton margin. Modified from *Rippe et al.* [2013].

1.2 Previous Modelling Studies

The influence of lateral contrasts in lithosphere thickness, and resultant horizontal temperature gradients, has been explored in previous geodynamic modelling studies. However, models which explicitly focus on changes in the geometry of craton margins through time in

response to dynamic processes, such as large-scale mantle flow and crustal shortening are largely absent from the literature. Given below is a brief description of five numerical modelling studies that consider lateral contrasts in rheological and thermal regimes by incorporating a step in the lithosphere. This is followed by a discussion of how these studies differ from the present one.

Tomographic seismic velocity models from the central and northeastern regions of the European continent suggest 4% and 6% lateral increases in relative seismic velocity between the lithosphere of the Sorgenfrei-Tornquist Zone (STZ) and the European craton for P- and S-wave velocities, respectively. This lateral seismic velocity contrast is observed at depths between 100 km and 250 km, and occurs over a lateral distance on the order of tens of kilometers [*Hieronymus et al.*, 2007; and references therein]. *Hieronymus et al.* [2007] constructed finite element models of a 150 km step in the lithosphere, representative of observations from the STZ, in order to determine whether mantle convection in the presence of a sharp lateral temperature contrast can adequately explain the observed contrast in seismic velocities. In their models, *Hieronymus et al.* [2007] assigned a pyrolite rheology to the sub-lithospheric mantle, while a harzburgite rheology was used for the entire mantle lithosphere. However, despite exclusion of rheologically distinct crust, calculated temperature gradients used in the models include crustal sources of heat production [*Hieronymus et al.*, 2007]. Thermal fields resulting from the models were converted to seismic velocities, and compared with observations from seismic tomography models.

The results of the models suggest that the observed contrast in seismic velocity could only be reproduced by models which incorporated both mantle convection and a compositional contrast between the mantle lithosphere and surrounding sub-lithospheric mantle [*Hieronymus et al.*, 2007]. *Hieronymus et al.* [2007] attributed the necessity of a rheologically distinct mantle

lithosphere in their models to a required contrast in relative viscosity between the mantle lithosphere and surrounding mantle, as opposed to differences in chemical composition between pyrolite and harzburgite, which had a comparatively minor effect on seismic velocity. For example, an 8% S-wave velocity contrast was calculated for models that incorporated the effects of both mantle convection and a viscosity contrast between the mantle lithosphere and sub-lithospheric mantle, compared to a contrast of 1.5% when contrasting chemical composition alone is considered.

Thermal-mechanical dynamic models constructed by *van Wijk et al.* [2008] tested the effects of a 40 km increase in lithosphere thickness between the Rio Grande rift and the adjacent Great Plains in the southwestern United States. Thermal fields from the models were then used to calculate seismic velocities, and the results were compared with velocity perturbations observed in seismic tomography models [*van Wijk et al.*, 2008, and references therein]. Edge-driven convection at the modelled lithosphere step resulted in upwelling of asthenospheric material below the rift zone and downwelling of cold, and therefore thermally unstable, material at the edge of the step, and thinning of the lithosphere was concentrated to within ~100-300 km of the step edge [*van Wijk et al.*, 2008]. Overall, it was found that compared to tests run for a uniformly thick lithosphere, inclusion of a step in the lithosphere produced a velocity field that closely paralleled the velocity field observed in the seismic tomography models [*van Wijk et al.*, 2008].

A similar study by *van Wijk et al.* [2010] found that edge-driven convection can also adequately explain the observed bowl-shaped surface topography of the Colorado Plateau and temporal changes in magma composition along its margins. The results of the study suggest that the removal of thermally unstable lithospheric material by edge-driven convection causes surface uplift to occur along the perimeter of the plateau; colder and thus denser lithospheric material of

the plateau is replaced by warmer, buoyant asthenospheric material [*van Wijk et al.*, 2010]. In addition to surface uplift, *van Wijk et al.* [2010] also proposed that edge-driven convection along the periphery of the plateau explains the change in composition of volcanic rocks, from a predominantly intermediate silica content during the Cenozoic to a predominantly basaltic composition during Neogene through Quaternary time. This compositional change is attributed to upwelling asthenospheric material that re-fertilized the lithosphere along the margins of the plateau [*van Wijk et al.*, 2010]. Comparisons between calculated seismic velocity perturbations from the thermal field produced by the models (V_s ~9%) and those observed in seismic tomography models (V_s ~12%) led *van Wijk et al.* [2010] to further suggest that edge-driven convection can largely account for the decrease in seismic velocity observed in the lithosphere surrounding Colorado Plateau.

Hardebol et al. [2012] used geodynamic modelling to study the effects of edge-driven convection resulting from a lithosphere step, like that observed below western Canada. In their experiments, the thickness of the mantle lithosphere is represented as a thermal boundary layer which was varied in both the Cordillera and the craton. The size of the lithosphere step was varied (60 km versus 140 km) and a constant 500 km wide lateral transition between thin and thick lithosphere was prescribed in the initial geometry of the models [*Hardebol et al.*, 2012]. In addition to variations in lithosphere thickness, the rheology of the cratonic mantle lithosphere was also varied between end-member wet and dry olivine rheologies in order to test the influence of variations in effective viscosity on the lithosphere step [*Hardebol et al.*, 2012]. Based on the results of the models, *Hardebol et al.* [2012] concluded that edge-driven convection increases in vigor as the difference in lithosphere thickness, and thus the lateral temperature gradient increased. In addition, the imposed lateral temperature gradient will migrate toward the interior

of the craton, unless the mantle lithosphere is strong enough to prevent erosion of the step, as is the case when a dry olivine rheology was used in the models [*Hardebol et al.*, 2012]. Therefore, *Hardebol et al.* [2012] concluded that the persistence of a lithosphere step is controlled by the interplay between edge-driven mantle flow and mantle lithosphere rheology.

Most recently, a study by *Currie and van Wijk* [2016] used geodynamic models to investigate the stability of an initially vertical 100 km step in the lithosphere, similar to that observed at the Cordillera-craton boundary. In their experiments, *Currie and van Wijk* [2016] varied the density and relative strength (representative of chemical depletion and dehydration, respectively) of the craton mantle lithosphere relative to the surrounding mantle. After 50-100 Ma of model time, craton margins that maintained dip angles of >45° were considered stable, whereas angles of <45° were considered unstable [*Currie and van Wijk*, 2016]. Overall, the results of the study suggest that, although increased relative strength was found to exert a greater influence, the preservation of steep craton margins requires both increased compositional buoyancy (20-40 kg/m^3 less dense) and increased relative strength (by a factor of ≥5) of the cratonic mantle lithosphere relative to the surrounding mantle [*Currie and van Wijk*, 2016].

The previous modelling studies described above differ from the present study in two important ways: 1) the imposed velocity boundary conditions; and 2) the rheological parameterization used in the models. Unlike the models constructed by *van Wijk et al.* [2008], extensional velocity boundary conditions are not tested in any models for the present study. In the numerical models constructed by *Currie and van Wijk* [2016] and *Hardebol et al.* [2012], the effects of large-scale mantle flow are tested. A shear velocity is imposed on the base of the mantle lithosphere in one model from the study by *Hardebol et al.* [2012], but the speed and direction of mantle flow is not varied in their experiments. *Currie and van Wijk* [2016] test the

influence of horizontal mantle flow in two directions through the model domain, but the velocity (2 cm/yr) of the flow is not varied. In addition, none of the studies described above test the influence of crustal shortening on the stability and evolution of the craton margin. In the present study, a through-flowing velocity boundary condition imposed on the sub-lithospheric mantle and both its speed and direction are varied. This is done to test the sensitivity of the craton mantle lithosphere to shearing at its base caused by large-scale regional mantle flow (referred to as mantle wind), and the results of ancillary tests on a set of models that incorporate crustal shortening are also presented.

In the study by *Hieronymus et al.* [2007] described above, convective flow patterns in the sub-lithospheric mantle are modelled using diffusion creep. For this study, dislocation creep is used to describe deformation in the mantle, as this is thought to be the dominant deformation mechanism in the shallow (~200-300 km) upper mantle [*Karato and Wu*, 1993]. *Hieronymus et al.* [2007] assign a pyrolite rheology to the sub-lithospheric mantle, and a harzburgite rheology is used to describe the entire mantle lithosphere. Subsequently, any effects that may be attributed to the crust are entirely neglected; however, because the study aimed to enable direct comparison with seismic tomography models, which use crustal corrections, this simplification may be justified. The numerical models presented by *Hardebol et al.* [2012] ascribe a wet quartzite rheology and a reference density of 2800 kg/m^3 to the entire crust, which may be unrealistically weak and buoyant as the crust contains minerals that are comparatively less hydrated and more mafic. Distinct rheologies are assigned to the upper and lower crust in the present study, and thus the two layers are treated independently. *Hardebol et al.* [2012] consider the influence of mantle lithosphere dehydration on the longevity of a step in the lithosphere by comparing end-member behavior of wet and dry olivine flow laws from *Hirth and Kohlstedt* [1996]. The present study

follows the approach of *Currie and van Wijk* [2016] by using the dislocation creep flow law for damp olivine from *Hirth and Kohlstedt* [2003] for the craton mantle lithosphere, and scaling the water content to investigate the behavior of mantle materials that contain intermediate amounts of water.

All of the previous studies discussed above used numerical modelling to explore the influence of a discontinuity in lithosphere thickness; however, with the exception of the study by *Currie and van Wijk* [2016], none of these studies have focused on the geometry of the lithosphere step (specifically, the conditions needed to produce a vertical or dipping boundary) and its evolution through time. The present study exclusively focusses on the response of a step in the lithosphere to dynamic processes, such as mantle convection, large-scale regional mantle flow and crustal shortening, with application to western Canada.

1.3 Objectives

Prompted by new geophysical observations described in Section 1.1, the present study considers the evolution of craton margin geometry in western Canada, placing particular focus on geodynamic processes at the craton margin that may promote or hinder the formation of vertical and west-dipping craton margin geometries. Thermally-mechanically coupled geodynamic models are used to provide new insight into craton stability; with a particular focus on the evolution of craton margin geometry over time-scales of 200 Ma. The objectives are:

1. To determine the rheological and compositional conditions necessary to facilitate the development of a craton margin geometry in which the craton edge dips below the back arc, as recently observed in western Canada.

2. To test the response of the modelled craton margin to dynamic processes such as mantle convection, large-scale mantle flow relative to the overlying lithosphere (also referred to as mantle wind) and crustal shortening.
3. To determine whether vertical and west-dipping craton margins are permanent (i.e. maintained over time scales of 100 Ma or more) or transient features (only observed over time scales of 10's of Ma).

1.4 Thesis outline

Chapter 2 of this thesis will provide the background information for the tectonic history of the North American craton and Cordillera of western Canada, as well as describing the current tectonic environment of western Canada and relevant geophysical observations from the region. A description of the finite element code used in this study (SOPALE) and its governing equations are given in Chapter 3, along with a detailed description of the model parameterization. The results of the numerical models are presented in Chapter 4, and their implications for western Canada are discussed in Chapter 5. Finally, the conclusions of this study and recommendations for future work are given in Chapter 6.

Chapter 2: Regional Background

This chapter describes the tectonic history of western Canada. First, a brief history of the formation of the North American craton is given in Section 2.1. This is followed by a summary of the Cordilleran orogeny in Section 2.2. Finally, the current tectonic environment of western North America is described in Section 2.3.

2.1 Tectonic Evolution of the Western Canadian North American Craton

The tectonic history of the western portion of the North American craton margin spans the majority of the geologic time-scale, from the Archean to the present day, and records multiple phases of compressional and extensional tectonics [*Cook and Erdmer*, 2005]. The craton consists of a collection of Archean and Proterozoic tectonic domains that were welded together over a series of orogenic and accretionary events that occurred during the Paleoproterozoic between 2.0 to 1.8 Ga [*Hammer et al.*, 2010]. In much of western Canada, these tectonic domains currently underlie the Phanerozoic sediments of the Western Canadian Sedimentary Basin (WCSB), forming the crystalline basement [*Hope and Eaton*, 2002]. The dashed box in Figure 2.1 shows the Precambrian-aged tectonic domains that comprise the North American craton in the southern half of Alberta. These include the Hearne Province and the Lacombe, Rimbey, Thorsby and Wabamun domains.

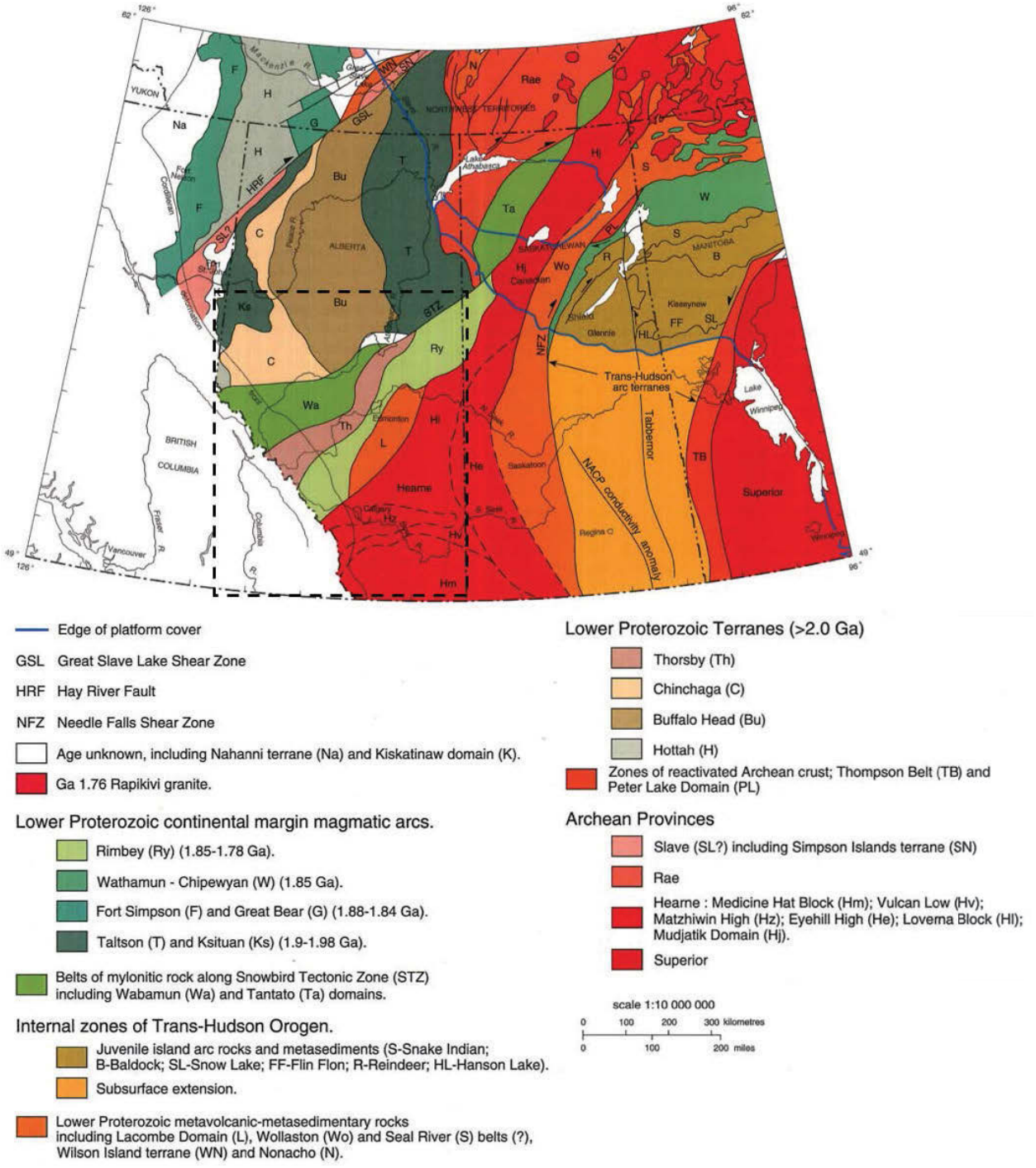

Figure 2.1: Regional map showing the Precambrian tectonic domains that constitute the basement rocks of western Canada. The bold, dashed black box shows the study area and tectonic domains discussed in the text. Modified from *Ross et al.* [1994]

The Hearne Province is an Archean-aged crustal block comprised of smaller fragments of Archean crust (e.g. Medicine Hat block, Loverna block, Lacombe domain, Rimbey domain and

the Vulcan Structure) that was incorporated into ancestral North America during the Thelon (~1.96-1.92 Ga) and Trans Hudson (1.9-1.7 Ga) orogenies, when it was amalgamated with the Superior, Slave and Rae provinces [*Ross et al.*, 2000; *Ross*, 2002; *Hammer et al.*, 2010]. With the exception of the Medicine Hat block, the majority of the Hearne Province has undergone penetrative intermediate to high grade deformation during the Trans Hudson and Taltson orogens [*Ross*, 2002; *Hammer et al.*, 2010]. As a result of this deformation, rocks of the Hearne Province are generally amphibolite to granulite facies, with additional magmatic rocks that have ages ranging between 1.80 and 1.82 Ga [*Ross*, 2002; *Hammer et al.*, 2010]. The Vulcan Structure, which forms part of the Hearne Province, has been interpreted as an Archean suture zone between the Medicine Hat and Loverna blocks [*Clowes et al.*, 2002; *Gorman et al.*, 2002; *Ross*, 2002].

The Lacombe, Rimbey, Thorsby and Wabamun domains lie within and northwest of the Hearne Province [*Ross et al.*, 2000]. The Wabamun and Thorsby domains are bordered to the north and south by two branches of the Snowbird Tectonic Zone (STZ in Figure 2.1), an apparent suture zone between the Hearne and Rae provinces whose origin and evolution are still actively debated [*Ross et al.*, 2000]. They were amalgamated into the North American craton in Paleoproterozoic time during the Alberta Orogen [*Ross et al.*, 1991, 2000; *Ross*, 2002]. The Thorsby domain consists of felsic metaplutionic rocks (~1.8 Ma) that are interpreted to be the product of collision of the ~2.3 Ga biotite tonalities of the Wabamun domain with the Hearne Province, and thus they represent a suture zone [*Ross et al.*, 1991, 2000]. The Rimbey and Lacombe domains lie within the Hearne Province, along the southern border of the Snowbird Tectonic Zone; the former consists of 1.79-1.85 Ga granites and the latter consists of low-grade metavolcanic and metasedimentary rocks of marine origin [*Hope et al.*, 1999; *Ross et al.*, 2000;

Ross, 2002]. Taken together, the Rimbey and Lacombe domains are thought to be the remnants of arcs formed during the Thelon Orogeny, which record subduction of oceanic crust below the Hearne Province [*Ross et al.*, 1991, 2000; *Ross*, 2002].

2.2 The Cordilleran Orogen

The Canadian Cordillera is the region of more juvenile lithosphere that is located to the west of the North American craton, and is generally divided into five distinct morphological belts, as shown in Figure 2.2. The earliest inception of the present-day Canadian Cordillera began with the break-up of the supercontinent Rhodinia during Neo-Proterozoic-Cambrian time, from ~750 to 450 Ma [*Monger and Price*, 2002; *Cook and Erdmer*, 2005]. This rifting event resulted in the formation of an ocean basin along the western edge of the North American craton, which became a passive margin [*Dickinson*, 2004; *Hammer et al.*, 2010]. Sedimentation along this passive margin occurred from the Neoproterozoic and into the Devonian and resulted in the formation of a westward thickening miogeocline [*Dickinson*, 2004; *Cook and Erdmer*, 2005]. Deposits of shallow and deep water carbonates and shales deposited during this time interval indicate a westward deepening ocean basin, and occur in the Foreland and Omineca belts of the present-day Cordillera, as well as within the Western Canadian Sedimentary Basin to the east (Figure 2.2) [*Monger and Price*, 2002; *Hammer et al.*, 2010].

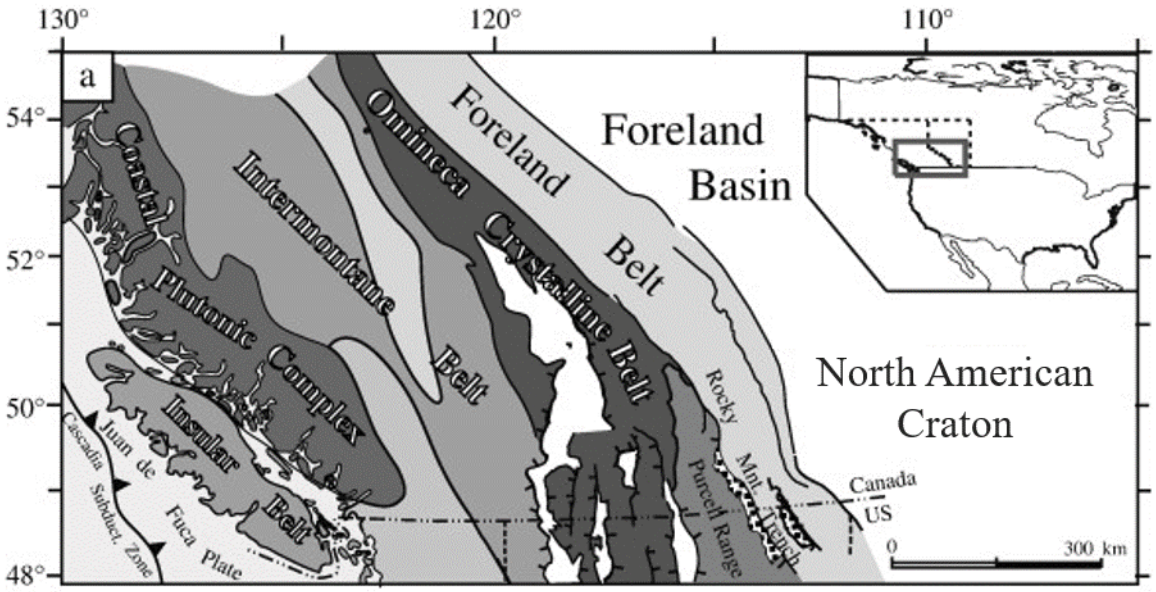

Figure 2.2: Regional map showing the five tectono-morphological belts that form the Canadian Cordillera. Note that Foreland Basin is used here to refer to the Western Canada Sedimentary Basin (WCSB). Modified from *Hardebol et al*. [2013].

A transition from extensional to compressional tectonics began in the Middle Devonian (~390 Ma) with the initiation of an intra-oceanic subduction zone west of the North American craton [*Monger and Price*, 2002]. During the Middle and Late Devonian and into the Early Triassic, the passive margin that flanked the North American craton collided with the off-shore subduction zone and subsequent terrane and arc accretion resulted in thrusting of allochthons onto the miogeocline [*Dickinson*, 2004]. Furthermore, arc magmatism was initiated in and along the miogeocline and adjacent terranes, producing the Middle to Late Devonian-aged intrusive and extrusive rocks of the present-day Omineca Belt [*Monger and Price*, 2002; *Evenchick*, 2007]. During the Middle Triassic to the Middle Jurassic, further subduction of oceanic crust west of North American produced an arc trench system that remained separated from the North American craton by back arc basins, which experienced marine flooding, resulting from the break-up of Pangaea [*Monger and Price*, 2002; *Dickinson*, 2004].

Collision between the intra-oceanic subduction zone and the western edge of the North American craton began in the Jurassic (~183 Ma), and resulted in the accretion of Intermontane and Insular belt terranes to the North American craton during the Middle Jurassic through the mid-Cretaceous [*Dickinson*, 2004; *Evenchick*, 2007; *Hammer et al.*, 2010]. At the same time, continental arcs formed both within the accreted terranes, as well as within the western edge of the North American craton [*Monger and Price*, 2002]. In addition to arc magmatism, collision and continued convergence along the western edge of the North American craton produced fold and thrust deformation of the passive margin sediments, generating the Foreland Belt [*Hammer et al.*, 2010]. From the mid-Cretaceous until well into the Cenozoic, these magmatic arcs rapidly migrated ocean-ward, resulting in the emplacement of the Coast batholith during the Late Cretaceous to mid-Eocene [*Monger and Price*, 2002; *Dickinson*, 2004]. Arc magmatism ceased during the Paleocene when the spreading ridge between the Kula plate and the now-subducted Resurrection oceanic plate collided with North America; by ~40 Ma relative motion between the Kula plate and North America became dextral and the Queen Charlotte fault system was initiated, while subduction of the Farallon oceanic plate continued further south [*Dickinson*, 2009; *Hammer et al.*, 2010].

2.3 Current Tectonic Environment

The present day North American plate consists of the North American craton and the accreted terranes of the Cordillera. On a global scale, the Cordillera comprises a portion of the Circum Pacific orogenic belt, a ring of subduction zones that flank the edges of the Pacific plate, [*Dickinson*, 2004]. In the southern portion of western Canada, the Cordillera is bounded by the Cascadia subduction zone, where the Juan de Fuca (the remaining fragment of the Farallon plate) plate is being subducted below the North American plate, producing related regions of arc

magmatism [*Monger and Price*, 2002; *Hyndman*, 2015]. North of the Cascadia subduction zone the boundary between the North American and Pacific plates is defined by the Queen Charlotte fault, which has been experiencing predominantly right lateral strike-slip motion since ~6 Ma, with a minor (~1 cm/yr) component of convergence [*Hyndman*, 2015; *Tréhu et al.*, 2015]. In the southern segment of the Canadian Cordillera, the Omineca and Intermontane belts (Figure 2.2) comprise the present-day back arc region of the Cascadia subduction zone and are bounded to the east by the Rocky Mountain Trench and to the west by the fore arc region which consists of the Coast Belt and extends west to the subduction zone located off shore of Vancouver Island.

2.4 Lithosphere Structure

Detailed studies of the Cascadia back arc have shown that features such as high surface heat flow, high Moho temperatures and thin lithosphere are characteristics generally inherent to back arc environments globally [*Hyndman and Lewis*, 1999; *Hyndman et al.*, 2005; *Currie and Hyndman*, 2006; *Hyndman and Currie*, 2011]. Conversely, the immediately adjacent North American craton has low surface heat flow and thick lithosphere. Geophysical observations detailing contrasts between the Cordillera and the craton lithosphere are presented below, along with a discussion of how these characteristics influence geodynamics at the Cordillera-craton boundary. In addition to contrasts between the Cordillera and craton mantle lithosphere, large scale mantle flow may play an important role in the evolution of craton margin geometry; therefore, evidence of mantle flow from seismic anisotropy below western Canada will also be discussed.

2.4.1 Geophysical Observations

Seismic imaging techniques such as reflection, refraction and tomography have been used to study the structure of the crust and mantle below both the North American craton and the

Cordillera. Results of these studies indicate that the Cordillera has an average Moho at depth of ~30-35 km [*Hammer and Clowes*, 2007; *Kao et al.*, 2013]. In general, the Moho below the Cordillera is remarkably flat and shallow compared to global averages and lacks variations associated with its tectonic domain boundaries [*Clowes et al.*, 2005]. Within the craton, the Moho lies at an average depth of ~40 km; however, variations in Moho depth associated with specific tectonic domains and other large geologic and structural features are also present. An 1800 km seismic reflection profile compiled from the Lithoprobe Alberta Basement Transect yields an average Moho depth of 40 km in the craton below Alberta, with depth ranging between 35 km and 48 km [*Bouzidi et al.*, 2002; *Gu and Shen*, 2015]. An abrupt step in the Moho of >10 km was recorded above the Snowbird Tectonic Zone [*Bouzidi et al.*, 2002]. In addition, there is an increases in Moho depth (~42 km) associated with the Vulcan structure [*Bouzidi et al.*, 2002]. Refraction profiles from the Southern Alberta Refraction Experiment (SAREX) also place the Moho at a depth of ~40 km below the Hearne Province, with a generally high velocity of 6.0-7.2 km/s in the crust [*Gorman et al.*, 2002]. Large scale ambient noise tomography models that span continental North America show that Moho depth within the craton tends to thin toward its interior, with an overall depth range of ~35-41 km [*Kao et al.*, 2013].

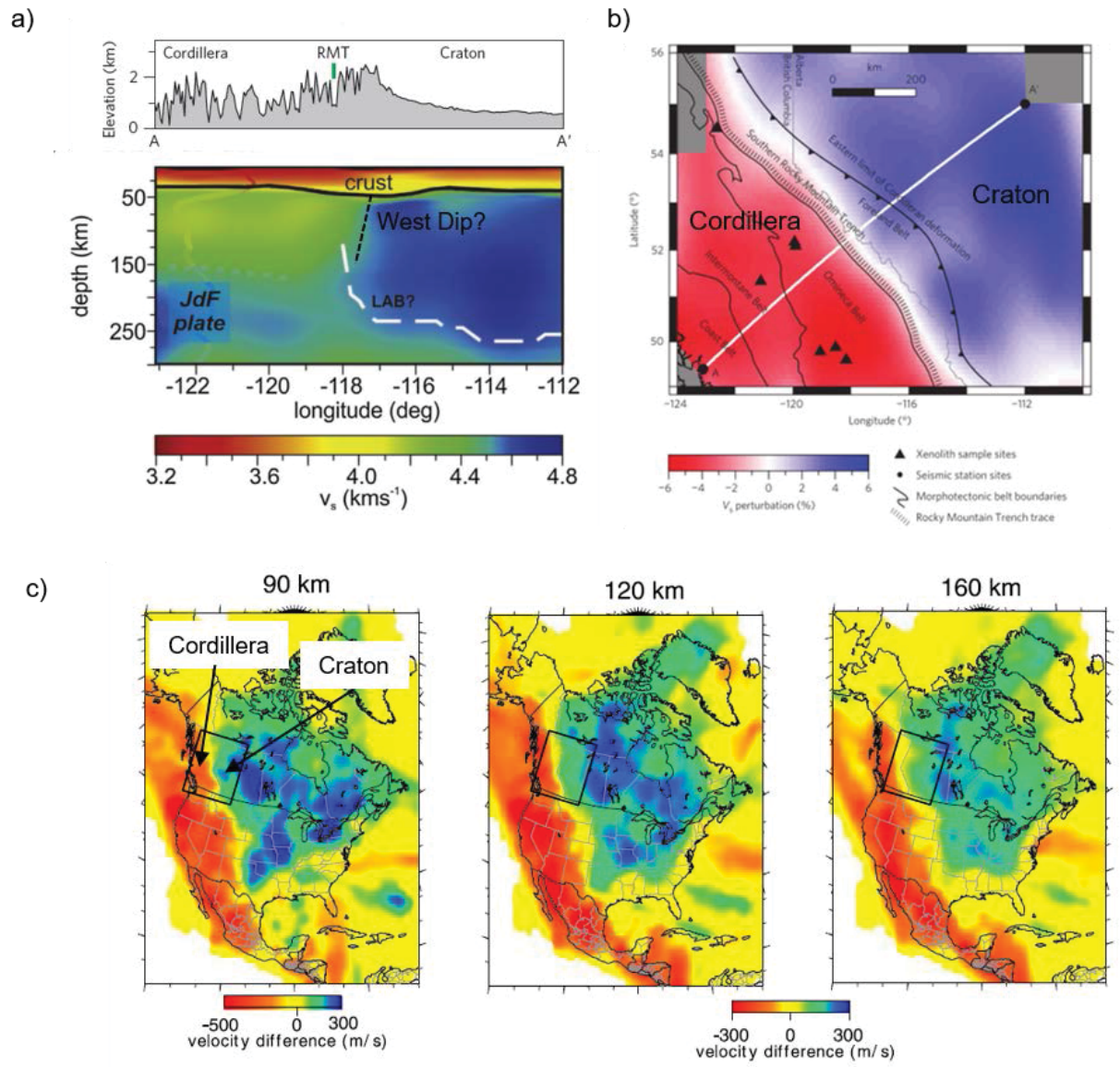

Figure 2.3: Examples from the literature of seismic tomography models that record the sharp lateral and vertical transition in seismic velocity that occurs across the Cordillera-craton boundary in western Canada. a) Cross section through the ambient noise tomography model of *Bao et al*. [2014] showing the sharp transition in shear wave velocity between the Cordillera and craton mantle lithosphere, as well as the inferred lithosphere-asthenosphere boundary (white line). b) Topographic view of the *Bao et al*. [2024] model showing the percent perturbation in shear wave velocity at 105 km depth as well as the location of the cross-section shown in a). c) Depth slices through Rayleigh wave tomography model of *Bedle and Van Der Lee* [2009] showing the contrast in shear wave velocity at the Cordillera-craton boundary.

Seismic tomography models of western North America yield shear wave velocities in the shallow (~100 km depth) Cordillera mantle that are approximately 6% to 9% slower than the adjacent craton [*Frederiksen et al.*, 2001; *Bedle and Van Der Lee*, 2009; *Bao et al.*, 2014]. This

contrast in mantle seismic velocity has been interpreted to indicate the presence of hot mantle material below the Cordillera [*Frederiksen et al.*, 2001; *Goes and Van Der Lee*, 2002; *Bedle and Van Der Lee*, 2009; *Kao et al.*, 2013; *Bao et al.*, 2014]. As illustrated in Figure 2.3, the transition from relatively slow velocities in the Cordillera mantle lithosphere to fast velocities in the craton is abrupt; shear wave velocities increase by ~100 m/s over a lateral distance of ~50 to 150 km across the Cordillera-craton boundary [*Bedle and Van Der Lee*, 2009; *Bao et al.*, 2014]. Furthermore, S-wave tomography models indicate that the base of the mantle lithosphere below the craton is located at an average depth of ~250 km, compared to 60 km depth below the Cordillera [*Frederiksen et al.*, 2001; *Bedle and Van Der Lee*, 2009; *Kao et al.*, 2013; *Bao et al.*, 2014]. The transition from ~60 km thick to ~250 km thick lithosphere coincides with the contrast in seismic velocity observed across the Cordillera-craton boundary (Figures 1.2 and 2.3), thus a ~190 km step in the lithosphere occurs at the Cordillera-craton boundary (i.e. below the Tintina fault and Rocky Mountain Trench) over a lateral distance of ~100 km [*Bao et al.*, 2014].

2.4.2 Thermal Regimes

The abrupt decrease in lithosphere thickness from the craton to the Cordillera that occurs at the Rocky Mountain Trench, also corresponds with a westward increase in average surface heat flow across the boundary, from ~45 mW/m^2 to ~75 mW/m^2 (Figure 2.4b) [*Hyndman and Lewis*, 1999; *Hyndman*, 2010]. Based on heat flow data, calculated geothermal gradients yield Moho temperatures as high as ~800-900°C below the Cordillera and ~400-500 °C (Figure 2.4c) below the craton [*Hyndman and Lewis*, 1999; *Hyndman and Currie*, 2011; *Hardebol et al.*, 2013]. This contrast in thermal regimes is consistent with the seismic observations discussed above which suggest that the Cordillera mantle is hotter than that of the craton.

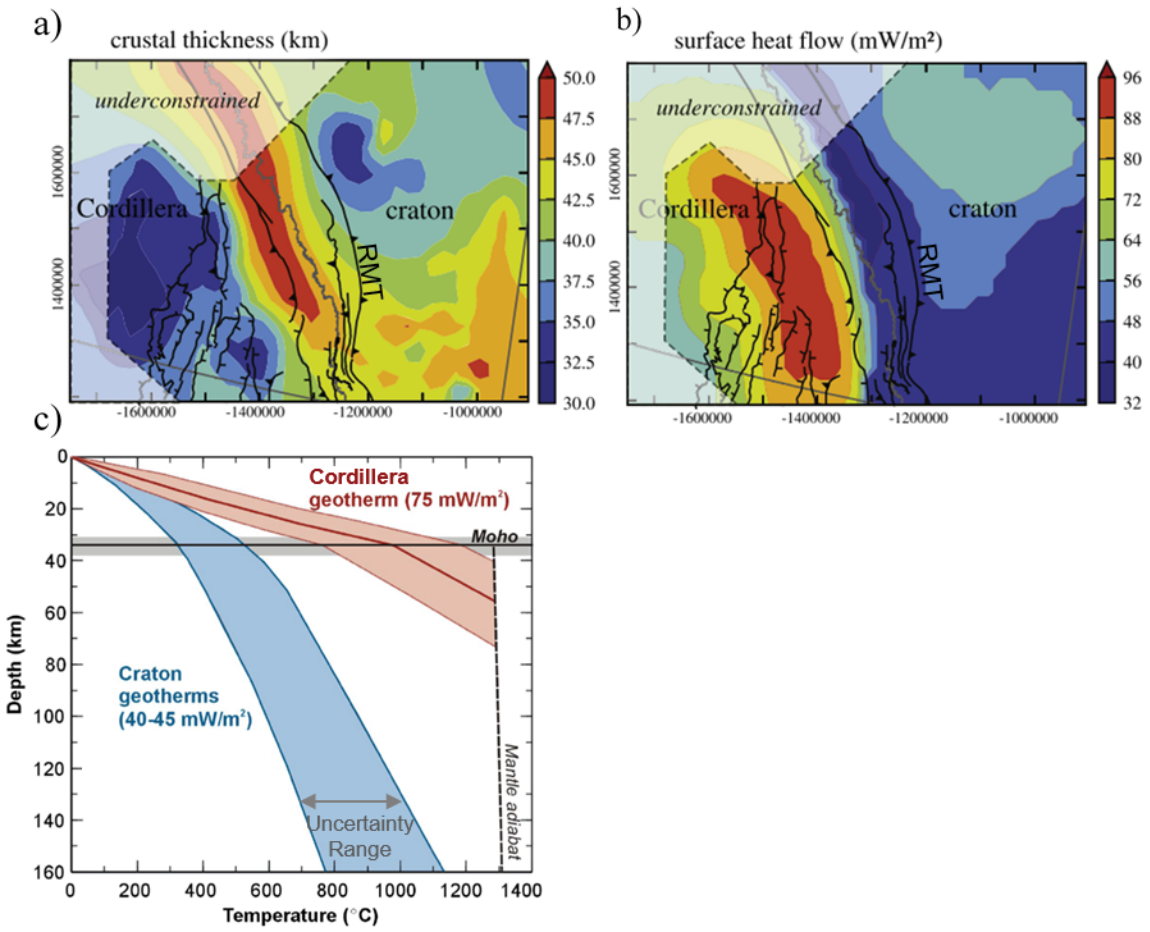

Figure 2.4: Summary of contrast in thermal regime between the Cordillera and North American craton, as inferred from surface heat flow data. Maps modified from *Hardebol et al.* [2013] showing; a) the variation in crustal thickness, and b) the distribution of measured surface heat flow. Note RMT = Rocky Mountain Trench. c) calculated geothermal gradients and their extrapolated uncertainty. Modified from *Currie and Hyndman* [2006].

The surface elevation of the Cordillera is ~1.0-1.5 km [*Hyndman and Currie*, 2011]. As previously discussed, the crust of the Cordillera has a thickness of ~30-35 km, whereas the craton has an average crustal thickness of ~40-45 km (Figure 2.4a). Airy isostasy predicts that the surface elevation of the Cordillera should be less than that of the craton, owing to its smaller crustal thickness. An analysis of the thermal structure of the Cordillera and craton shows that the high elevation of the Cordillera is consistent with this being an area of high temperatures and thin lithosphere; the density reduction resulting from thermal expansion provides the support to

maintain the high elevation [*Hyndman*, 2010; *Hyndman and Currie*, 2011]. Studies of thermally supported topography have shown that the high geothermal gradient can account for as much as 1.6 km of elevation in the Cordillera relative to the North American craton, after correcting for crustal density differences between the two regions [*Hyndman and Currie*, 2011].

The disparity in crustal thickness and temperature gradients between the Cordillera and craton also has important consequences for lithosphere strength and deformation styles across the Cordillera-craton boundary. A Moho temperature of 800-900°C below the Cordillera implies that the lower crust is within the granulite facies, and the basalt solidus (1200°C at a pressure of ~3 GPa) occurs at a depth of <100 km [*Hyndman and Lewis*, 1999]. The strength of crust and mantle rocks decreases with increasing temperature [*Karato and Wu*, 1993; *Hirth and Kohlstedt*, 2003]. Given the high temperatures below the Cordillera, the strength of the lower crust and upper mantle lithosphere is relatively low, thus concentrating strength in the upper crust [*Hyndman and Lewis*, 1999]. The effective elastic thickness of the lithosphere in the Cordillera has been estimated to be between 5 km and 15 km, and does not exceed 20 km [*Hyndman et al.*, 2009; *Hardebol et al.*, 2013]. In comparison, the low temperatures below the craton indicate both crust and upper mantle possess a strength at least a factor of 10 greater than the Cordillera [*Hyndman and Lewis*, 1999]. Furthermore, the integrated strength of the craton lithosphere is thought to be approximately an order of magnitude greater than the Cordillera, and estimates of effective elastic thickness are in the range of 40-80 km [*Hyndman et al.*, 2005, 2009; *Hardebol et al.*, 2013].

The thermal characteristics exhibited in the Cordillera, including high surface heat flow, effective elastic thickness of less than 30 km, and high surface elevation despite thin crust, are thought to be inherent traits of subduction zone back arcs in general [*Hyndman et al.*, 2005;

Currie and Hyndman, 2006; *Hyndman and Currie*, 2011]. Furthermore, high temperatures at such shallow depths below back arcs have been attributed to vigorous mantle convection, facilitated by dehydration of the subducting slab, resulting in a lower melting temperature and reduced viscosity of the surrounding asthenosphere [*Hyndman et al.*, 2005; *Currie and Hyndman*, 2006; *Hyndman and Currie*, 2011]. Numerical models of such thermal conditions suggest that even after subduction has ceased, the high temperatures observed in back arc environments like the Cordillera can persist for up to 300 Ma [*Currie and Hyndman*, 2006].

2.4.3 Seismic Anisotropy and Mantle Flow

In addition to inherent characteristics of the Cordillera and North American cratonic lithosphere, other factors, such as large-scale flow of the asthenosphere or mantle wind (i.e. motion of the asthenosphere relative to the overlying lithosphere), add to the complexity of the geodynamic environment and may affect the structure of the lithosphere. One indication of mantle flow patterns comes from seismic anisotropy. Mantle anisotropy results from the preferred orientation of mantle minerals, such as olivine and pyroxene, in response to shear strain [*Savage*, 1999]. Dislocation creep, an important mechanism for deformation in the mantle, occurs when imperfections in a crystal migrate through its lattice to the outer boundary of the crystal. This results in lattice preferred orientation (LPO) of olivine crystals, and consequently, anisotropy [*Savage*, 1999]. Seismic anisotropy occurs when phases of a wave travel at varying speeds depending on either the direction of travel or the polarization of the energy [*Savage*, 1999]. Seismic anisotropy can be measured using compressional (P-waves), shear (S-waves) or surface (Rayleigh or Love) waves. A large number of studies that explore seismic anisotropy in the mantle concentrate on polarization anisotropy in olivine using technique called shear wave splitting. It should be noted that anisotropy measurements have 180° of ambiguity, and thus the

direction of mantle flow inferred from seismic anisotropy also has 180° of ambiguity; additionally, seismic anisotropy can not be used to determine mantle flow velocity.

Based on observations of azimuthal anisotropy, *Yuan and Romanowicz* [2010a] and *Yuan et al.* [2010] have argued for the presence multiple anisotropic layers below the Cordillera. They suggest alignment of olivine fast axes below the Cordillera are in agreement with North American absolute plate motion to depths of ~70 to 100 km [*Yuan and Romanowicz*, 2010a; *Yuan et al.*, 2011]. However, below the Cordillera at depths of ~ 150-200 km the fast axis orientation changes, and the fast axis orientation is aligned with absolute motion of the Pacific plate, suggesting mantle flow below the Cordillera may change direction with depth [*Yuan and Romanowicz*, 2010a; *Yuan et al.*, 2011]. Interestingly, this change in azimuthal anisotropy also occurs at the Rocky Mountain Trench, which further suggests that mantle flow not only changes with depth but may also change laterally across the Cordillera-craton boundary [*Yuan and Romanowicz*, 2010a, 2010b; *Yuan et al.*, 2011].

Seismic anisotropy for the Cordillera mantle also exhibits local variation. As shown in Figure 2.5b, within the central portion of the Cordillera backarc, shear wave splitting measurements yield fast directions that are oriented NE-SW [*Currie et al.*, 2004; *Courtier et al.*, 2010; *Gu et al.*, 2011]. This orientation is consistent with the direction of absolute plate motions between the overriding North American plate and the subducting oceanic Juan de Fuca plate [*Currie et al.*, 2004; *Courtier et al.*, 2010; *Gu et al.*, 2011]. Anisotropy in this region has been interpreted as the result a combination of deformation in the shallow portion of the overriding backarc mantle lithosphere and in the mantle wedge below [*Currie et al.*, 2004]. Anisotropy measured using Rayleigh waves indicate that, within the lower crust of both the Cordillera backarc and the adjacent Foreland Belt (Figure 2.5a, 20 s), fast directions are aligned parallel to

the strike of the deformation front (NW-SE) and interpreted as evidence of ductile flow as a consequence of the Laramide Orogeny [*Bao et al.*, 2016]. More complex seismic anisotropy has been reported in the southern region of the Canadian Cordillera.

Null anisotropy in shear wave splitting data and low to null anisotropy in Rayleigh wave data have been reported below the southern portion of the Canadian Cordillera (shown by dashed black circles in Figure 2.5a) [*Currie et al.*, 2004; *Bao et al.*, 2016]. Several explanations have been proposed to explain the apparent lack of horizontal mantle anisotropy in this region. As previously discussed in Section 2.4.2, due to the high thermal gradient and the presence of slab-derived fluids, the lithosphere of the Cordillera is thin (~60 km) [*Bedle and Van Der Lee*, 2009; *Kao et al.*, 2013; *Bao et al.*, 2014], and thus, deformation may occur via diffusion creep in the asthenosphere, which does not produce mantle anisotropy [*Currie et al.*, 2004]. Null measurements could also result from vertically directed mantle flow caused by the presence of a slab window, delamination of Cordillera lithosphere, edge-driven convection, or some combination of these mechanisms [*Currie et al.*, 2004; *Gu et al.*, 2011; *Bao et al.*, 2016]. Overall, the observed seismic anisotropy in the Cordillera shows along-strike variation and is thought to be particularly complex below the southern Canadian Cordillera.

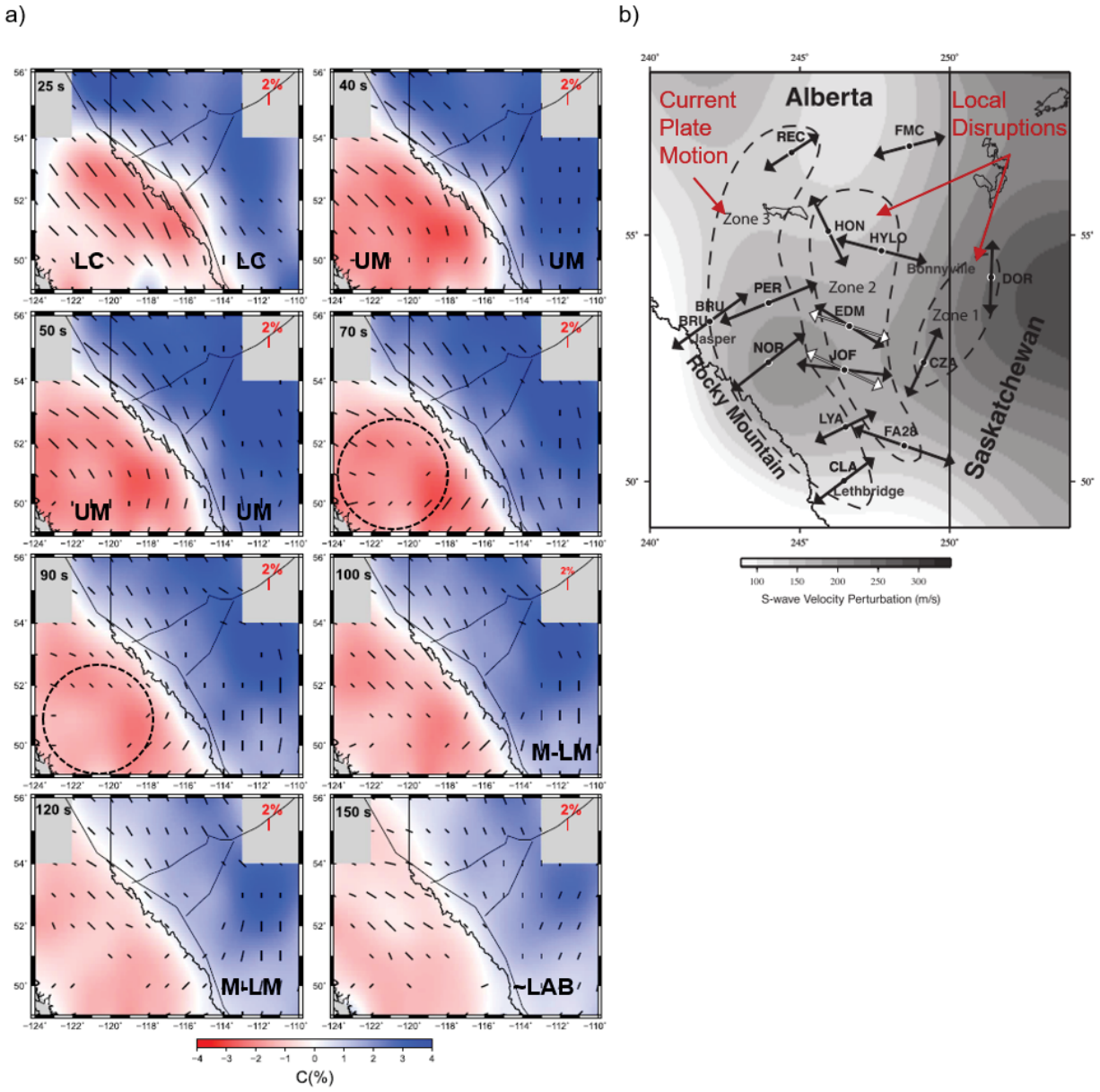

Figure 2.5: Observations of seismic anisotropy from western Canada. a) Slices through combined tomographic inversion model of Rayleigh wave phase velocities overlain by azimuthal anisotropy from *Bao et al.* [2016]. The period corresponding to each slice is shown in the upper left-hand corner of each slice. The dashed circles at 70 s and 90 s indicate the region of observed null anisotropy discussed in text. The approximate depths within the Cordillera (LHS of map) and craton (RHS of map) lithosphere are indicated as follows; LC = Lower Crust, UM = Uppermost Mantle, M-LM = Middle to Lower Mantle, ~LAB = approximate Lithosphere-Asthenosphere Boundary below the craton. Note; the velocity scale indicates the percentage of perturbation relative to the average velocity for each period. Modified from *Bao et al.* [2016]. b) Shear velocity map (background grey-scale) overlain by olivine fast directions (black and white arrows) in the mantle lithosphere below Alberta from shear wave splitting study by *Gu et al.* [2011]. The location of seismic stations used in the study are indicated by dots and abbreviated station names, white arrows indicate regions potentially exhibiting two anisotropic layers. Dashed black lines indicate distinct anisotropic zones identified by *Gu et al.* [2011] and described in text. Modified from *Gu et al.* [2011].

Complex seismic anisotropy is also reported from studies of the North American craton lithosphere. Rayleigh (Figure 2.5a) and shear wave splitting data (Figure 2.5b) indicate the presence of two anisotropic layers and several regions of anomalous anisotropic patterns within the lithosphere of the North American craton [*Currie et al.*, 2004; *Courtier et al.*, 2010; *Gu et al.*, 2011; *Bao et al.*, 2016]. An upper anisotropic layer with olivine fast directions oriented approximately N-S has been reported in many studies, and has been interpreted as "frozen" anisotropy representing fossil deformation that occurred during the accretion of the craton in the Paleozoic [*Currie et al.*, 2004; *Yuan and Romanowicz*, 2010b; *Gu et al.*, 2011; *Bao et al.*, 2016]. Based on shear wave splitting parameters, this upper layer has been estimated to be between ~140 km and 220 km thick [*Currie et al.*, 2004; *Yuan and Romanowicz*, 2010b; *Bao et al.*, 2016]. The lower layer of anisotropy has olivine fast directions that are oriented NE-SW and align with present-day relative motion of the North American plate [*Currie et al.*, 2004; *Yuan and Romanowicz*, 2010b; *Gu et al.*, 2011] and an estimated thickness of approximately 200 km [*Currie et al.*, 2004; *Bao et al.*, 2016]. Within the cratonic lithosphere below central and eastern Alberta, an anomalous region of anisotropy has been reported by *Gu et al*. [2011]. Olivine fast axes in this region appear to be tangentially aligned with a N-S oriented elliptical feature in the craton mantle lithosphere that *Gu et al.* [2011] interpret as the presence of a possible tectonic boundary within the craton lithosphere or a potential cratonic keel at the base of the mantle lithosphere which may locally disrupt mantle flow patterns. In addition to anisotropic anomalies in the deeper part of the cratonic lithosphere, other small-scale features (~50-200 km in length) have been identified and interpreted as being associated with surface and/or crustal tectonics [*Courtier et al.*, 2010].

The studies described above illustrate the lateral and vertical variations in radial and azimuthal anisotropy, observed in studies of both shear waves and Rayleigh waves below western Canada. Interpretation of these observations suggest complex mantle flow patterns that vary laterally and vertically within the lithosphere of the Cordillera and the North American craton. However, future investigation of seismic anisotropy is required to further constrain our understanding of these complex flow patterns and their influence on local and regional dynamic processes within the lithospheric domains of the Cordillera and North American craton and at the boundary between them.

Chapter 3: Methods

3.1 Numerical Modelling Approach

Numerical modelling for this study are conducted using SOPALE, a two-dimensional, plane-strain finite element (FE) code [*Fullsack*, 1995; *Beaumont et al.*, 2006]. The finite element algorithm uses an arbitrary Lagrangian-Eulerian (ALE) method to calculate large-scale deformation of the lithosphere, which is mathematically represented as viscous-plastic Stokes flow [*Fullsack*, 1995]. The ALE method combines the Lagrangian and Eulerian descriptions of motion of continuum mechanics. The Lagrangian description of motion uses a reference frame which tracks the motion of a particle in a continuum by recording the particle's initial position (x) at some time (t), and then records its new position ($x + \Delta x$) at a later time ($t + \Delta t$) [*Malvern*, 1969]. In FE computations, the Lagrangian reference frame has several advantages; it allows for irregular geometry, tracking of material interfaces and easily enables free-slip boundary conditions [*Fullsack*, 1995; *Duarte et al.*, 2004]. However, because the Lagrangian reference frame results in deformation of the Lagrangian mesh, instabilities arise when calculations involve large deformations within the domain of the model [*Fullsack*, 1995; *Duarte et al.*, 2004].

Conversely, in the Eulerian description of motion, the reference frame is fixed in space, and therefore the mesh is rigid and does not undergo deformation over time [*Malvern*, 1969; *Duarte et al.*, 2004]. When compared to the Lagrangian description of motion, the Eulerian mesh can be used to model large deformations [*Fullsack*, 1995; *Duarte et al.*, 2004]. However, because the reference frame is fixed at a point in space, two unfortunate consequences arise; 1) material interfaces are not easily resolved, and 2) variable resolution in the model domain is difficult to implement in comparison to the Lagrangian method [*Fullsack*, 1995; *Duarte et al.*, 2004].

The ALE algorithm used in SOPALE provides the advantage of combining the material tracking capabilities of the Lagrangian method with the large deformation capabilities of the Eulerian method. The Eulerian mesh, which is fixed in space, is used to solve the constitutive equations of mass, momentum and energy, described below [*Fullsack*, 1995; *Beaumont et al.*, 1996]. The Eulerian mesh consists of quadrilateral elements, with a node positioned at each vertex. The horizontal position of the nodes remains fixed in space, and the horizontal resolution is constant over the model domain [*Fullsack*, 1995]. The side boundaries and bottom boundary of the Eulerian mesh are fixed. When a stress-free boundary is used for the top surface (as in the models in this study), topography can develop along the top boundary, resulting in vertical dilation of elements [*Fullsack*, 1995].

A Lagrangian pseudo mesh (so called here as it is not a true mesh) is used in order to track materials in the model domain [*Fullsack*, 1995]. The Lagrangian pseudo mesh consists of a cloud of points, such that each point represents a material particle in the model domain [*Fullsack*, 1995; *Beaumont et al.*, 1996]. A specified number of Lagrangian particles are assigned to each element in the Eulerian mesh. When distortion of the particles reduces the number of Lagrangian particles in an Eulerian element, particles are injected into the model domain to maintain a minimum number of particles within each element [*Fullsack*, 1995]. For example, in the present study, a minimum of three Lagrangian particles are required in each Eulerian element; if the number of Lagrangian particles is less than three, four new Lagrangian particles (two along the horizontal edge and two along the vertical edge) are injected into the Eulerian element. The newly injected particles are assigned the thermal and material properties of the Eulerian element into which they have been injected.

At each time step, Eulerian velocities combined with applied boundary conditions are used to advect the Lagrangian particles. This information is then used to update materials within the Eulerian mesh [*Fullsack*, 1995]. Thus the Eulerian and Lagrangian meshes are iteratively re-gridded via interpolation of their respective nodal values [*Fullsack*, 1995]. The rheological properties of a given Eulerian element are updated using a "majority" rule which is dictated by the Lagrangian particles contained within said element; the density of the element is the average density of the Lagrangian particles [*Fullsack*, 1995]. Because particles are tracked by the Lagrangian pseudo mesh it is possible to model large magnitudes of particle displacement, provided these displacements do not exceed resolution of the Eulerian mesh in a single time step, thus surface processes such as erosion and deposition can also be calculated with relative ease [*Fullsack*, 1995]. It is important to note that the described method for calculating material advection in SOPALE is also applied to the calculation of the thermal field [*Fullsack*, 1995].

3.2 Governing Equations

As mentioned previously, the SOPALE code solves the viscous-plastic Stokes flow equations for creeping flows [*Fullsack*, 1995; *Pysklywec et al.*, 2010b]. The system is governed by the equations of the conservation of mass, momentum and energy. The conservation of mass is described by the continuity equation, which is given by:

$$\frac{d\rho}{dt} + \rho \frac{\partial v_i}{\partial x_i} = 0 \qquad (3.1)$$

where ρ is the density, t is time, $\partial v_i/\partial x_i$ is the divergence of the velocity field (v_i). The index i is the component of the velocity field (i=1,2 for the 2D model) and repeating indices imply summation The SOPALE code makes use of the incompressibility assumption, which states that

the density of a material point (i.e. a Lagrangian particle) does not change over time [*Gerya*, 2010]. With this assumption, equation (3.1) reduces to:

$$\frac{\partial v_i}{\partial x_i} = 0 \tag{3.2}$$

If volume-changing phase transitions are absent and pressure and temperature changes are not very large, then the assumption of incompressibility is valid for numerical geodynamic models; however, it should be noted that this assumption results in a simplification of the modelled system [*Gerya*, 2010].

The conservation of momentum is described by the momentum equation:

$$\frac{\partial \sigma_{ij}}{\partial x_j} + \rho g_2 = \rho \frac{dv_i}{dt} \tag{3.3}$$

where σ_{ij} is the stress tensor, x_j is the position, ρ is the density, and g_2 is the downward acceleration of gravity. The SOPALE code assumes static equilibrium, which implies that the internal acceleration of the system is negligible, and thus equation (3) reduces to the form shown in Equation (4) below.

$$\frac{\partial \sigma_{ij}}{\partial x_j} + \rho g_i = 0 \tag{3.4}$$

The assumption of static equilibrium is valid for highly viscous flows, like the Earth's lithosphere over time scales of millions of years, in which gravitational forces and the viscosity are large enough to render the system's internal acceleration negligible [*Gerya*, 2010].

Conservation of energy is described by;

$$\rho c_p \left(\frac{\partial T}{\partial t} + v_i \frac{\partial T}{\partial x_i}\right) = k \frac{\partial^2 T}{\partial x_i^2} + A + \sigma'_{ij} \dot{\varepsilon}_{ij} + v_2 \alpha g T \rho \tag{3.5}$$

where c_p is the specific heat capacity at a constant temperature, T is absolute temperature, k is the thermal conductivity, A is the radiogenic heat production, and α is the volumetric coefficient of thermal expansion. The term on the left hand side of Equation 3.5 represents the change in temperature over time $(\partial T/\partial t)$ and the heat advection $(v_i\,\partial T/\partial x_i)$. The first term on the right hand side of Equation 3.5 is the heat conduction. The second term represents radiogenic heat production from decay of radioactive elements in the material (A). Shear heat production, which results from dissipation of mechanical energy as heat that occurs during material deformation, can be described as the product of the deviatoric stress (σ'_{ij}) and strain rate ($\dot{\varepsilon}_{ij}$) and is represented by the third term in Equation 3.5, [*Currie and van Wijk*, 2016; *Huismans and Beaumont*, 2003]. An adiabatic temperature gradient is used to calculate the temperature at the base of the model domain, and this temperature is imposed as a boundary condition on the model domain. Therefore, because the SOPALE code assumes incompressibility, the last term on the right-hand side of Equation 3.5 is used to correct for adiabatic heating (i.e. heat transport is purely convective) resulting from material that moves vertically with velocity v_2 [*Currie and van Wijk*, 2016; *Beaumont and Ings*, 2012].

At each time step, Equation 3.5 is used to calculate the evolution of the temperature field in the models and Equation 3.2 and 3.3 are used to calculate the mechanical evolution (i.e., velocity and stress fields). It should be noted that the thermal and mechanical fields are coupled, as the model includes materials with a viscous rheology (see below), material movement redistributes radiogenic heat production, and deformation causes shear heating [*Beaumont and Ings*, 2012; *Currie and van Wijk*, 2016].

3.3 Rheology and Density Equations

All materials undergo frictional-plastic and viscous deformation. At each time step the deformation style is determined in SOPALE by calculating both frictional plastic and viscous yield stress; the lesser of the two values at each node determines the deviatoric stress, and thus the mode of deformation [*Pysklywec et al.*, 2010a]. The stress tensor here is defined as:

$$\sigma_{ij} = -P\delta_{ij} + \sigma'_{ij} = -P\delta_{ij} + 2\eta_{eff}\dot{\varepsilon}_{ij} \tag{3.6}$$

where P is the pressure, σ'_{ij} is the deviatoric stress, δ_{ij} is the Kronecker delta, η_{eff} is the effective viscosity, and $\dot{\varepsilon}_{ij}$ is the strain rate tensor, which is given by:

$$\dot{\varepsilon}_{ij} = \frac{1}{2}\left(\frac{\partial u_i}{\partial x_i} + \frac{\partial u_j}{\partial x_j}\right) \tag{3.7}$$

Frictional plastic yield stresses (σ_y) are used at shallower depths where deviatoric stresses are high; under such conditions deformation occurs via brittle failure, and stress calculated using the Drucker-Prager yield criterion, defined as;

$$\sigma_y = (J_2')^{1/2} = C\cos\phi_{eff} + P\sin\phi_{eff} \tag{3.8}$$

where Φ_{eff} is the internal angle of friction and c_o is the material cohesion [*Beaumont and Ings*, 2012; *Currie and van Wijk*, 2016]. It should be noted that deformation in SOPALE is modelled as viscous creep; thus, brittle deformation is represented by a narrow viscous shear band over the width of 1-2 elements, and the yield stress is used to calculate an effective viscosity [*Fullsack*, 1995; *Beaumont et al.*, 2006].

At greater depths, deviatoric stress is reduced, and thus materials behave viscously. The viscous yield stress (σ_v) is defined by;

$$\sigma_v = 2\eta_{eff}\dot{I}_2 \tag{3.9}$$

where $\dot{I}_2$ is the second invariant of the strain rate tensor and η_{eff} is the effective viscosity. The effective viscosity is calculated in SOPALE using a power law expression for dislocation creep, which is given by;

$$\eta_{eff} = f(B^*)\dot{I}_2^{(1-n)/2n} exp\left[\frac{(Q+PV^*)}{nRT}\right] \tag{3.10}$$

where B^* is pre-exponential factor, Q is activation energy, P is pressure, V^* is activation volume, n is stress exponent, R is the gas constant, T is the temperature, f is a viscosity scaling factor that linearly scales the viscosity relative to experimentally derived values [*Currie and van Wijk*, 2016.; *Beaumont et al.*, 2006; *Pysklywec et al.*, 2010b]. This approach allows for the consistent use of well-constrained, experimentally derived flow laws, such that materials with rheologies that are weaker or stronger than the reference material can be represented by using the viscosity scaling factor (f) to reflect differences in rheological behaviour, without necessitating the use of additional parameters [*Beaumont et al.*, 2006]. As described in detail by *Beaumont et al.* [2006], the use of the viscosity scaling factor is understood to be representative of differences in bulk composition or water content in the modelled materials [*Beaumont et al.*, 2006].

Because flow laws are experimentally derived, values often reported in terms of uniaxial laboratory conditions, in which the effective viscosity (η_{eff}) is given by;

$$\eta_{eff} = \frac{1}{2}\left(\frac{3^{(n+1)/2}}{2}A_{uni}\right)^{-1/n} \dot{I}_2^{(1-n)/2n} exp\left[\frac{Q+PV^*}{nRT}\right] \tag{3.11}$$

where A_{uni} is the uniaxial pre-exponential factor that is obtained from the laboratory deformation experiments. In contrast, the 2D SOPALE models assumes plane strain conditions.

Therefore, the pre-exponential factor B^* in Equation 3.10 is used to convert the experimental pre-exponential factor (A_{uni}) into a plane strain pre-exponential factor (A_{ps}) [*Beaumont et al.*, 2006]. Equation (3.13) gives the relationship between the pre-exponential factors used in SOPALE flow laws (B^*), uniaxial flow laws (A_{uni}) and plane strain flow laws (A_{ps}), as shown below in Equation (3.12).

$$B^* = \tfrac{1}{2}{A_{ps}}^{-1/n} = \left[\frac{3^{(n+1)/2}}{2}\right]^{-1/n} {A_{uni}}^{-1/n} \tag{3.12}$$

For the present study, the rheology of mantle material is defined by the flow law of *Hirth and Kohlstedt* [2003] for dislocation creep of wet olivine, which includes a term for water content. The pre-exponential factor used here follows *Currie and van Wijk* [2016];

$$B^* = \frac{1}{2}\left[\frac{3^{(n+1)/2}}{2}\right]^{-1/n} (A_{uni}{C_{OH}}^{r})^{\frac{-1}{n}} \tag{3.13}$$

where C_{OH} is the water content of the material measured in ppm H/Si and r is the water content exponent. Thus, the pre-exponential factor allows for the water content of the material to be varied [*Currie and van Wijk*, 2016].

Material densities in the system are temperature dependent. At temperature T, the density is given by:

$$\rho = \rho_o\big(1 - \alpha(T - T_o)\big) \tag{3.14}$$

where ρ_o is a reference density, α is the coefficient of thermal expansion, T_o is the reference temperature.

3.4 Rheological Parameters for Model Materials

The rheological parameters of each material in the reference model are given in Table 3.1. The plastic deformation parameters follow those used in previous SOPALE studies [e.g., *Beaumont et al.*, 2006; *Beaumont and Ings*, 2012; *Currie and van Wijk*, 2016]. Strain softening, which occurs when a materials strength decreases through time in response to continuous plastic shear strain, is incorporated into the modelled rheologies by linearly scaling the internal friction angle (Φ_{eff},) of Equation 3.8 [*Huismans and Beaumont*, 2003].

All of the viscous rheologies are based on flow law parameters from well-known laboratory experiments that have been extensively benchmarked for use with the SOPALE code [*Beaumont et al.*, 2006]. The upper crust is modelled using the wet Black Hills quartzite rheology of *Gleason and Tullis* [1995]. An effective viscosity scaling factor of $f = 5$ is used to reflect the fact that in general the upper crust contains minerals more mafic than quartz and is less hydrated than wet quartz [*Beaumont et al.*, 2006]. The dry Maryland diabase of *Mackwell et al.* [1998] is used to represent the rheology of the lower crust with a viscosity scaling factor $f = 0.1$, which benchmarked in SOPALE, and is found to closely resemble the rheological behaviour of a granulite with an intermediate composition [*Beaumont et al.*, 2006]. The mantle lithosphere and sub-lithospheric mantle are modelled using rheology values reported from laboratory experiments on synthetic olivine aggregates by *Hirth and Kohlstedt* [2003]. As noted above, this flow law includes a term for water content. As a reference, it is assumed that the mantle is partially hydrated, with a water content of 1000 ppm H/Si. It should be emphasized that this does not imply that the mantle lithosphere is composed entirely of olivine. However, olivine represents ~60% or more of the modal mineralogy of mantle rocks and is therefore considered the rate-determining mineral for diffusion creep in the mantle [*Bürgmann and Dresen*, 2008].

The mantle lithosphere of the left (Cordillera) and right (craton) hand sides of the model domain are assigned a reference density of ρ = 3250 kg/m^3 and a viscosity scaling factor of f = 1.

Table 3.1: Viscous and plastic rheology material properties used in the reference model for model experiments

Parameter	**Upper Crust**	**Lower Crust**	**Mantle Lithosphere**	**Sub-Lithospheric Mantle**
Viscous Rheology				
Stress Exponent; n	4.0	4.7	3.5	3.5
Uniaxial Pre-Exponential Factor; A_{uni} (Pa^{-n}/s)	1.10×10^{-28}	5.05×10^{-28}	9.00×10^{-20}	9.00×10^{-20}
Plane Strain Pre-Exponential Factor; A_{ps} (Pa^{-n}/s)	8.57×10^{-28}	5.78×10^{-27}	2.12×10^{-15}	2.12×10^{-15}
Pre-Exponential Factor; B^* (Pa·s$^{1/n}$)	2.92×10^{6}	1.91×10^{5}	7.79×10^{3}	7.79×10^{3}
Activation Energy; Q (J/mol)	223000	485000	480000	480000
Activation Volume; V^*(m^3/mol)	N/A	N/A	1.1×10^{-5}	1.1×10^{-5}
Viscosity Scaling Factor(f)	5.0	0.1	1	1
Plastic Rheology				
Cohesion C_o	20	0	0	0
Effective Internal Angle of Friction; ϕ_{eff}	15-2°	15-2°	15-2°	15-2°

Table 3.2: Thermal properties used for the reference model

Parameter	Upper Crust	Lower Crust	Mantle Lithosphere	Sub-lithospheric Mantle
Thermal Parameters				
Thermal Conductivity; k (W/m·K)	2.5	2.5	2.5	2.5
Heat Production; A ($\mu W/m^3$)	1.1	0.4	0	0
Specific Heat; c_p (J/kg·K)	1250	1250	1250	1250
Temperature Dependent Density				
Reference Density at T_o; ρ_o (kg/m^3)	2800	3000	3250	3250
Reference Temperature; T_o (°C)	627	627	1327	1327
Volumetric Thermal Expansion Coefficient; α (K^{-1})	3.0×10^{-5}	3.0×10^{-5}	3.0×10^{-5}	3.0×10^{-5}

3.5 Boundary and Initial Conditions

The initial geometry of the numerical models for this study is shown in Figure 3.1. The model domain is 2400 km in length and extends to a depth of 900 km. Across the entirety of the model domain, the upper and lower crust were assigned constant thicknesses of 20 km and 15 km, respectively. Although in reality the craton has a crustal thickness of ~10 km greater than the Cordillera (see Section 2.4.1), a uniform crustal thickness is chosen to simplify the model and

isolate the effects of differing mantle lithosphere thickness and rheology at the boundary between the Cordillera and North American craton. The mantle lithosphere on the left hand side of the model domain corresponds to the Cordillera and has a thickness of 25 km, whereas the mantle lithosphere on the right hand side of the model domain corresponds to the North American craton and has a thickness of 215 km. Thus, the Cordillera and North American craton have total lithosphere thicknesses of 60 km and 250 km. respectively, and a step in the lithosphere of 190 km occurs at the boundary. An initially vertical craton margin geometry was used for simplicity in the model design, as well as to preclude an initially west dipping margin geometry that is simply maintained during the experiments. These initial lithosphere thicknesses are consistent with observations from geophysical data discussed in Chapter 2.

The models use an Eulerian mesh that has a horizontal resolution of 10 km over the whole model domain, whereas the vertical resolution decreases with depth. The upper 50 km has a resolution of 2.5 km, decreasing to 5 km from 50-400 km depth and then decreasing to 15 km resolution from 400-700 km. Finally, a 20 km resolution is used in the bottom 200 km of the model domain, which extends to a total depth of 900 km.

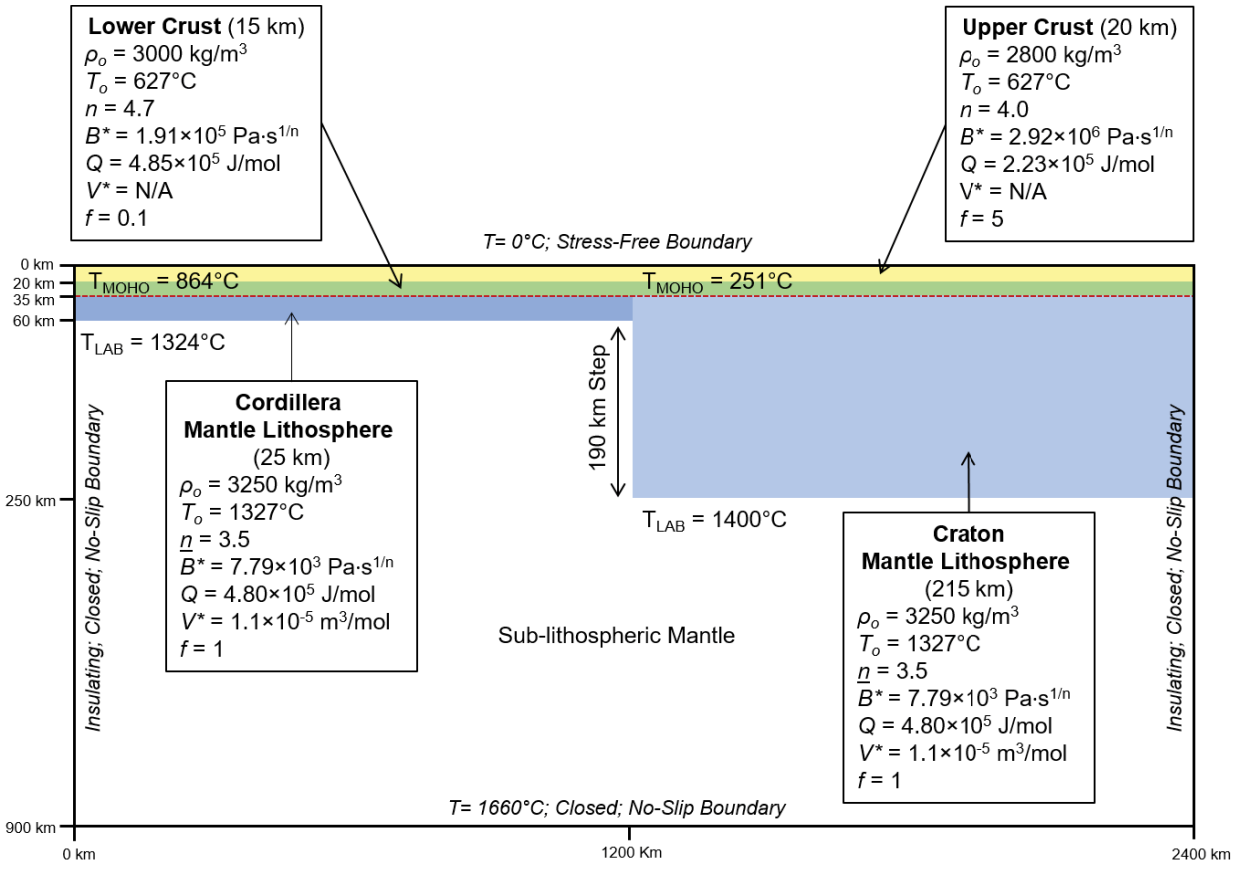

Figure 3.1: Initial geometry, boundary conditions and material parameters used in the reference model. The upper crust is shown in yellow, the lower crust is shown in green, and the mantle lithosphere is shown in blue and light blue for the Cordillera and craton, respectively. The location of the modelled Moho is indicated by a dashed red line. Note that a vertical exaggeration of 5:1 is used.

Numerical experiments are conducted in two phases; an initialization phase, followed by an experimental phase. During the initialization phase, the 2D thermal structure is computed and the model domain is isostatically balanced. The temperature structure is calculated based on material thermal properties and assigned boundary conditions (Figure 3.1). The thermal properties of the Cordillera lithosphere (crust and mantle) are given in Table 3.2. For the craton, an artificially high thermal conductivity of k = 5.989 W/m·K is assigned to the upper crust, lower crust and mantle lithosphere. This conductivity is chosen in order to create an initial geothermal gradient that is compatible with the 250 km lithosphere thickness (i.e., the base of the lithosphere coincides with the adiabatic mantle temperature at this depth). This approach is needed because

the SOPALE code does not permit lateral heat flux variations from the sub-lithospheric mantle, which is assigned a value of 32 W/m·K. After the initial thermal structure is calculated, the model is run for 200 Ka in order to allow for isostatic adjustment. For this, a free-slip boundary is applied to the right hand side of the model domain. The free slip condition allows the craton to sink, owing to its cooler temperatures and thus higher density than the adjacent mantle. In the reference model, the craton sinks by ~3.5 km, creating a topographic step at the Cordillera-craton boundary.

After the initialization phase, the thermal conductivity of materials in the craton and Cordillera is assigned a value of k = 2.5 W/m·K, as shown in Table 3.2. Both the left and right hand sides of the model are assigned to be no-slip boundaries, which are thermally insulated. This means that there is no heat flux through the sides of the model domain. The base of the model domain is also assigned a no-slip boundary, and a temperature of 1660°C, which corresponds to the adiabatic temperature at 900 km depth. The top surface of the model has a fixed temperature of 0°C and is stress free. This means that both horizontal and vertical velocities are permitted on this boundary. This condition allows for the formation and evolution of topography during the experiments.

Numerical modelling experiments are then carried out to observe how the thermal and rheological transition from the Cordillera to the craton margin changes over time. Two aspects are of particular interest: (1) the stability of the craton margin (i.e., can a sharp change in lithosphere thickness be maintained) and (2) is there a set of conditions under which the step between the Cordillera and craton evolves to a west-dipping (i.e. toward the Cordillera) geometry, as suggested by the seismic observations (see Section 1.1). For this, a range of densities and viscosity scaling factors are applied to the craton mantle lithosphere, representing

varying degrees of chemical depletion and dehydration, respectively. The effects of dynamic processes, such as mantle wind and crustal shortening, on the geometry of the lithosphere step are also examined. In total approximately 400 numerical modelling experiments are conducted and numerical solutions are calculated over 200 Ma of geologic time. A time scale of 200 Ma is chosen to reflect the onset of subduction along the Cascadia subduction zone [*Monger and Price*, 2002; *Dickinson*, 2004].

Chapter 4: Model Results

4.1 Overview of Models

The numerical modelling results from this study focus on how the geometry of the craton margin evolves through time. The results of the reference model are presented first to examine effects related to gravitational instability of the lithosphere. Then a series of modelling experiments are presented to emphasize the effects of varying the viscous strength and density of the craton mantle lithosphere relative to the surrounding sub-lithospheric mantle. Then the response and sensitivity of the craton margin to large-scale horizontal mantle flow (mantle wind) and crustal shortening are considered.

For each model, the craton margin geometry is quantified by measuring its dip relative to the horizontal (see Figure 4.1). The dip of the craton mantle lithosphere is measured primarily by considering the orientation of the 1300°C isotherm between 100 km and 220 km depth at the westward margin of the craton, which is coincident with the material boundary in most cases (i.e. the boundary between particles of cratonic mantle lithosphere and sub-lithospheric mantle). Exceptions occur when material that is dripping away from the craton margin causes significant deflection of the 1300°C isotherm in a way that does not reflect the geometry of the materially-defined craton margin. In such cases the material boundary is used to measure dip angles. This approach is used for two reasons: 1) it ensures consistency in angle measurements, which allows for direct comparison between individual numerical models; and 2) within the upper mantle, seismic velocities are highly sensitivity to temperature, whereas the effects of composition can be considered secondary [*Goes and Van Der Lee*, 2002; *Cammarano et al.*, 2003], which is important when comparing the numerical models with seismic tomography models.

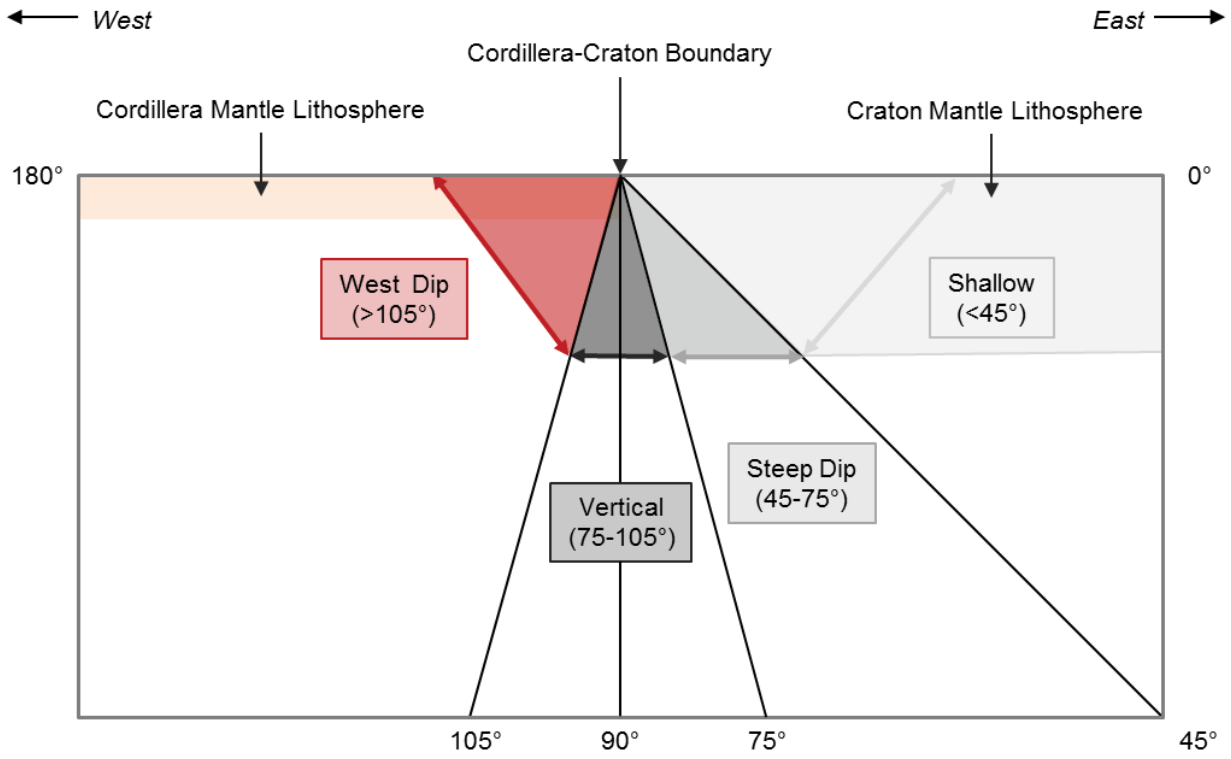

Figure 4.1: Schematic diagram showing the classification system used for measuring craton margin dips. Craton margins whose dips are <75° are considered east dipping. East dipping craton margins have been further sub-divided into shallow (<45°) and steep (45-75°). A craton margin whose dip is 75-105° is considered vertical and only craton margins with dips exceeding 105° are considered west-dipping. Note that east and west directions correspond to the right and left hand sides of the mode, respectively, and that the initial position of the Cordillera-craton boundary used to delineate east and west directions. The colour scheme assigned here to each dip category is used in subsequent figures; light grey = shallow (<45°), grey = steep (45-74°), black = vertical (75-105°), red = west dipping (>105°).

Craton margin dip measurements are classified into four categories which are shown schematically in Figure 4.1: 1) craton margins that dip eastward (i.e. toward the right hand side of the model domain) at angles <45° relative to the surface are considered shallow; 2) eastward dip angles that fall between 45 and 75° are considered steep; 3) dip angles between 75 and 105° are considered vertical; and 4) craton margins with dip angles >105° are considered as west-dipping. The use of categorized dip angles as opposed to exact measurements is deliberate; resolution disparities between the seismic tomography models of *Chen et al.* [submitted manuscript 2016] and the numerical models of this study do not allow for direct comparison of

precisely measures angles. Thus, categories are used to avoid inappropriate comparisons between numerical models and tomography models.

4.2 Reference Model

The results for the reference model, which uses the parameters given in Tables 3.1 and 3.2, are shown in Figure 4.2. It is important to note that in the reference model there is no difference in rheological parameters or density between the craton mantle lithosphere and the surrounding mantle materials (i.e. the sub-lithospheric mantle and Cordillera mantle lithosphere). Furthermore, there are no velocities imposed on boundaries of the model, and thus motion of material throughout the evolution of the model is a direct result of thermally-induced convection.

At t = 0 Ma, a convection cell has already initiated in the sub-lithospheric mantle of the reference model and the most vigorous flow is concentrated at the sharp edge of the craton mantle lithosphere. The concentration of flow at the edge of the craton mantle lithosphere is caused by the lateral temperature gradient between the craton and the surrounding sub-lithospheric mantle [*King and Anderson*, 1998]. The cold temperatures in the craton mantle lithosphere create gravitational instability, as thermal contraction makes the craton mantle lithosphere denser than the underlying sub-lithospheric mantle by approximately +52 kg/m^3 (compared to approximately +22 kg/m^3 for the Cordillera). This results in edge-driven convection, with downwelling of cold material along the edge of the craton mantle lithosphere and upwelling of hot material below the Cordillera mantle lithosphere [*King and Anderson*, 1998]. Thus a clockwise convection cell forms at the step in the lithosphere. By 50 Ma, the craton mantle lithosphere has undergone extensive erosion caused by downwelling of thermally unstable craton mantle lithosphere. The dip of the craton margin has been reduced to <45°, and thinning of the mantle lithosphere by ~50 km is seen not only at the craton margin, but up to

~200 km inboard of the craton. By contrast, the mantle lithosphere of the Cordillera remains comparatively intact; minor thinning and downwelling of mantle lithosphere material only occurs close to the craton margin, where edge-driven convection occurs.

Thinning of the craton mantle lithosphere by 50 km or more is pervasive at 100 Ma of model evolution, extending ~600 km into the craton and convection at the edge of the craton margin has further decreased the dip angle of the craton margin. At t = 150 Ma, thinning of the craton mantle lithosphere extends 800 km inboard of the craton margin, with the greatest degree of thinning occurring within 300 km of the boundary between the craton and Cordillera lithosphere. By 200 Ma of model evolution, the mantle lithosphere of the craton has been thinned by ~50-100 km or more over its entire lateral extent, as convection cells in the sub-lithospheric mantle have migrated away from the initial position of the craton margin and toward the interior of the continent. Interestingly, due to its high temperature (and thus minor thermal density contrast), the Cordillera mantle lithosphere remains largely intact. The dip angle of the craton margin remains shallow throughout the evolution of the reference model, dipping below 45° after less than 20 Ma.

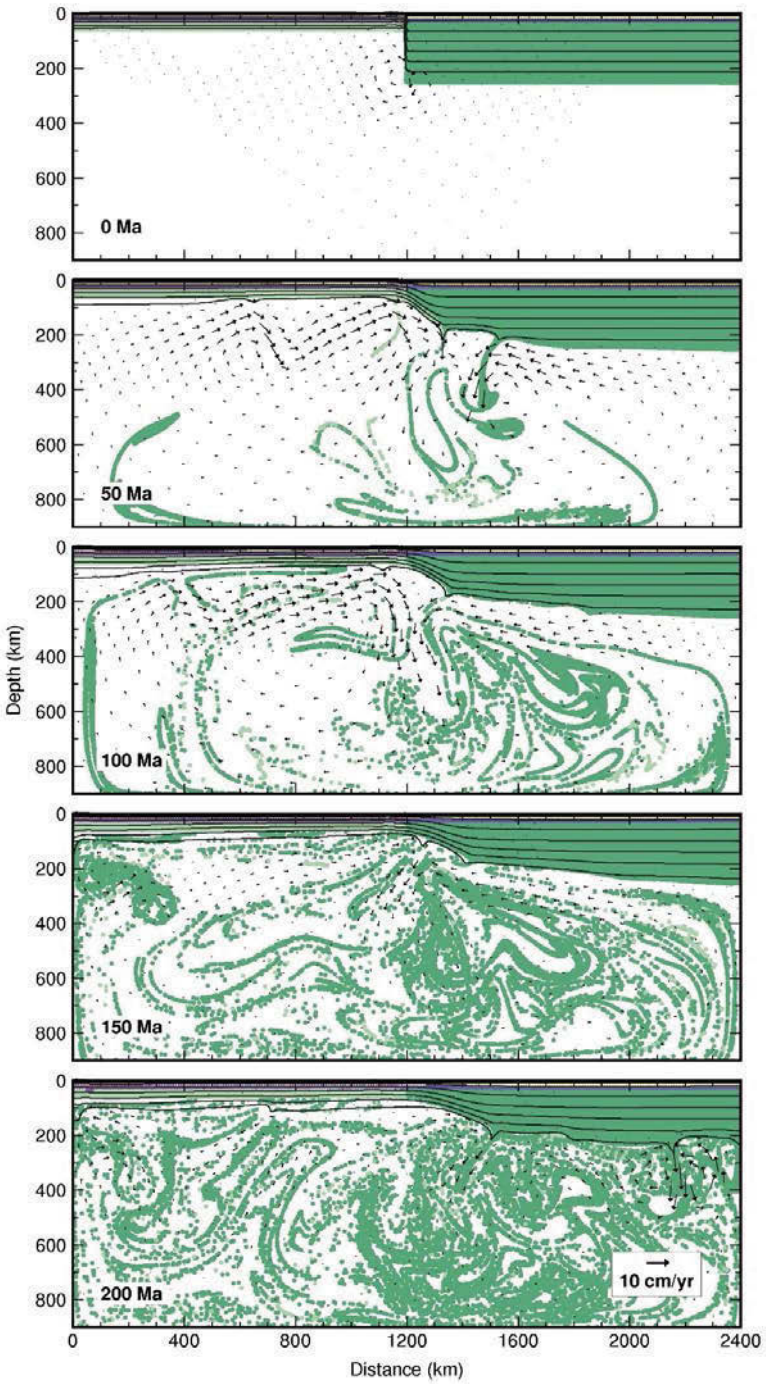

Figure 4.2: Evolution of the reference model over 200 Ma shown at 50 Ma intervals. Colours represent materials assigned to the model domain as outlined in Tables 3.1 and 3.2; the upper crust is shown in yellow, the lower crust is shown in purple, and the mantle lithosphere is shown in green. The scale for the material velocity vectors (black arrows) is shown in the white box in the bottom right-hand corner. Temperature contours are shown as black lines at 200°C intervals.

4.3 The Effects of Strong Mantle Lithosphere

In the reference model, the initially vertical boundary between the Cordillera and craton is rapidly erased by thermal convection. After 50-100 Ma, the transition from thin to thick lithosphere occurs over a lateral distance of ~300 km, with the boundary dipping eastward (i.e. toward the interior of the craton, refer to Figure 4.1). This is inconsistent with seismic data of the craton edge in western Canada and other places, which show a sub-vertical lithosphere step [*Currie and Wijk*, 2016, and references therein] or one which dips westward (Figure 1.2). Therefore; numerical modelling experiments are conducted in which the strength of the craton mantle lithosphere is increased, in order to determine if a higher viscosity can prevent the convection-driven erosion of the lithosphere step seen in the reference model (Figure 4.2).

The reference model uses a damp olivine rheology for the mantle lithosphere, which has a water content of 1000 ppm H/Si. The viscous strength of olivine increases as the water content decreases [*Hirth and Kohlstedt*, 2003], as shown in Figure 4.3a. Xenolith and other data suggest that the mantle lithosphere below cratons may be relatively dry [*Karato*, 2010; *Wang*, 2010]. The models presented below investigate the effect of drier (and therefore stronger) craton mantle lithosphere by using the scaling factor of Equation 3.11 to linearly increase the effective viscosity. In these experiments, the relative strength of the craton mantle lithosphere is varied relative to the reference value by factors of 2, 5, 10, 15 and 20. The relationship between the scaling factor used in the numerical models and the water content of olivine is shown in Figure 4.3b, and indicates that a dry olivine rheology is ~5-40 times stronger than the reference damp olivine.

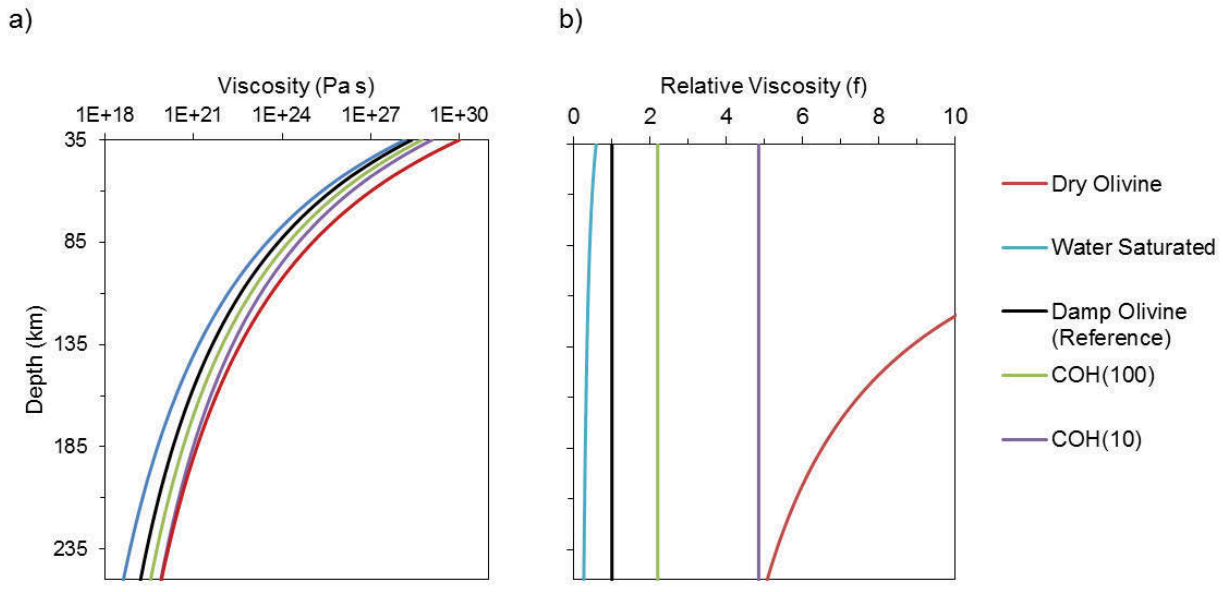

Figure 4.3: a) The relationship between effective viscosity and water content of olivine (concentration of OH in ppm H/Si) given in the numerical modelling experiments for this study. b) The relationship between the viscosity scaling factor (*f*) of Equation 3.11 and the water content of olivine (C_{OH}=1000 ppm H/Si); this is calculated by dividing the viscosity profile for each water content by the reference damp olivine rheology. Calculations assume a craton geotherm and a strain rate of $1.0 \times 10^{-15} s^{-1}$.

The results for increasing the strength of the craton mantle lithosphere by factors of 5 and 20 are shown in Figure 4.4a and b, respectively. In comparison with the reference model, increased strength of the craton mantle lithosphere results in thermally-driven convection that is more spatially confined to the craton margin at 0 Ma, and convective flow velocities are significantly reduced. In particular, increased strength by a factor of 20, confines flow of material in the sub-lithospheric mantle is to the edge of the craton margin, only extending to a depth of ~250 km, and there is little deformation of the surrounding craton mantle lithosphere (Figure 4.4b, 0 Ma). At lower strengths, convection affects both the craton mantle lithosphere and the surrounding mantle (Figure 4.4a, 0 Ma). After 50 Ma, the craton margin maintains steep (45-75°) dip for strength increases by both a factor of 5 and 20; however, neither successfully maintains a vertical dip and no west-dipping margins are observed. When strength is increased by a factor of 5, a steep dip angle is maintained for 90 Ma, but dips shallowly by 100 Ma. In

contrast, increasing strength by a factor of 20 allows a vertical margin to persist for 30 Ma and a steep craton margin is maintained throughout the model evolution. Increased strength also results in less downwelling of craton mantle lithosphere material throughout the modelled time span. Therefore, the results of the numerical models suggest that two important consequences of strengthened craton mantle lithosphere are the persistence of both lithosphere thickness and a steeply dipping craton margin.

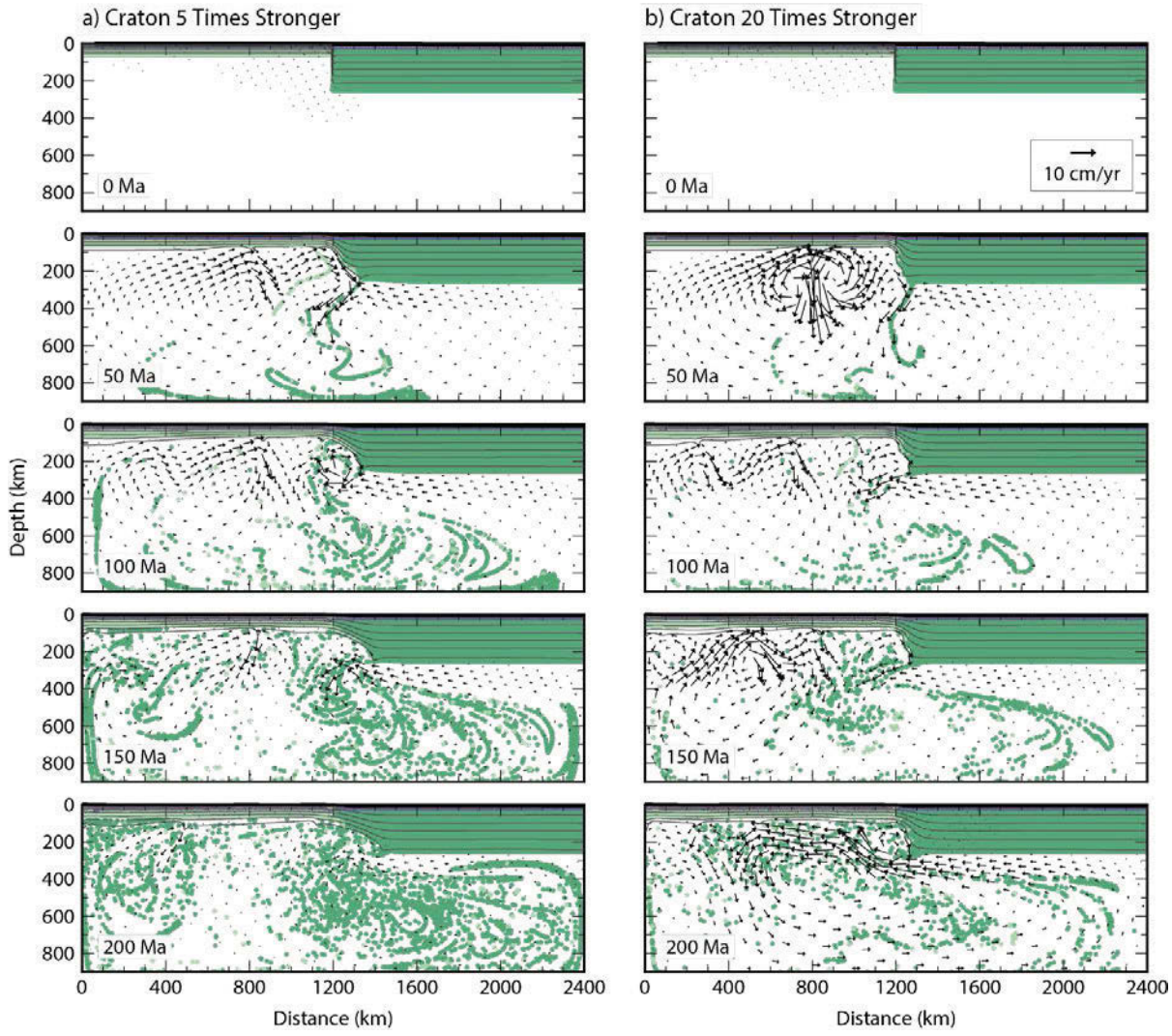

Figure 4.4: Results for increasing the relative strength of the craton mantle lithosphere by a factor of a) $f = 5$ and b) $f = 20$. Note that all other material/thermal parameters used are the same as those in the reference model (Table 3.1 and 3.2) and no velocity boundary conditions are imposed on the model, thus all velocities are a direct result of

thermally-induced mantle convection. The 10 cm/yr velocity vector shown in the white box in column b) at t = 0 Ma is included for scale.

A summary of the results for all strength values tested is shown in Figure 4.5. Vertical craton margins are only observed when the strength of the craton mantle lithosphere is greater than the surrounding mantle by a factor of 5 or more, and no west-dipping craton margins are observed for any of the tested strength values. Although a dry olivine rheology is 5-40 times stronger than the reference strength (Figure 4.3), it is unlikely that the craton mantle lithosphere is completely dry. Laboratory measurements of water contained in olivine from kimberlite mantle xenoliths indicate that the mantle lithosphere below cratons contains an average of ~17 ± 13 ppm H_20, which corresponds to ~270 ± 200 H/10^6Si [*Wang*, 2010] and a modelled strength factor of between 1 and 2 (Figure 4.3). However, *Karato* [2010] argues that because kimberlite magmas tend to be rich in volatiles, mantle xenoliths from kimberlites can overestimate cratonic mantle lithosphere water content, and that electrical conductivity and olivine fabrics are more consistent with water contents no greater than ~10 ppm H_2O (i.e. ~150 H/10^6Si or less) Therefore, despite the fact that a completely dry olivine rheology is up to ~40 times stronger than the reference damp olivine, strengths 5-20 times greater are probably more realistic for typical craton mantle lithosphere.

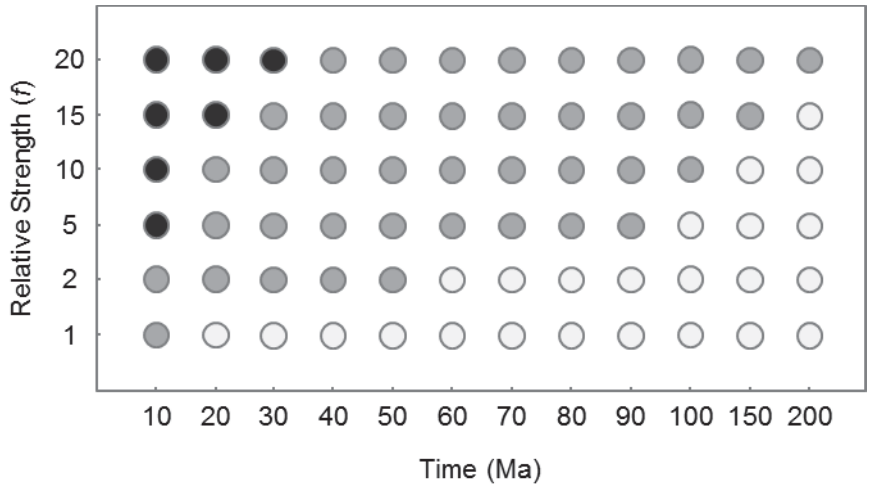

Figure 4.5: Measured dip angle of the craton margin through time for experiments in which the strength factor (viscosity scaling factor f of Equation 3.11) of the craton mantle lithosphere is increased. Light grey dots indicate shallow dip angles (<45°), grey dots indicate steep dip angles (45-75°) and black dots indicate vertical dip angles (75-105°). Note that when the reference density (3250 kg/m^3) is used, no west-dipping craton margins are observed for any of the tested strength values.

4.4 The Effects of Buoyant Mantle Lithosphere

Increasing the strength of the craton mantle lithosphere in the previous set of modelling experiments helped to increase the longevity of a steeply dipping craton margin and vertical geometries are observed when strength is increased by a factor of 5 or greater. However, none of the tested strength increases successfully maintains a vertical craton margin for more than 30 Ma and no west-dipping craton margins are observed (Figure 4.5). This is inconsistent with seismic data that suggests the craton margin has a nearly vertical to west-dipping geometry throughout the southern Canadian Cordillera (Figure 1.2); furthermore, it has been suggested that the craton margin has been stable for ~50 Ma or longer [*Bao et al.*, 2014]. Therefore, experiments are presented in which the density of the craton mantle lithosphere is reduced relative to the surrounding mantle to test the effects of increased mantle lithosphere buoyancy and to determine if buoyant mantle lithosphere can increase the durability of the craton margin and/or produce a west-dipping geometry.

Chemical depletion through metasomatic processes (e.g. partial melting) reduces the density of mantle lithosphere material, and the degree of mantle lithosphere depletion has been shown to increase with age [*Poudjom Djomani et al.*, 2001]. As discussed in Section 2.1, the tectonic domains of the North American craton that form the craton margin are of Archean and Proterozoic age. Geochemical studies of mantle xenoliths indicate that Archean aged craton mantle lithosphere becomes progressively depleted in iron relative to cratons of Proterozoic age; moreover, both show chemical depletion relative to a primitive mantle composition [*Poudjom Djomani et al.*, 2001, 2005]. Using the estimates of *Poudjom Djomani et al.* [2001], this corresponds to a density reduction of ~1.9-2.8% and ~0.6-1.7% for Archean and Proterozoic craton mantle (relative to primitive mantle) lithosphere, respectively.

In the present study, the reference density of the craton mantle lithosphere is decreased relative to the surrounding mantle lithosphere by 50 kg/m^3 in steps of 10 kg/m^3. This range of densities is equivalent to a density reduction of ~0.3-1.54% relative to the reference density (Table 3.1) or ~0.7-1.9% relative to a primitive mantle composition [*Poudjom Djomani et al.*, 2001]. Figure 4.6 shows the evolution of a craton margin that is 5 times stronger than the reference model for density reductions of 30 kg/m^3 (Figure 4.6a) and 50 kg/m^3 (Figure 4.6b). These models can be compared to the model in Figure 4.4a, in which the craton mantle lithosphere has a strength of $f = 5$ and the standard reference density. In all of these models, the craton mantle lithosphere is gravitationally unstable and the craton margin deforms during model evolution. However, density plays an important role in determining the fate of the detached material.

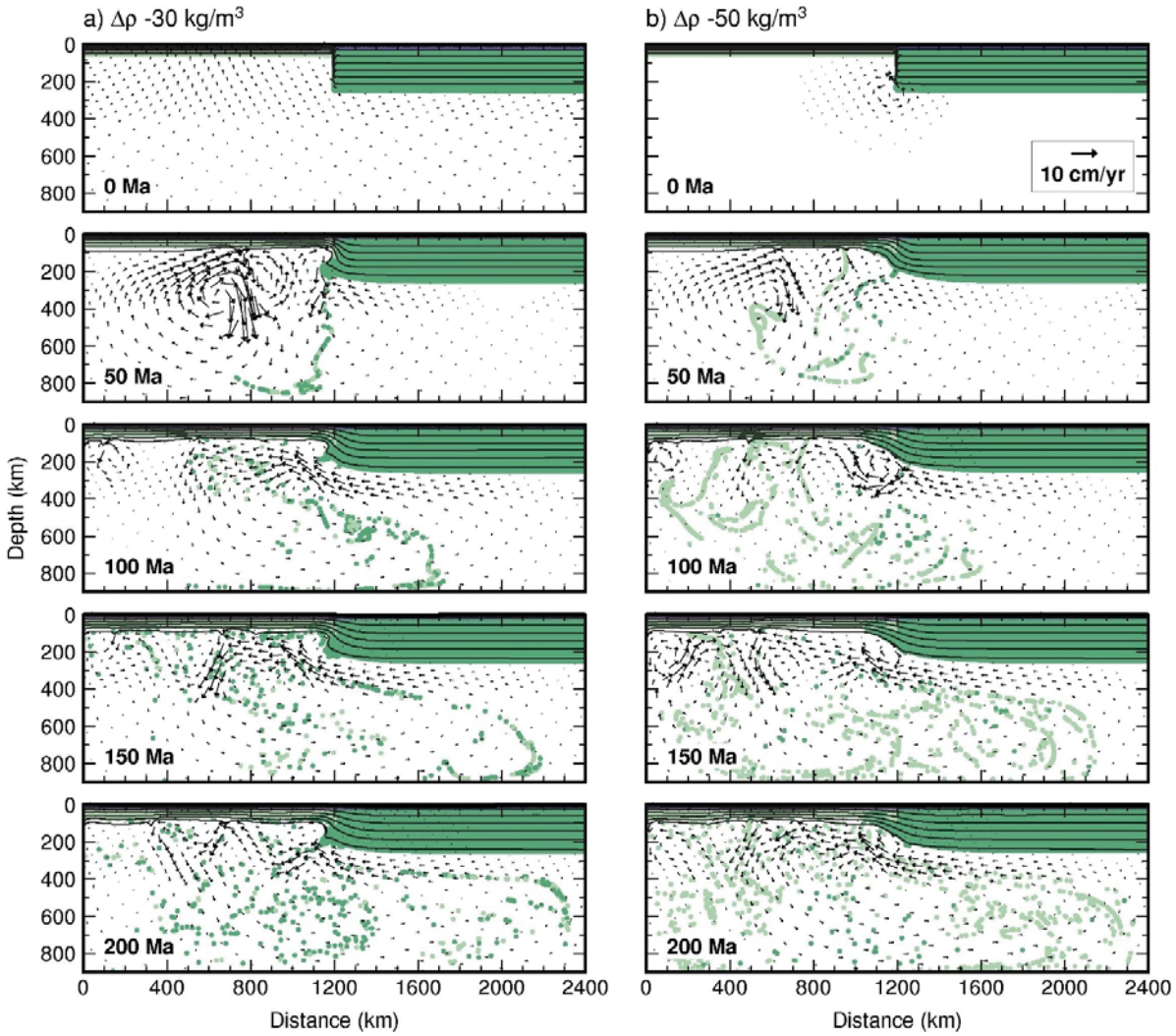

Figure 4.6: Results of numerical experiments for reducing density for a craton mantle lithosphere that is 5 times stronger than the reference model. a) The reference density reduced by 30 kg/m^3 and b) the reference density reduced by 50 kg/m^3. Note that the scale for velocity vectors in the models is given by the 10 cm/yr velocity vector in the white box located in the lower right-hand corner of column b) at t = 0 Ma.

For a craton mantle density that is 50 kg/m^3 less than the reference value, vigorous convection is observed along the craton margin at 0 Ma (Figure 4.6a). Although it maintains a steep angle, mantle lithosphere that is 50 kg/m^3 less dense than the sub-lithospheric mantle is too buoyant to sink downward. Thus, despite the fact that it is cold, the buoyant material upwells as it drips away from the craton margin and accumulates below the Cordillera mantle lithosphere, which becomes gravitationally unstable as a result. By 150 Ma, the upwelling buoyant material

has spread laterally to infill the step in the lithosphere reducing the craton margin to a shallow dip. Furthermore, the boundary between the Cordillera and craton has migrated westward by ~100-150 km. Westward migration of the boundary in the models may be significant, as it suggests the sub-surface location of the current Cordillera-craton boundary may not correspond to the present-day location of the boundary at the surface (i.e. the Rocky Mountain Trench/Tintina Fault system).

The results for an intermediate density reduction of 30 kg/m^3 (Figure 4.6b) exhibit a combination of the two end-member densities discussed above. Downwelling material is a mix of both Cordillera and craton mantle lithosphere. Less material is removed throughout the evolution of the numerical model compared to the reference density (Figure 4.4a) because the compositional reduction in density is large enough to counteract the increase in density caused by thermal contraction. Vigorous convection at the lithosphere step combined with increased buoyancy of the material successfully produces a west-dipping craton margin by 50 Ma. A small amount of upwelling material that has been removed from the edge of the craton margin begins to accumulate at the step in the lithosphere at 100 Ma; however, a westward dip is maintained throughout most of the evolution of the numerical model. Mantle lithosphere that is 30 kg/m^3 less dense that the reference density is too buoyant to quickly sink into the sub-lithospheric mantle, but it is also dense enough to prevent rapid upwelling (Figure 4.6a), as observed when density is reduced by as much as 50 kg/m^3(Figure 4.6b). The intermediate density value successfully produces and maintains a shallowly westward dipping craton margin over time scales >100 Ma, but the angle does not exceed ~115°.

The results of all numerical modelling experiments in which the density and relative strength of the craton mantle lithosphere are varied relative to the reference values are

summarized in Figure 4.7. Under the influence of thermal convection alone, the results suggest that relative to the reference model, both increased buoyancy and strength are required to produce and maintain near vertical to west-dipping craton margin geometries. Mantle lithosphere that is highly buoyant (i.e. -50 kg/m^3 relative to the reference value) causes upwelling at the craton edge and under-plating adjacent to the lithosphere step, which erodes the craton margin. Conversely, mantle lithosphere that is dense (i.e. the reference value) causes erosion of the craton margin via a downwelling Rayleigh-Taylor type instability. Similarly, if the craton mantle lithosphere is weak (i.e. $f \leq 2$), the craton margin is quickly eroded by thermal convection at the lithosphere step, and if the mantle lithosphere is too strong (i.e. $f \geq 15$) a west-dipping craton margin can not be produced, even if it is highly buoyant. Overall, the numerical models suggest that the optimal balance between buoyancy and strength for producing a west-dipping craton margin is when the craton mantle lithosphere is approximately 30 kg/m^3 less dense and ~5-15 times stronger than the reference values.

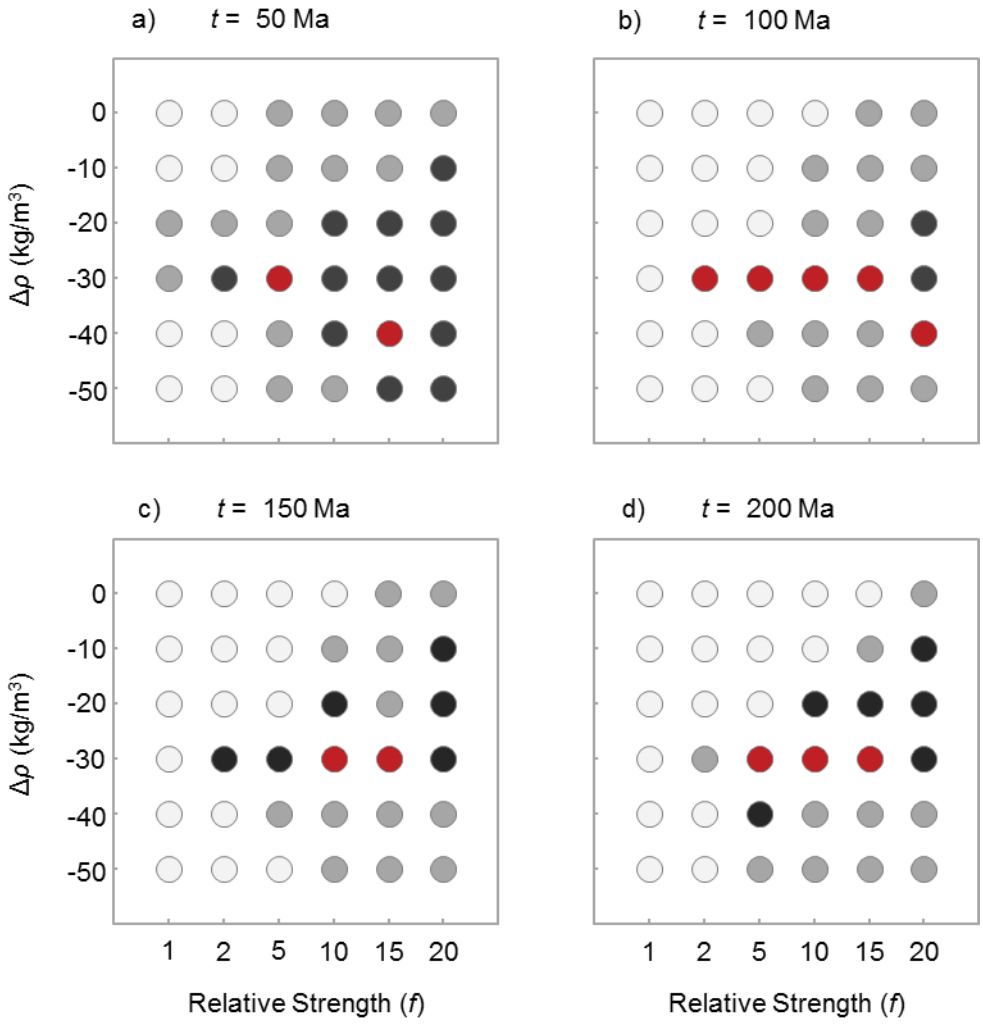

Figure 4.7: Diagrams summarizing the evolution of modelling experiments for all tested combinations of varying the density (*y*-axis) and strength (*x*-axis) of the craton mantle lithosphere relative to the reference model at; a) t = 50 Ma, b) t = 100 Ma, c) t = 150 Ma, and d) t = 200 Ma. Colours are used to indicate the dip angle of the craton margin; light grey circles represent shallow dip angles(<45°), grey circles represent steep dip angles (45-75°), black circles represent vertical dip angles (75-105°) and red circles represent west-dipping craton rmargins (>105°).

4.5 The Effects of Mantle Wind

In the modelling experiments described above, there is no relative motion between the continental mantle lithosphere and the underlying sub-lithospheric mantle. In those experiments only a narrow range of tested strength increases and density reductions preserve vertical craton margins or produce west-dipping craton margins, for all other tested values the craton margin is gradually eroded to an eastward dip. Therefore, the effects of large scale mantle flow and/or

relative plate motion (referred to here as mantle wind) on the evolution of the craton margin are also considered. The numerical models are solved in a continental reference frame; thus mantle wind is incorporated into the models by imposing a velocity boundary condition on the sub-lithospheric mantle.

As discussed in Section 2.4.3, observed seismic anisotropy provides evidence for mantle flow. Studies of azimuthal anisotropy in the mantle below North America indicate a change in mantle flow patterns across the Cordillera-craton transition, coinciding approximately with the Rocky Mountain Front [*Yuan and Romanowicz*, 2010a, 2010b; *Yuan et al.*, 2011]. Below the Cordillera, strong azimuthal anisotropy is observed at depths of ~70-100 km, and is aligned with the absolute plate motion of the North American plate (i.e. NE-SW); however, in the ~100-150 km depth range the fast axis becomes approximately aligned with the absolute motion of the Pacific plate [*Yuan and Romanowicz*, 2010a; *Yuan et al.*, 2011]. In the craton, weak azimuthal anisotropy is observed at depth shallower than ~200 km, but becomes strong at ~250 km (approximately corresponding to the lithosphere-asthenosphere boundary) and is also aligned with absolute plate motion on the North American plate [*Yuan and Romanowicz*, 2010b; *Yuan et al.*, 2011]. Unfortunately, seismic anisotropy can only delineate the trend in mantle flow, not the direction of flow (i.e. NE to SW or SW to NE directed flow). Several authors have used models that combine GPS data, seismic anisotropy, and geodynamic models of mantle convection, and provide estimated present-day mantle flow velocities of ~0.2-5.5 cm/yr below North America, but there is no consensus on the direction of flow [*Silver and Holt*, 2002; *Conrad et al.*, 2004; *Eaton and Frederiksen*, 2007]. Thus numerical modelling experiments for this study test a range of mantle wind velocities in both west-to-east and east-to-west directions.

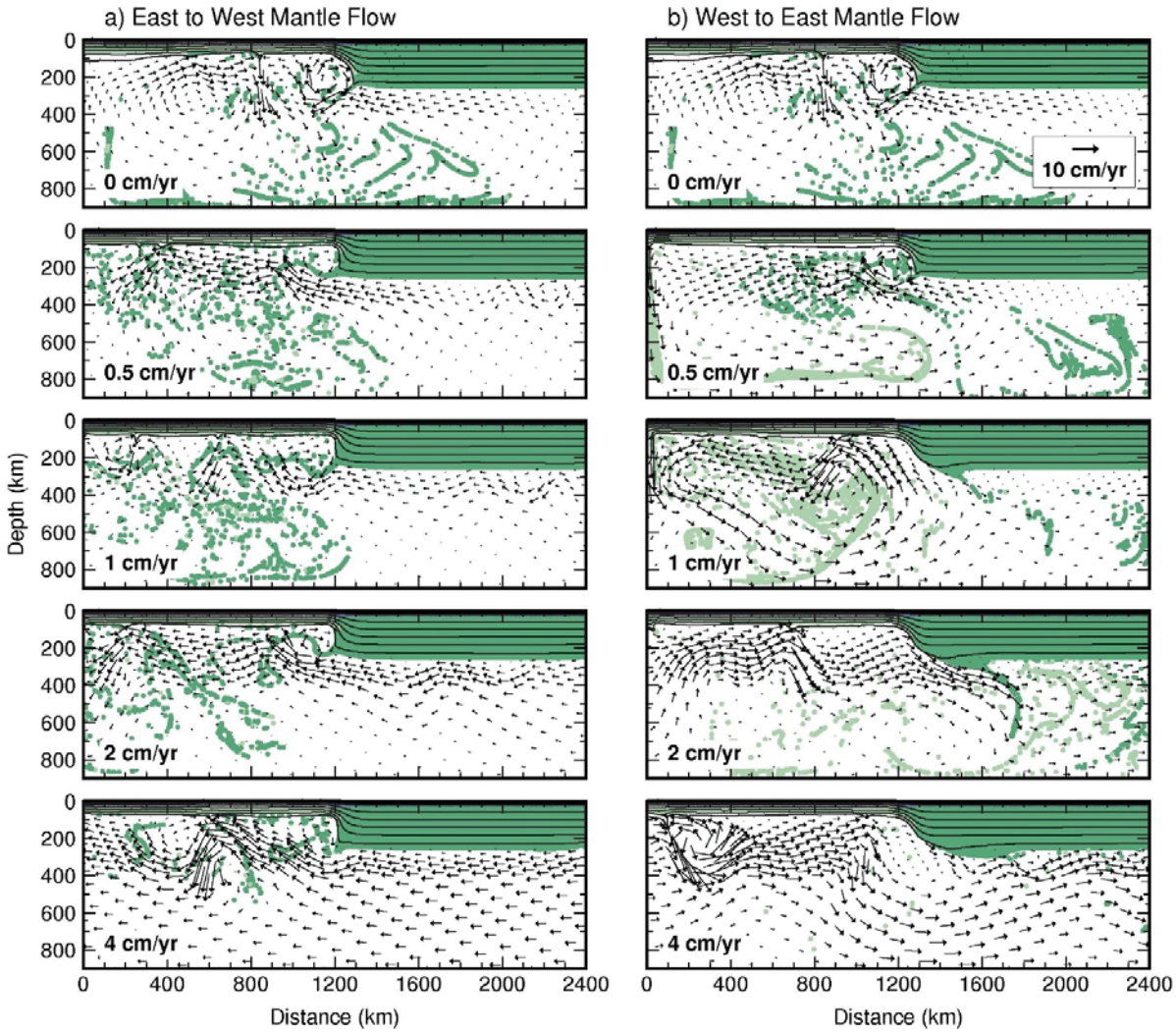

Figure 4.8: The influence of the range of tested mantle flow velocities on the geometry of the craton margin after 100 Ma of model evolution. Mantle wind velocities are shown for both a) an east to west directed flow, and b) a west to east directed flow. The craton mantle lithosphere is 5 times stronger and 20 kg/m^3 less dense than the reference model. Imposed velocity boundary conditions are shown in the lower left-hand corner of each model, and all models use the same velocity scale, indicated by the 10 cm/yr velocity vector shown in the white box in the top right-hand corner of the 0 cm/yr model plot in b).

Mantle wind velocities of 0.5 cm/yr, 1 cm/yr, 2 cm/yr and 4 cm/yr are tested on all density and strength combinations presented in sections 4.3 and 4.4, and flow is tested in both the east-west and west-east directions (i.e. right to left and left to right through the model domain, respectively) for a total of 288 experiments. Figure 4.8 shows the results for mantle lithosphere that is 5 times stronger and 20 kg/m^3 less dense than the reference model after 100

Ma of model evolution. In the absence of mantle flow (i.e. a mantle wind of 0 cm/yr), this particular combination of density and strength produces a shallowly dipping (<45°) craton margin (Figure 4.7 and top row of Figure 4.8). The deformation and removal of the craton lithosphere results in gravitational instability. The addition of horizontal mantle flow shears the base of the craton mantle lithosphere and alters the style of the removal process. In general, mantle wind slows the descent of removed craton mantle lithosphere material through the sub-lithospheric mantle; however, this effect is highly sensitive to direction and, to a lesser degree, speed of the imposed flow.

When mantle wind is directed east-to-west (or right to left through the model domain), removed mantle lithosphere material is pushed westward as it drips away from the craton (Figure 4.8a). In addition, the clockwise convection cell at the edge of the craton margin is intensified, as the flow of mantle material is drawn into this region by a lower pressure gradient. If mantle flow is less than 2 cm/yr, this westward push and clockwise convection cell help prevent erosion of the craton margin and its initially vertical geometry is maintained. At velocities of 2 cm/yr, mantle wind is too slow to induce significant shearing on the lithosphere. The gravitational effects (i.e. the high thermal density of the cratonic mantle lithosphere) dominate dynamics, and material sinks into the sub-lithospheric mantle as in the case without mantle wind. This prevents the development of a west-dipping craton margin. Conversely, a mantle wind velocity of 4 cm/yr is much larger than the velocities associated with convective flow. In this case, the destabilizing lithosphere is sheared and any mantle lithosphere that dips away from the bottom of the craton is carried sideways as it descends. This prevents it from sinking to depths greater than ~600 km, and overall, the margin maintains a near vertical geometry such that no westward dip is observed. For the model shown in Figure 4.8a, a velocity of 2 cm/yr is the only mantle wind

velocity that successfully produces a west-dipping craton margin. In this case, corner flow at the lithosphere step is balanced by the westward push of the mantle wind; mantle flow is fast enough to entrain the downwelling cold lithospheric material, but not so fast that the material is immediately removed from the craton margin. Thus, the drip is carried away sideways below the Cordillera, and the geometry of the craton margin evolves to a westward dip (~105-110°).

The effects of mantle wind that flows from west-to-east (or from left to right through the model domain) are shown in Figure 4.8b. Contrary to the westward flow discussed above, eastward mantle wind generally enhances erosion of the craton margin for the range of tested velocities. This is because the edge of the lithosphere step is entirely exposed to erosion from both convective and mantle wind flow velocities. In contrast, when flow is in the opposite direction the step is protected from mantle wind. Furthermore, material that is eroded from the edge of the lithosphere step is re-deposited along the base of the craton lithosphere as it is transported eastward, resulting in locally thickened craton mantle lithosphere. When a velocity of 0.5 cm/yr is imposed on the model, upward flow of material resulting from convection at the lithosphere step is counteracted by the eastward flowing mantle wind, and thus the craton margin maintains a vertical geometry. All other mantle wind velocities tested result in craton margin that dips shallowly eastward (<45°) for the combination of density and strength shown in Figure 4.8b.

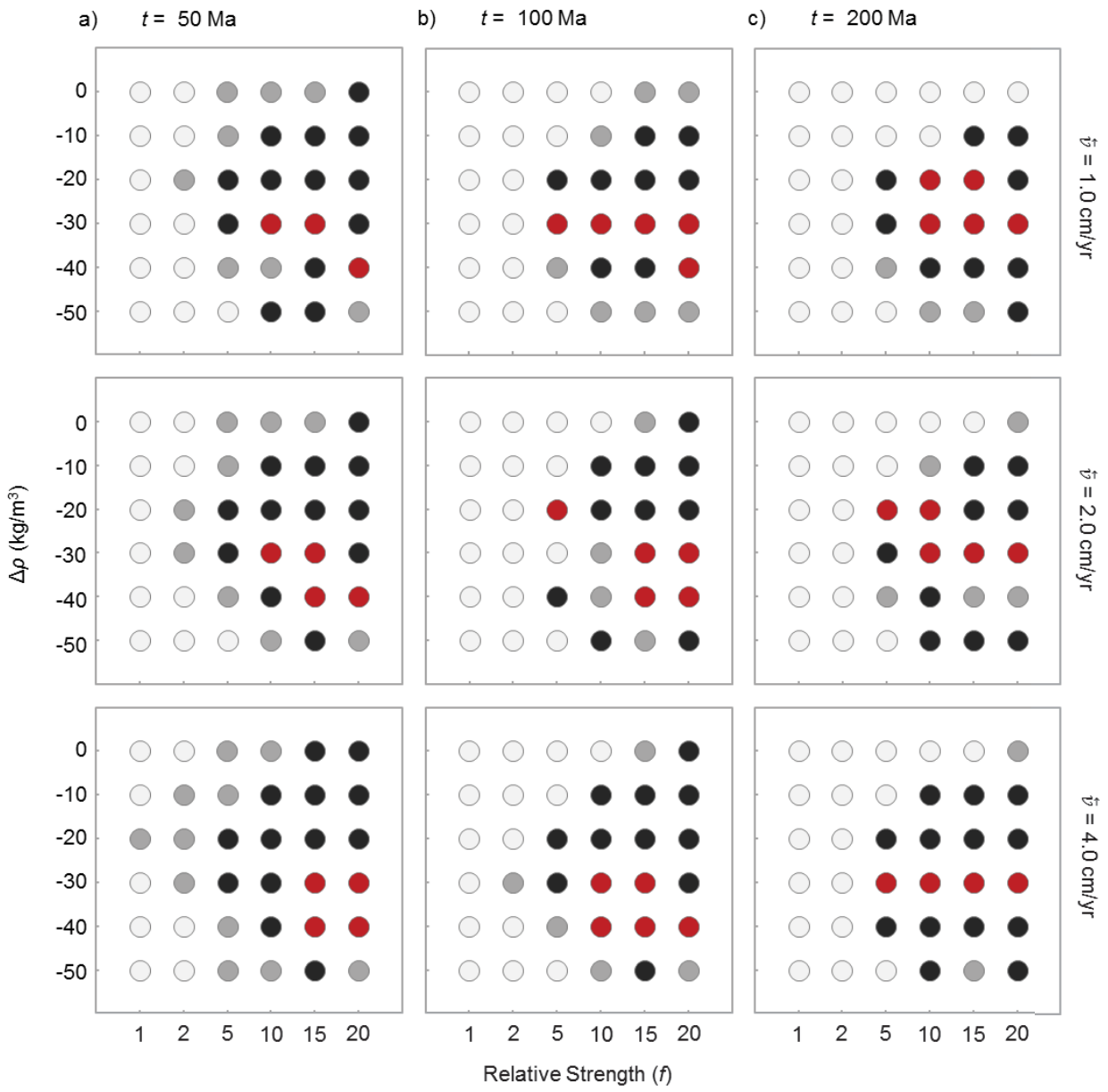

Figure 4.9: Diagrams summarizing and comparing the evolution of craton margin geometry in numerical modelling experiments for three tested velocities of mantle wind flowing in an east to west direction. a) Evolution of the models after 50 Ma for mantle wind velocities of 1 cm/yr (top), 2 cm/yr (middle) and 4 cm/yr (bottom); b) same as in a) but at 100 Ma of model evolution; c) same as in a) and b) but at 200 Ma of model evolution. Circles represent tested combinations of increased strength (i.e. viscosity scaling factor (*f*) of Equation 3.11) and decreased density, relative to the reference values. Colours represent the dip angle of the craton margin; light grey = shallow dip (<45°), grey = steep dip (45-75°), black = vertical (75-105°) and red = west-dipping craton margins (>105°).

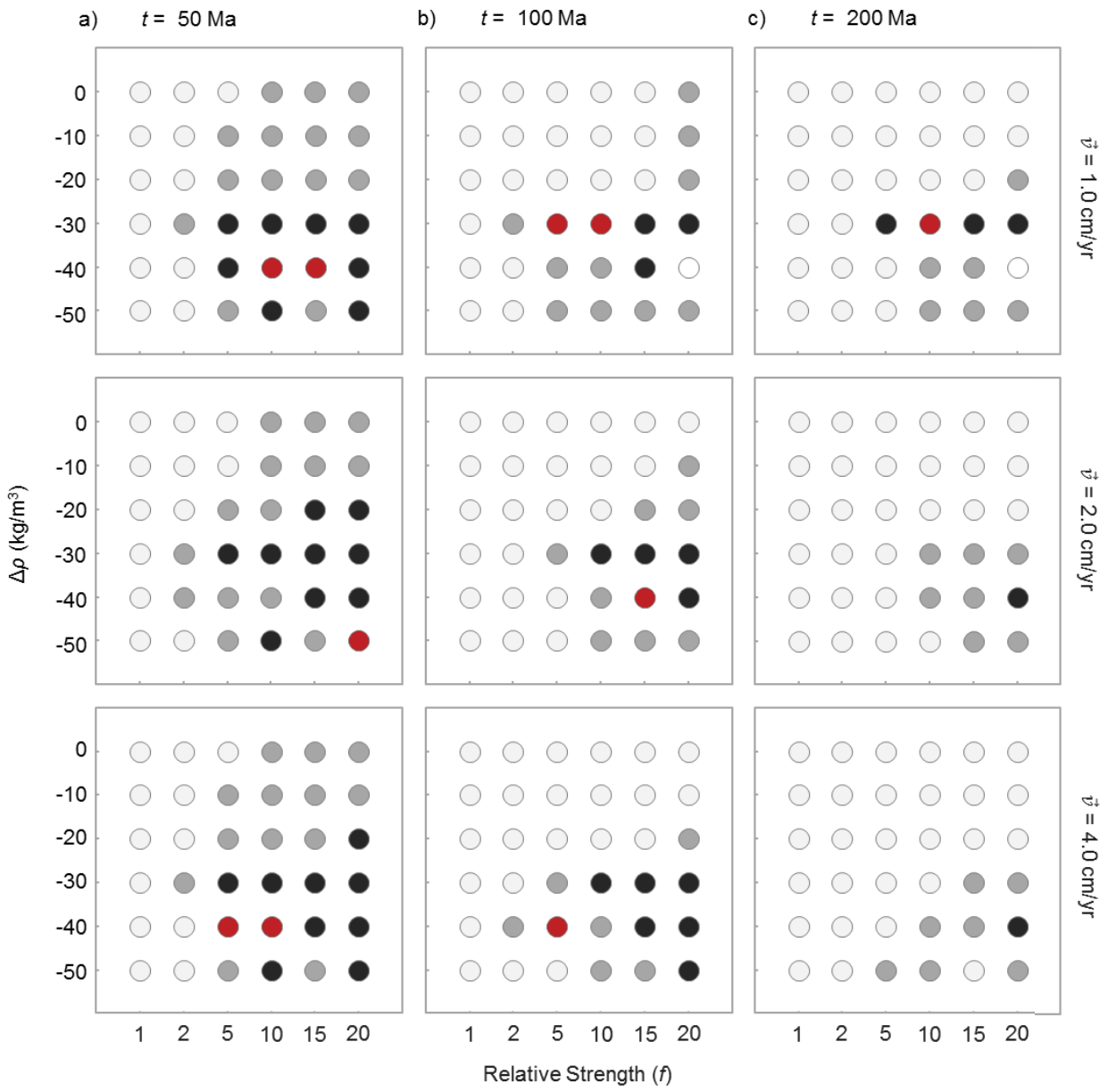

Figure 4.10: Diagrams summarizing and comparing the evolution of craton margin geometry in numerical modelling experiments for three tested velocities of mantle wind flowing in a west-east direction. a) Evolution of the models after 50 Ma for mantle wind velocities of 1 cm/yr (top), 2 cm/yr (middle) and 4 cm/yr (bottom); b) same as in a) but at 100 Ma of model evolution; c) same as in a) and b) but at 200 Ma of model evolution. Circles represent tested combinations of increased strength (i.e. viscosity scaling factor (*f*) of Equation 3.11) and decreased density, relative to the reference values. Colours represent the dip angle of the craton margin; light grey = shallow dip (<45°), grey = steep dip (45-75°), black = vertical (75-105°) and red = west-dipping craton margins (>105°).

A summary of modelling results for all mantle wind experiments are shown in Figures 4.9 and 4.10 for eastward and westward directed mantle flow, respectively. Overall, the modelling experiments indicate that under the influence of mantle wind, the geometry of the

craton margin is strongly dependent on the direction of flow. A comparison of Figures 4.7 and 4.9 show that east-west flowing mantle wind increases the range of density and strength values that produce west-dipping and vertical craton margin geometries. Without mantle wind, only models in which the craton mantle lithosphere is 5-15 times stronger and 30-40 kg/m^3 less than the reference value facilitate the formation of a westward dipping craton margin, and vertical margins are only observed for mantle lithosphere 2-20 times stronger and 10-50 kg/m^3 less dense than the reference value (Figure 4.7). However, for an imposed east-west mantle wind, vertical craton margins are observed over the whole range of tested densities and at strengths a factor of 5 or greater than the reference value (Figure 4.9). In addition, west dipping craton margins are observed for mantle lithosphere that is 20-40 kg/m^3 less dense and 5-20 times stronger than the reference values. An east-west flowing mantle wind also preserves vertical and west-dipping craton margins over longer periods of geologic time.

Conversely, a comparison of Figures 4.7 and 4.10 shows that a west-east mantle wind greatly impedes the formation of both west-dipping and vertical craton margin geometries, for the range of tested strength and density values. Only models in which the craton mantle lithosphere is 30-50 kg/m^3 less dense and 5-15 times stronger than the reference values produce a west-dipping craton margin (Figure 4.10). Vertical craton margins are also observed over a narrower range of density and strength values (mantle lithosphere 5-15 times stronger and between 20-50 kg/m^3 less than the reference value) compared to models without imposed mantle wind. Furthermore, vertical and west-dipping geometries are maintained over shorter periods of time, and their persistence decreases with increasing mantle wind velocity (Figure 4.10c); when the velocity is greater than 1 cm/yr none of the models produce a craton margin with dip greater than 75° after 100 Ma of model evolution.

4.6 Effects of Crustal Shortening

The experiments described above focus on erosion of a craton margin due to gravitational effects (Sections 4.2 to 4.5) and shearing by mantle wind (Section4.5) for a range of craton mantle lithosphere densities and strengths. A third hypothesis is tested here. A west-dipping craton margin may arise from crustal shortening, where far-field tectonic forces induce thrusting of the Cordillera crust over the Craton. As a result, the upper craton margin may move eastward relative to the deeper margin, resulting in a westward dip.

In western Canada, geological and geophysical data show that during Cordillera deformation, the Foreland Belt (Figure 2.2) behaved as a thin-skinned fold and thrust belt; it is inferred to have accommodated ~150-200 km of shortening between approximately 100 and 50 Ma, from the Late Cretaceous until the Early Eocene [*McClelland and Oldow*, 2004; *Evenchick*, 2007; *Simony and Carr*, 2011]. The goal of the experiments described below is not to directly simulate convergent tectonic events within western Canada but to test the influence of crustal shortening on the geometry of the craton margin. However, parameters are chosen to be reasonable with respect to the Late Cretaceous-Early Eocene shortening events. A constant shortening rate of 0.4 cm/yr is used everywhere, and the numerical models are run for 50 Ma, for a total of 200 km of shortening. Equal convergence rates are imposed on the left and right hand side of the model; thus a 0.2 cm/yr velocity boundary condition is applied to each side of the model domain.

A series of model experiments incorporating crustal shortening are conducted to determine if plate convergence and crustal shortening can produce or enhance west-ward dipping geometry of the craton margin. All of the models presented in this section are preliminary, and thus the reference density (Table 3.1) is assigned to the mantle lithosphere everywhere, such that

no change in compositional density occurs at the step in the lithosphere; however, the strength of the mantle lithosphere and upper crust are varied in both the Cordillera and craton.

Figure 4.11 shows the results at 50 Ma for the reference strength (Table 3.1) and mantle lithosphere that is 50 and 100 times stronger, and is applied to the mantle lithosphere of both the craton and Cordillera. Strength values this large are not realistic, but are used here to counteract gravitational instability of the mantle lithosphere and to concentrate deformation at the Cordillera-craton boundary. As in the experiments discussed above (Figure 4.5), when the lithosphere of both the Cordillera and the craton are assigned the reference strength, the craton margin is quickly eroded. Downwelling of Cordillera mantle lithosphere occurs at distances >300 km away from the craton margin, as thickening in the crust is compensated by thinning of the mantle lithosphere which prevents a significant increase in total lithosphere thickness. Because it is cold, the lithosphere of the craton is much stronger than the Cordillera, and the imposed velocities result in deformation throughout the weaker Cordillera, rather than localizing at the Cordillera-craton boundary. As a result, the boundary between the two migrates westward by ~100 km over 50 Ma of model evolution and there is little crustal thickening in the craton.

In an attempt to prevent Cordillera deformation and localize deformation at the boundary, the strength of the mantle lithosphere is increased in both the craton and Cordillera (Figure 4.11). For mantle lithosphere strength increases by factors of 50 and 100, a dramatic decrease in lithosphere removal is observed in both the craton and Cordillera. Increased mantle lithosphere viscosity allows the craton margin to maintain a vertical geometry and the stronger Cordillera lithosphere allows it to thicken over the 50 Ma model time. However, if the models were allowed to evolve over a longer period of time, it is likely that the high temperatures in the Cordillera would still result in thinning of the lithosphere. Furthermore, the boundary between the two

lithospheric blocks still migrates ~100 km westward, despite increased strength in the lithosphere.

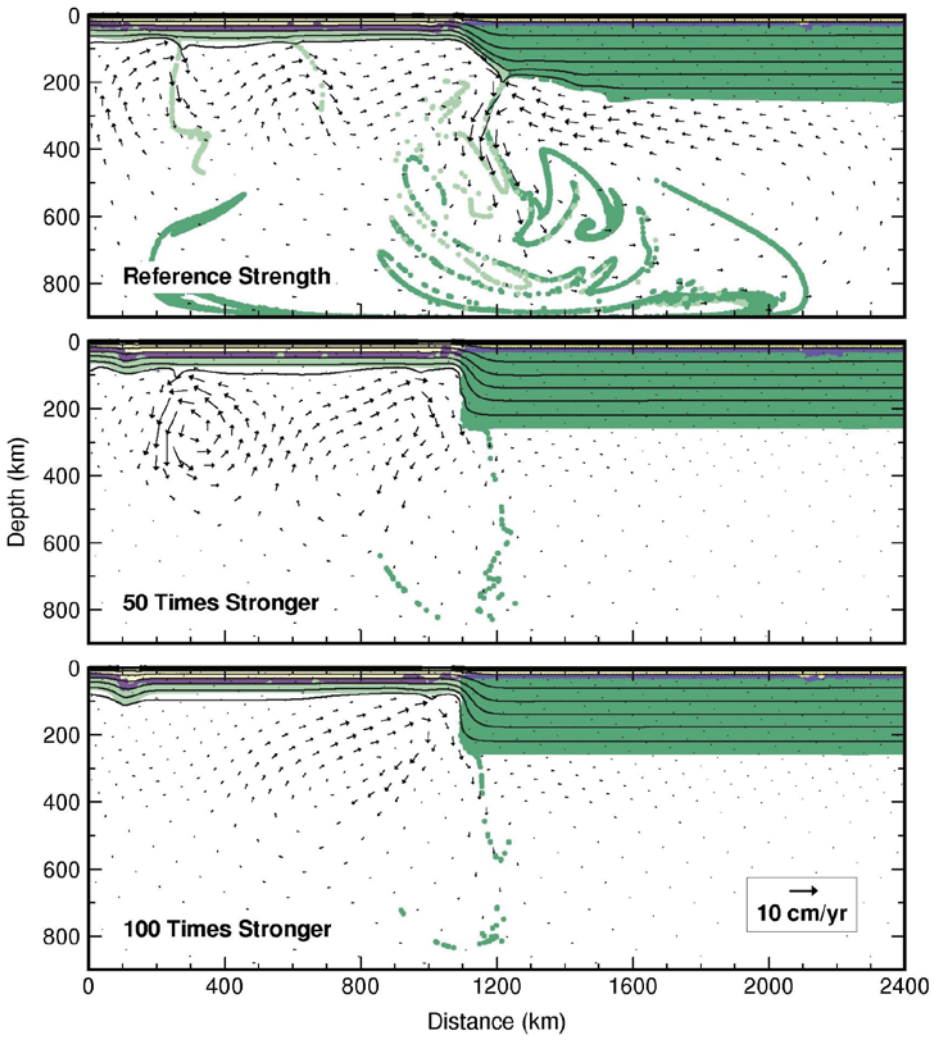

Figure 4.11: The results of crustal shortening models at 50 Ma in which the strength of the mantle lithosphere in both the craton and Cordillera are increased by factors of 50 (middle) and 100 (bottom) relative to the reference strength (top). Note that the scale for velocity vectors is shown in the white box at bottom right-hand corner of the bottom plot.

None of these convergence experiments successfully produces a westward dipping craton margin, and over-thrusting of the Cordillera crust is not achieved. Even for an extremely strong Cordillera lithosphere, deformation is not localized at the Cordillera-craton boundary. Thus a weak seed is introduced to determine if the addition of a zone of weakness will concentrate

deformation at the boundary. Tables 4.1 and 4.2 list the tested variety of weak seed geometries. All weak seeds are placed within the hot Cordillera lithosphere, adjacent to the Cordillera-craton boundary. The wet olivine rheology of *Hirth and Kohlstedt* [2003] (Table 3.1) is assigned to the weak seed; however, the viscosity scaling factor (Equation 3.11) is reduced to 0.1 and the internal friction angle (Equation 3.9, Table 3.1) is reduced to 2° to remove strain softening and promote the concentration of deformation within the weak seed. The rheological parameters used here are similar to those that have been applied to numerical modelling experiments with lithosphere extension [*Huismans and Beaumont*, 2003; *Beaumont and Ings*, 2012].

Table 4.1: Non-dipping weak seed geometries used for crustal shortening experiments. Dimension values are for width and height respectively; depths reported are for depth to the top of the weak seed. All weak seeds are placed within the Cordillera lithosphere, such that the easternmost side is located at x = 1200 km. Mantle lithosphere scaling factors divided with a "/" denote tests for strength values in the Cordillera and craton, respectively (e.g. 50/40 indicates a strength of 50 in the Cordillera mantle lithosphere and 40 in the craton). ML = Mantle Lithosphere; LC = Lower Crust; UC = Upper Crust, WO*0.1= Wet Olivine (i.e. the reference damp olivine with a viscosity scaling factor of f = 0.1). For details on materials, see Table 3.1 in Section 3.4.

Dimensions (km)	**Depth (km)**	**Material**	**Location**	**Scaling Factor f (Mantle Lithosphere)**
Square Geometries				
10 × 10	37.5	WO* 0.1	ML	1, 50, 50/40, 50/20, 100, 100/80, 100/50
10 ×10*	25	WO*0.1 WQ	LC/ML	1, 25, 50, 100 25
20 × 20	37.5	WO*0.1	ML	1, 25, 50, 100
50 × 50	10	WO*0.1	UC/LC/ML	1, 25, 50, 100

Rectangular Geometries				
10 × 20	37.5	WO*0.1	ML	1, 50, 100
10 ×20	25	WO*0.1	LC/ML	1, 50, 100
30 × 50	10	WO*0.1	UC/LC/ML	1, 25, 50, 100

As with the convergence experiments discussed above, models with both the reference rheology for the craton and Cordillera mantle lithosphere and models with increased strength mantle lithosphere strength are tested for all weak seed geometries. None of the square or rectangular weak seed geometries (Table 4.1) effectively concentrate deformation at the boundary between the Cordillera and craton or produce a westward dipping craton margin, regardless of the tested viscosity scaling factor. Weak seeds geometries with dips of 45° toward the west (Table 4.2) are also tested to act as "ramps" to help initiate thrusting of the Cordillera crust over the craton. However, neither over-thrusting nor west-dipping craton margin geometries are observed for the range of viscosity scaling factors and geometric variations tested.

Table 4.2: Dipping weak seed geometries used in crustal shortening experiments, note that all weak seeds dip westward (i.e. toward the Cordillera). Dimension values for parallelograms are given for width and length, respectively; depths are reported with respect to the shallowest portion of the weak seed. All weak seeds are placed within the Cordillera lithosphere and lie adjacent to the Cordillera-craton boundary at x = 1200km.

Shape	**Dimensions (km)**	**Dip Angle (°)**	**Depth (km)**	**Material**	**Scaling Factor *f*** (Mantle Lithosphere)
Dipping Geometries					
Parallelogram	10 × 14	45	37.5	WO*0.1	1, 50, 100

Parallelogram	10 × 28	45	37.5	WO*0.1	1, 25, 50, 50/20, 50/40, 100, 100/50, 100/80
Trapezoid	30 × 71 × 42	45	10	WO*0.1	1, 25, 50, 100
Composite Geometry[*]					
Parallelogram (ramp)	20 × 56	26	0	WO*0.1	25
Square (base)	10 × 10	-	25		25

In all the above models, the Cordillera and craton strength are varied by the same amount. A few weak seed geometries are selected to test the effects for varying the craton mantle lithosphere strength relative to the Cordillera mantle lithosphere. Because of its high geothermal gradient, the strength of the Cordillera mantle lithosphere is increased relative to the craton (strength values separated by a "/" in Tables 4.1 and 4.2) as an attempt to offset the thermally-induced relative strength contrast between the Cordillera and craton. However, these experiments are also unsuccessful in creating a west-dipping craton margin and over-thrusting of the Cordillera crust. The main issue appears to be that the Cordillera persists as a region of weakness, and therefore shortening causes deformation here, rather than at the Cordillera-craton boundary.

Owing to the high temperatures and small mantle lithosphere thickness, the main strength of the Cordillera lithosphere resides within its crust. Therefore, the square weak seed marked with an asterisk in Table 4.1 is selected for further experimentation, to determine if increased crustal strength helps initiate over-thrusting during imposed shortening. For these experiments, a

mantle lithosphere rheology 25 times stronger than the reference value is used for both the Cordillera and craton. This value is chosen because previous experiments indicate a trade-off between material strong enough to resist gravitational erosion of the craton margin and material weak enough to sufficiently deform over the modelled 50 Ma time frame. The upper crust of both the Cordillera and the craton are initially assigned a viscosity scaling factor of 25, which is 20 times stronger than the reference value (Table 3.1). However, because the craton crust is cold compared to the Cordillera, the Cordillera remains a zone of weakness and over-thrusting is not achieved. Thus the upper crust of the craton is assigned the reference strength while the upper crustal of the Cordillera is 25 and 50 times stronger than the reference value. The effects of a wet quartzite weak seed rheology (Table 3.1, with a scaling factor of $f = 1$) is also investigated. Wet quartzite is weaker than olivine, and therefore this rheology could enhance the effect of the weak seed. Unfortunately, neither of these models concentrate deformation at the Cordillera-craton boundary, which suggests the weak seed may not be large enough. The geometry of the weak seed is subsequently modified to include a "ramp" that extends to the Earth's surface, as outlined by the composite weak seed geometry given in Table 4.2. The ramp is a shallowly dipping (30°) weak zone that dips westward, toward the Cordillera.

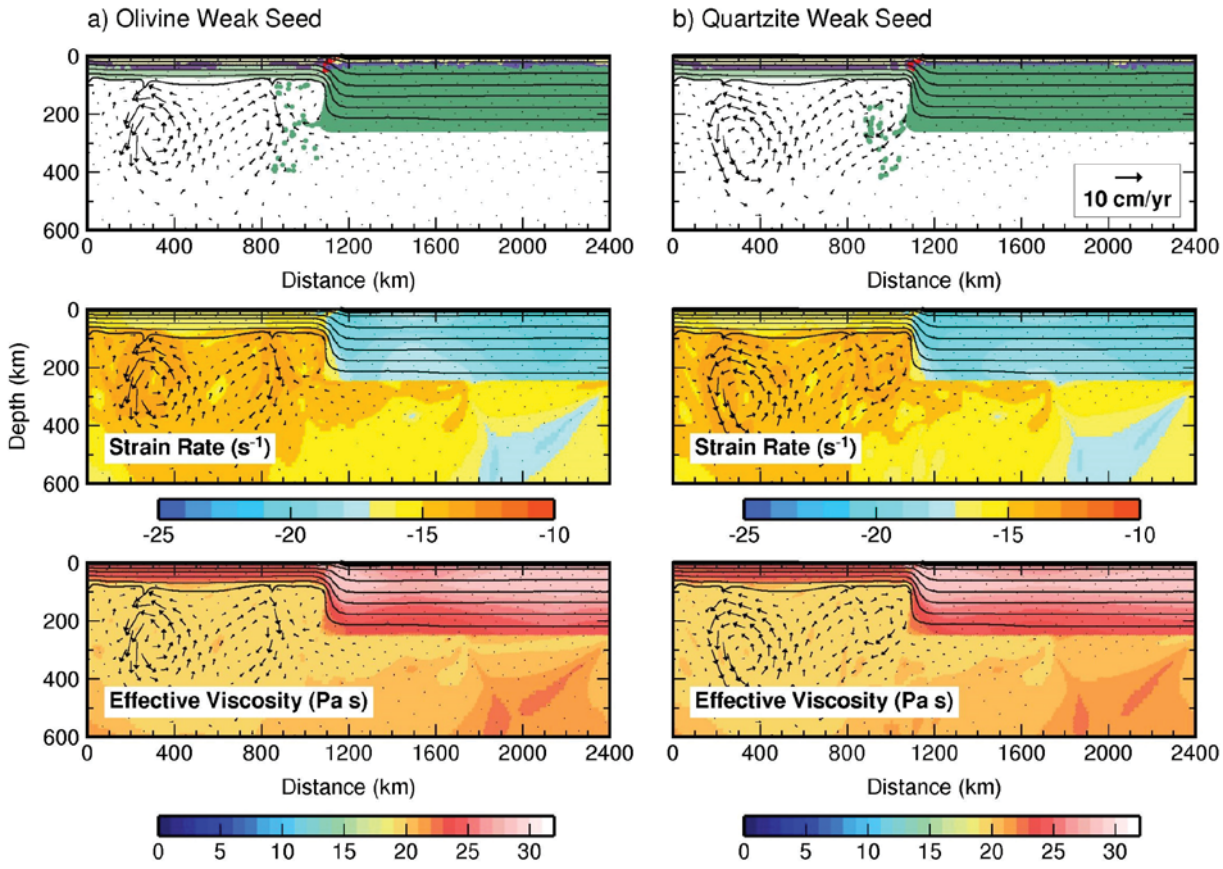

Figure 4.12: Results of convergence models for a composite geometry weak seed (Table 4.2) with a) a wet olivine rheology, and b) with a wet quartzite rheology. The upper plot shows the model result, the center plot shows the magnitude of the maximum shear strain (logarithmic scale), and the bottom plot shows the magnitude of the effective viscosity (logarithmic scale). The upper crust of the craton is assigned the reference value, whereas the upper crust of the Cordillera is 50 times stronger than the reference value. The mantle lithosphere in both the craton and Cordillera are 25 times stronger than the reference value.

Figure 4.12 shows the model results with the composite weak seed geometry for a wet olivine weak seed rheology and a wet quartzite rheology after 50 Ma of model time. The addition of a shallow ramp successfully concentrates strain at the Cordillera-craton boundary, as shown by the region of high strain rate in Figure 4.12 (second row). It appears the presence of a weak zone within the crust is necessary for shortening to localize deformation; in previous models, a simple change in crustal strength is not sufficient. By 50 Ma and 200 km of shortening, a west-dipping craton margin is produced for both weak seed rheologies, although the dip does not exceed ~110° in either model. However, the weaker quartzite seed better concentrates strain at

the craton edge and facilitates thrusting of ~60 km of Cordillera crust onto the craton. For the olivine weak seed rheology, only ~50 km of over-thrusting is observed. The Cordillera mantle lithosphere is uniformly thickened by ~10 km in both models, and the Cordillera-craton boundary remains vertical down to the base of the Cordillera lithosphere; at depths below this, the craton margin has a westward dip. However, in the model with a quartzite weak seed, there is little deformation elsewhere in the crust of both the Cordillera and craton relative to the weak seed with a wet olivine rheology at distances >200 km from the craton-Cordillera boundary.

Overall, the results of the crustal shortening experiments discussed here suggest that a west-dipping craton margin and over-thrusting of the Cordillera crust can not be created via crustal shortening without the addition of a substantial zone of weakness. Without a weak zone, deformation is largely concentrated in the lithosphere of the Cordillera due to high temperatures, which weaken the material significantly. The weak seed used here is a modelling parameter to test the effect of heterogeneities in the lithosphere. In nature, the weak zone may correspond to sedimentary rocks of either the continental passive margin or accreted terranes, or a mid to lower crustal décollement, associated with the long tectonic history of the lithosphere of western Canada [*McClelland and Oldow*, 2004; *Simony and Carr*, 2011]. Because west-dipping and vertical craton margin geometries are presently observed in seismic images from the Canadian Cordillera (Figure 1.2), further experimentation is required to determine the post-shortening stability and evolution of this craton margin geometry over time scales greater than 50 Ma, which corresponding to the cessation of shortening in the Canadian Cordillera ~59-52 Ma [*Simony and Carr*, 2011].

4.7 Summary

This work is motivated by complex structures observed in seismic studies of the Canadian Cordillera. The goal of the modelling experiments presented in this chapter is to explore the evolution of craton margin geometry over long (>100 Ma) periods of geologic time to determine whether various dynamic processes create, enhance or destroy vertical and west-dipping craton margin geometries. Initially, the strength and compositional density of the craton mantle lithosphere are varied to investigate the effects of mantle convection and edge-driven flow. Subsequent experiments test the influence of large scale mantle flow (or mantle wind) that is varied in both direction and speed, and finally, the effects of crustal shortening are also explored. Models that test convection and east-west flowing mantle wind of 2 cm/yr of less are more successful in producing vertical and west-dipping craton margin geometries than crustal shortening models. Ultimately, experiments in which the craton mantle lithosphere is both buoyant and strong are most successful. In particular, craton mantle lithosphere that is 30 kg/m^3 less dense and 10-15 times stronger than the reference values produce and best maintain both vertical and westward dipping craton margins with dip angles of approximately 105-120°, consistent with the observations described in Section 1.1 (Figure 1.2).

Chapter 5: Discussion

The objective of this study is to investigate the dynamics of the margin of thick cratonic mantle lithosphere. It was motivated by observational seismic data from western Canada, which shows that the transition from thin (~60 km) Cordillera lithosphere to thick (~250 km) craton lithosphere occurs over a lateral distance of less than 100 km [e.g., *Bao et al.*, 2014a], suggesting a sub-vertical step in lithosphere thickness. Recent high-resolution seismic data shows that in southwestern Canada the craton margin may dip westward (i.e. toward the Cordillera) [*Chen et al.*, submitted manuscript 2016] (Figure 1.2). Thus, a specific goal of this work is to determine whether a west-dipping craton margin geometry can be produced via geodynamic processes and whether such a feature can persist over timescales >100 Ma. The modelling experiments presented in Chapter 4 successfully produce west-dipping and vertical craton margin geometries, but only for craton mantle lithosphere that is both buoyant and viscous relative to the surrounding sub-lithospheric mantle. This suggests that dehydration and chemical depletion of craton mantle lithosphere play key roles in preventing erosion of the craton margin, and consequently determine the geometrical evolution of the craton margin.

Processes such as partial melting deplete the mantle lithosphere of REE's (Rare Earth Elements) and lower its Mg# (Mg/ (Mg+Fe) × 100; a geochemical indicator of olivine depletion; a higher Mg# indicates greater depletion) [*Salters and Stracke*, 2004]. This chemical alteration results in a reduced mantle lithosphere density. Geochemical analysis of mantle xenoliths typically report Mg# numbers of ~90-92, with the degree of depletion increasing with lithosphere age [*Bernstein et al.*, 2007; *Karato*, 2010]. Subsequently, the change in compositional density relative to a primitive mantle (Mg# of ~88) composition is estimated to be ~0.7-2.5% for

cratonic mantle lithosphere [*Poudjom Djomani et al.*, 2001], like the Archean- to Proterozoic-aged North American craton. Lowering the density of the craton mantle lithosphere counteracts the effects of thermal contraction, which results from cold temperatures in the craton mantle lithosphere relative to the surrounding mantle. Therefore, depletion contributes to the preservation of the craton margin by reducing gravitational instability in the craton mantle lithosphere.

Geodynamic studies that focus on the preservation of thick craton lithosphere demonstrate that a low density is a necessary requirement to prevent basal erosion of the lithosphere and maintain thick (>200km) lithosphere roots [*Shapiro et al.*, 1999; *Lenardic*, 2003; *Wang et al.*, 2014]. However, these studies primarily focus on the central regions of continental plates. The current study focuses specifically on the margin of the craton. A key result from this study is that there appears to be an upper bound on the degree of mantle lithosphere depletion for the formation of a westward-dipping craton margin geometry, as is observed in western Canada. Figure 5.1 compares the evolution of the craton margin geometry under the influence of convection alone, and shows that over time scales of 50 Ma or more, west-dipping craton margins are exclusively observed when the mantle lithosphere is 30-40 kg/m^3 (or 0.9-1.2%) less dense than the surrounding sub-lithospheric mantle. Xenoliths from below Alberta show compositional layering of the cratonic mantle lithosphere with depth; less depleted above ~115 km depth, highly depleted from 115 to 150 km, and melt/metasomatized re-fertilized below 160km [*Griffin et al.*, 2004]. Therefore, the mid-range degree of depletion that successfully produces west-dipping and vertical craton margin geometries in the models appears to be consistent with regional mantle lithosphere composition.

Figure 5.1 also shows that, although buoyancy is critical, strength of the craton mantle lithosphere appears to be more important for creating and preserving vertical and west-dipping craton margin geometries. Partial melting also results in dehydration of the mantle lithosphere, as water is incompatible and will preferentially partition into the melt phase [*Karato*, 2010]. There is an approximately linear relationship between increasing Mg# and decreasing water content [*Karato*, 2010]. As explained in Section 4.3, lowering the water content of olivine greatly increases its strength; laboratory experiments suggest that the difference in effective viscosity of olivine between water saturation and completely dry conditions can be as large as 4 orders of magnitude at constant stress [*Hirth and Kohlstedt*, 2003; *Karato*, 2010]. In this study, the models that most successfully result in westward dipping craton margins are those with viscosity scaling factors greater than 5, relative to the surrounding mantle. These values correspond to olivine compositions that range from dry to a water content of ~10 ppm H/10^6Si (Figure 4.3), and are consistent with estimates of water content for craton mantle lithosphere from laboratory experiments and long-period magnetotelluric conductivity studies [*Hirth et al.*, 2000; *Hirth and Kohlstedt*, 2003; *Karato*, 2010]. Thus, it can be concluded that the viscosity contrast between the craton and surrounding mantle required for vertical and west-dipping craton margin geometries in the models is not unreasonable with respect to estimates from the literature. In addition, geodynamic models that focus on lithosphere evolution in continental interiors show that the preservation of thick craton lithosphere requires both a high viscosity and low density [*Lenardic*, 2003; *Wang et al.*, 2014], consistent with the conclusions of the current study on the craton margins.

The results of this study have shown that west-dipping craton margin geometries can persist over time scales of 50 Ma or more; however, in many of the models, west dipping geometries

develop and are eroded over shorter time scales, on the order of tens of millions of years (Figure 5.1). In some cases, the craton margin assumes a westward dip more than once throughout the 200 Ma evolution of the model. This suggests that a west-dipping craton margin may be both a long-lived and transient feature, and in some instances, perhaps a recurring transient feature.

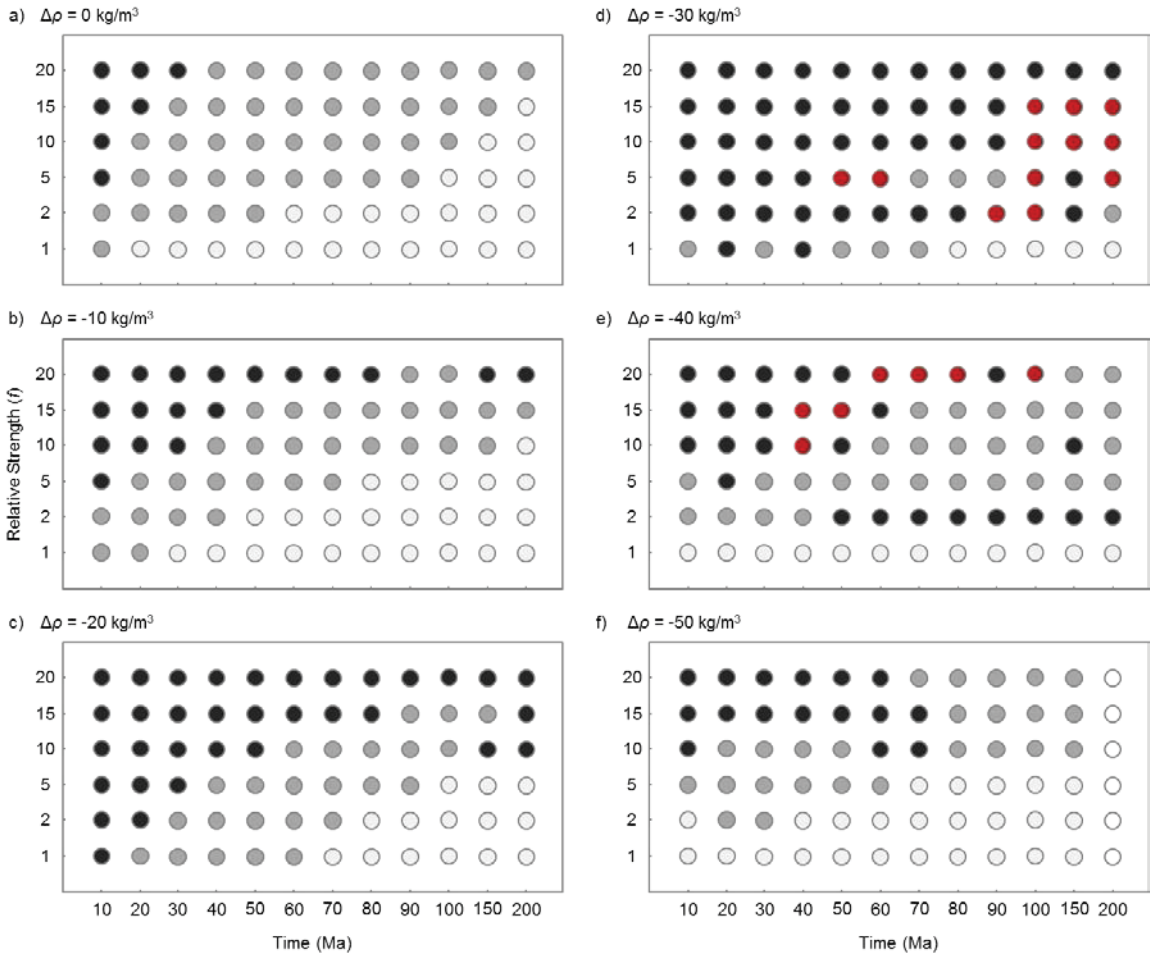

Figure 5.1: Diagrams summarizing the influence of relative density and strength of cratonic mantle lithosphere on the evolution of craton margin geometry through time. Models with different viscosity scaling factors (Equation 3.11) are plotted versus time for each density reduction, relative to the reference density. Circles represent measured craton angles at each time step and colours are used to represent the dip of the craton margin; light grey = shallow dip (<45°), grey = steep dip (45-75°), black = vertical dip (75-105°), and red = westward dip (>105°).

An example of a recurring, transient west-dipping craton margin is shown in Figure 5.2 for a model under the influence of thermally-driven convection. In this model the mantle lithosphere is 30 kg/m^3 less dense and 5 times stronger than the reference values. At 40 Ma the

craton edge remains vertical, but the reduced compositional density of the craton mantle lithosphere results in the initiation of upwelling of the craton edge. By 60 Ma some of the material has detached from the craton edge and is deposited along the base of the Cordillera mantle lithosphere, adjacent to the Cordillera-craton boundary. However, smaller masses of cratonic mantle lithosphere are entrained by the larger mass of removed material, resulting in the formation of a west-dipping craton margin geometry. By 80 Ma, continued upwelling and subsequent deposition of the entrained material smooths the craton margin to a steep (45-75°) angle. This process is repeated, resulting in the re-establishment of a westward dipping craton margin at 100 Ma. The recurrent formation of a west-dipping craton margin observed in the models implies that the westward dipping geometry of the craton margin observed in seismic tomography models of western Canada could represent a “snap-shot” of a dynamic process occurring at the Cordillera-craton boundary.

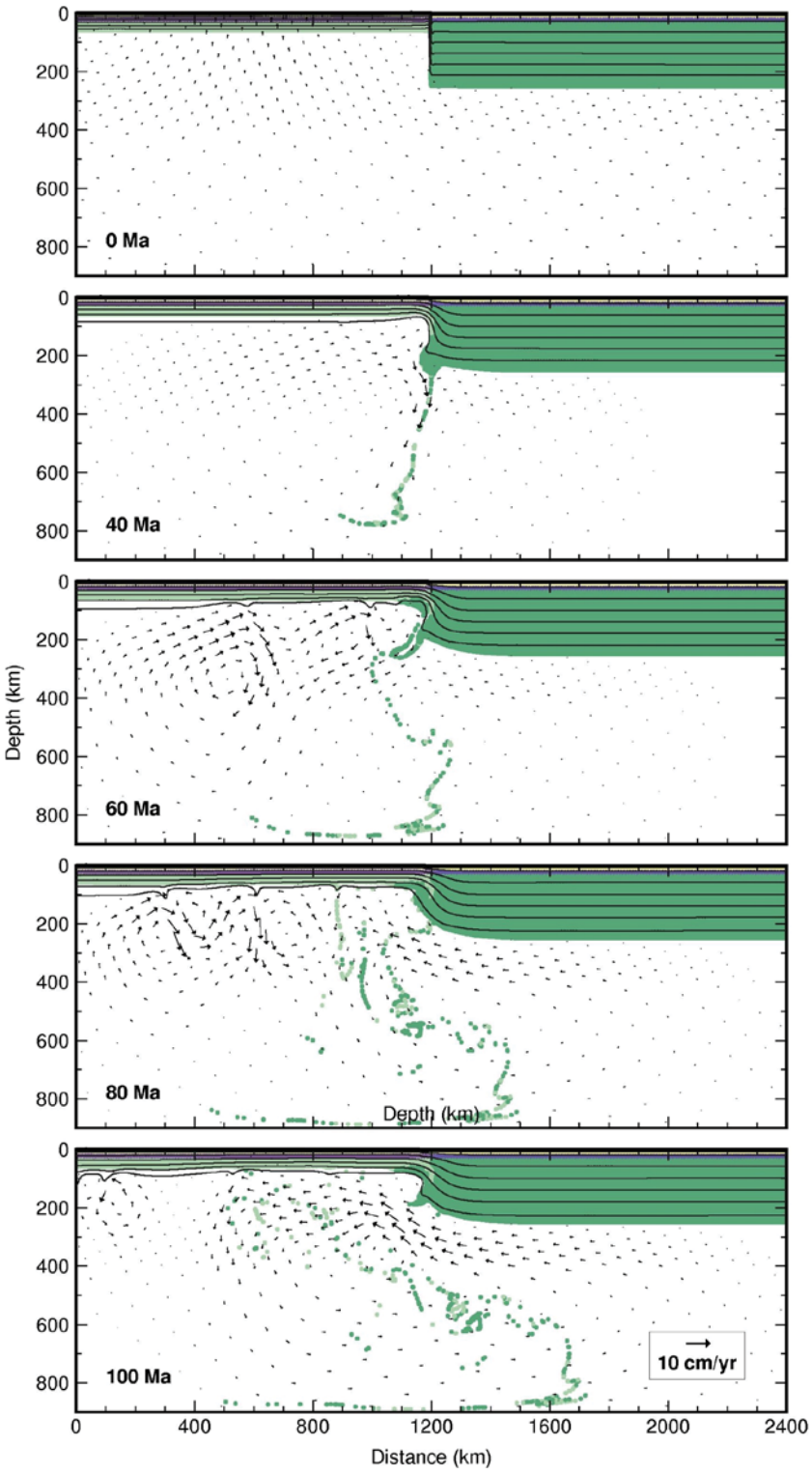

Figure 5.2: An example of the transient nature of west dipping craton margins observed in some of the numerical models, see text for discussion.

The model results in Section 4.5 (Figures 4.9 and 4.10) show that under the influence of large scale mantle flow (i.e. mantle wind), westward-dipping or vertical geometry of the craton margin can either be enhanced or diminished. In general, mantle wind velocities greater than 2 cm/yr result in basal shearing of the craton lithosphere and has a greater influence on the evolution of the margin than gravitational instability. Thus, higher velocity mantle flow tends to narrow the range of modelled strength and density combinations over which vertical and west-dipping craton margins are observed. However, Figure 4.9 suggests that vertical geometries may be more susceptible to erosion by increasing mantle wind velocity than west-dipping craton margin geometries. A possible explanation for this observation is that the density and strength contrasts that best resist shearing, and thus preserve the craton margin, appear to overlap with those that produce west-dipping craton margin geometries (i.e. buoyant, strong mantle lithosphere).

Although the speed of mantle wind velocity does affect the evolution of craton margin, a comparison of Figure 4.9 and Figure 4.10 shows that the geometry of the craton margin is much more strongly dependent on the flow direction. Overall, a westward flowing mantle wind enhances the formation of a west-ward dipping craton margin; as material flows from a region of thick to thin lithosphere, the thickness of mantle lithosphere helps shield the craton margin. Conversely, an eastward flowing mantle wind highly intensifies erosion of the craton margin, as the entire craton margin is exposed to erosion by mantle flow, and any material removed from the craton edge is carried and re-deposited eastward along the base of the craton mantle lithosphere.

Studies of seismic anisotropy offer conflicting views of mantle flow below western Canada; some authors argue for westward flow [*Conrad et al.*, 2004], some argue for eastward

flow [*Silver and Holt*, 2002; *Eaton and Frederiksen*, 2007], and others argue for changing flow direction with depth [*Yuan et al.*, 2011]. There is similar disagreement for estimates of flow velocity, with estimates as low as ~0.2-0.5 cm/yr [*Eaton and Frederiksen*, 2007] to as high as ~5.5 cm/yr [*Silver and Holt*, 2002]. Despite the controversy, the model results presented here seemingly support either a westward mantle flow or a slow eastward flow of 2 cm/yr or less to facilitate the formation of west-dipping and vertical geometries observed at the margin North American craton.

The preliminary crustal shortening models presented in Section 4.5 suggest that crustal shortening alone is insufficient to produce a westward-dipping craton margin geometry. Only models which incorporate a significant zone of weakness that extends through strong upper crust (20 times the reference value) up to the Earth's surface were successful in producing a westward dipping craton margin and thrusting of the Cordillera crust over the craton. This result suggests that upper crustal strength is particularly important to explain observed over-thrusting of the Cordillera crust, and agrees with previous studies, that estimate that ~80% of the strength in the Cordillera lithosphere is derived from the upper crust [*Hardebol et al.*, 2013]. However, it should be noted that the crustal shortening models presented here are preliminary; therefore, more testing is required to determine the effects of increased buoyancy in the craton mantle lithosphere.

In summary, geophysical observations have led to wide recognition that the mantle lithosphere below western Canada dramatically thickens from west to east by ~150-200 km across the Cordillera-craton boundary and that the transition from thin to thick lithosphere is extremely abrupt, occurring over a lateral distance of ~100 km [*Clowes et al.*, 2005; *Mercier et al.*, 2009; *Bao et al.*, 2014]. Additionally, new seismic tomography models from *Chen et al.*

[submitted manuscript, 2016] suggest that the geometry of the craton margin also shows along-strike variation. indicating that the geometry of the craton margin changes from steeply east-dipping at latitudes north of 53°N to west dipping between ~48-51°N, with a transition occurring between ~52-53°N, where the craton margin is approximately vertical (Figure 1.2). The geodynamic models of this study show that formation of a west-dipping craton margin is possible under a limited range of conditions, where the craton geometry evolves from vertical to west-dipping due to a variety of geodynamic processes, such as thermal convection, large-scale mantle flow. However, the development of a westward dipping craton margin requires thermal, rheological, and (perhaps to a lesser degree) density contrasts between the craton mantle lithosphere and the surrounding mantle. Namely, the craton mantle lithosphere must be stronger than the surrounding mantle by at least a factor of 5 and ~30 kg/m^3 less dense Furthermore, the models imply that a west-dipping craton margin can be either a long-lived feature, persisting over time scales greater than 50 Ma, or a transient feature, resulting from the removal and entrainment of cold cratonic mantle lithosphere in response to thermally-induced gravitational instability.

Chapter 6: Conclusions

Motivated by new geophysical observations from western Canada which suggest the craton margin dips westward below the southern Canadian Cordillera, this study had three main objectives: 1) to investigate the effects of geodynamic processes on the evolution of craton margin geometry; 2) to determine the rheological and compositional parameters required for the formation of a west-dipping craton margin; and 3) to establish whether or not such a feature is transient or long-lived. To do this, the finite element code SOPALE was used to numerically model the dynamical evolution of a 190 km step in mantle lithosphere thickness. The models explore how contrasting thermal regimes, rheologies and densities across the lithosphere step influence the geometry of the craton margin, and its evolution over 200 Ma of model time. Additionally, velocity boundary conditions imposed on the models investigate the effects of dynamic processes such as large-scale mantle flow and crustal shortening. Several conclusions can be drawn from the results of the model experiments:

1. In general, the models evolve toward an eastward dipping geometry due to erosion by gravitational instabilities. However, highly strong craton mantle lithosphere (approximately 15 to 20 times stronger than the surrounding mantle) can maintain a vertical craton margin, even in the absence of highly buoyant mantle lithosphere (i.e. ~10-20 kg/m^3 less than the surrounding mantle).
2. Owing to the thermal contrast between the hot mantle lithosphere of the Cordillera and the adjacent cold mantle lithosphere of the North American craton, craton mantle lithosphere that is at least 5 times stronger and ~30-40 kg/m^3 less dense than the surrounding mantle is required for the development of a westward dipping geometry at

the craton margin. This particular range of strength and density contrasts between the craton and the sub-lithospheric mantle provide a necessary balance between buoyancy and strength that prevents erosion of the craton margin by gravitational instability but is not so strong that no deformation occurs (i.e. boundary remains vertical).

3. Large-scale mantle flow, caused by relative motion between the continent and underlying mantle, can enhance both the formation and erosion of vertical and west-dipping craton margins. The response of the craton margin to imposed mantle wind suggests a greater sensitivity to the direction of mantle flow, compared to velocity. Perhaps unsurprisingly, mantle wind that flows from the interior of the craton toward the margin enhances and preserves vertical and west-dipping craton margins, whereas mantle wind that flows from the Cordillera toward the craton enhances erosion of the margin.
4. Preliminary models of crustal shortening suggest a zone of weakness which extends from the upper mantle up to the Earth's surface is required for thrusting of the Cordillera crust over the craton, and for the development of a vertical to shallowly (<110°) westward dipping craton margin.

The results of the numerical models presented in this study show promising agreement with geophysical observations from western Canada and offer insight into the evolution of craton margins in general. However, future work is required to investigate other important processes and observations that are not incorporated in the models for this study. For example, the models use a constant crustal thickness across the Cordillera-craton boundary; as discussed in Section 2.2, the crust thickens across the boundary by ~10 km, which may have an effect on the model results, particularly for crustal shortening models. Furthermore, tests should be conducted for mantle lithosphere that is layered (i.e. varying density and strength with depth), which has been

proposed for western Canada [*Griffin et al.*, 2004]. Surface processes, such as erosion and deposition, are not included in the models but may be important to processes occurring within the lithosphere [*Cloetingh et al.*, 2005]. It has been suggested that large-scale mantle flow may change direction with depth, as well as laterally across the Cordillera-craton boundary [*Yuan and Romanowicz*, 2010a, 2010b]; testing such variation in mantle flow could provide additional insight into observations from seismic anisotropy.

It is also important to assess the models relative to geophysical observations. Although the craton margin geometries resulting from geodynamic models show good qualitative agreement with the seismic tomography models of *Chen et al.* [submitted manuscript, 2016] (Figure 1.1) and the electrical conductivity models of *Rippe et al.* [2013] (Figure 1.2), a detailed quantitative comparison can not be made between these data sets. Conversion of the thermal model output to seismic velocity and electrical conductivity would allow for direct comparison between the geodynamic models of this study, the seismic tomography models and the electrical conductivity, and therefore further enrich our understanding of mantle lithosphere dynamics of western Canada.

References

Bao, X., D. W. Eaton, and B. Guest (2014), Plateau uplift in western Canada caused by lithospheric delamination along a craton edge, *Nat. Geosci.*, *7*(11), 830–833, doi:10.1038/ngeo2270.

Bao, X., D. W. Eaton, and Y. J. Gu (2016), Rayleigh wave azimuthally anisotropic phase velocity maps beneath western Canada, *J. Geophys. Res. Solid Earth*, (121), 1821–1834, doi:10.1002/2015JB012453.

Beaumont, C., and S. J. Ings (2012), Effect of depleted continental lithosphere counterflow and inherited crustal weakness on rifting of the continental lithosphere: General results, *J. Geophys. Res. Solid Earth*, *117*(8), 1–25, doi:10.1029/2012JB009203.

Beaumont, C., S. Ellis, J. Hamilton, and P. Fullsack (1996), Mechanical model for subduction-collision tectonics of Alpine-type compressional orogens, *Geology*, *24*(8), 675–678, doi:10.1130/0091-7613(1996)024<0675:MMFSCT>2.3.CO.

Beaumont, C., M. H. Nguyen, R. A. Jamieson, and S. Ellis (2006), Crustal flow modes in large hot orogens, *Geol. Soc. London, Spec. Publ.*, *268*(1), 91–145, doi:10.1144/GSL.SP.2006.268.01.05.

Bedle, H., and S. Van Der Lee (2009), S velocity variations beneath North America, *J. Geophys. Res. Solid Earth*, *114*(7), doi:10.1029/2008JB005949.

Bernstein, S., P. B. Kelemen, and K. Hanghoj (2007), Consistent olivine Mg# in cratonic mantle reflects Archean mantle melting to the exhauston of orthopyroxene, *Geology*, *35*(5), 459–462, doi:10.1130/G23336A.1.

Bouzidi, Y., D. R. Schmitt, R. A. Burwash, and E. R. Kanasewich (2002), Depth migration of deep seismic reflection profiles: crustal thickness variations in Alberta, *Can. J. Earth Sci.*, *39*(3), 331–350, doi:10.1139/e01-080.

Bürgmann, R., and G. Dresen (2008), Rheology of the Lower Crust and Upper Mantle: Evidence from Rock Mechanics, Geodesy, and Field Observations, *Annu. Rev. Earth Planet. Sci.*, *36*(1), 531–567, doi:10.1146/annurev.earth.36.031207.124326.

Cammarano, F., S. Goes, P. Vacher, and D. Giardini (2003), Inferring upper-mantle temperatures from seismic velocities, *Phys. Earth Planet. Inter.*, *138*(3–4), 197–222, doi:10.1016/S0031-9201(03)00156-0.

Cloetingh, S., P. A. Ziegler, F. Beekman, P. A. M. Andriessen, L. Matenco, G. Bada, D. Garcia-Castellanos, N. Hardebol, P. Dèzes, and D. Sokoutis (2005), Lithospheric memory, state of stress and rheology: Neotectonic controls on Europe's intraplate continental topography, *Quat. Sci. Rev.*, *24*(3–4 SPEC. ISS.), 241–304, doi:10.1016/j.quascirev.2004.06.015.

Clowes, R. M., M. J. A. Burianyk, A. R. Gorman, and E. R. Kanasewich (2002), Crustal velocity structure from SAREX, the Southern Alberta Refraction Experiment, *Can. J. Earth Sci.*, *39*(3), 351–373, doi:10.1139/e01-070.

Clowes, R. M., P. T. C. Hammer, G. Fernández-viejo, and J. K. Welford (2005), Lithospheric structure in northwestern Canada from Lithoprobe seismic refraction and related studies: a synthesis, *Can. J. Earth Sci.*, *42*(6), 1277–1293, doi:10.1139/e04-069.

Conrad, C. P., C. Lithgow-Bertelloni, and K. E. Louden (2004), Iceland, the Farallon slab, and dynamic topography of the North Atlantic, *Geology*, *32*(3), 177–180, doi:10.1130/G20137.1.

Cook, F. A., and P. Erdmer (2005), An 1800 km cross section of the lithosphere through the northwestern North American plate: lessons from 4.0 billion years of Earth's history, *Can. J. Earth Sci.*, *42*(6), 1295–1311, doi:10.1139/e04-106.

Courtier, A. M., J. B. Gaherty, J. Revenaugh, M. G. Bostock, and E. J. Garnero (2010), Seismic anisotropy associated with continental lithosphere accretion beneath the CANOE array, Northwestern Canada, *Geology*, *38*(10), 887–890, doi:10.1130/G31120.1.

Currie, C. A., and R. D. Hyndman (2006), The thermal structure of subduction zone back arcs, *J. Geophys. Res. Solid Earth*, *111*(8), 1–22, doi:10.1029/2005JB004024.

Currie, C. A., and J. van Wijk (2016), How craton margins are preserved: Insights from geodynamic models, *J. Geodyn.*, *100*(780), 144–158, doi:10.1016/j.jog.2016.03.015.

Currie, C. A., J. F. Cassidy, R. D. Hyndman, and M. G. Bostock (2004), Shear wave anisotropy beneath the Cascadia subduction zone and western North American craton, *Geophys. J. Int.*, *157*(1), 341–353, doi:10.1111/j.1365-246X.2004.02175.x.

Dickinson, W. R. (2004), Evolution of the North American Cordillera, *Annu. Rev. Earth Planet. Sci.*, *32*(1), 13–45, doi:10.1146/annurev.earth.32.101802.120257.

Dickinson, W. R. (2009), Anatomy and global context of the North American Cordillera, *Geol. Soc. Am. Mem.*, *1204*(1), 1–29, doi:10.1130/2009.1204(01).

Duarte, F., R. Gormaz, and S. Natesan (2004), Arbitrary Lagrangian-Eulerian method for Navier-Stokes equations with moving boundaries, *Comput. Methods Appl. Mech. Eng.*, *193*(45–47), 4819–4836, doi:10.1016/j.cma.2004.05.003.

Eaton, D. W., and A. Frederiksen (2007), Seismic evidence for convection-driven motion of the North American plate., *Nature*, *446*(7134), 428–431, doi:10.1038/nature05675.

Evenchick, C. (2007), A synthesis of the Jurassic–Cretaceous tectonic evolution of the central and southeastern Canadian Cordillera: Exploring links across the orogen, *Geol. Soc. Am. Spec. Pap.*, *433*(6), 117–145, doi:10.1130/2007.2433(06).

Frederiksen, A. W., M. G. Bostock, and J. F. Cassidy (2001), S-wave velocity structure of the Canadian upper mantle, *Phys. Earth Planet. Inter.*, *124*(3–4), 175–191, doi:10.1016/S0031-9201(01)00194-7.

Fullsack, P. (1995), An arbitrary Lagrangian-Eulerian formulation for creeping flows and its application in tectonic models, *Geophys. J. Int.*, *120*, 1–23, doi:10.1111/j.1365-246X.1995.tb05908.x.

Gerya, T. (2010), *Introduction to Numerical Geodynamic Modelling*, First Edit., Cambridge University Press, New York.

Gleason, G. C., and J. Tullis (1995), A flow law for dislocation creep of quartz aggregates determined with the molten salt cell, *Tectonophysics*, *247*(1–4), 1–23, doi:10.1016/0040-1951(95)00011-B.

Goes, S., and S. Van Der Lee (2002), Thermal structure of the North American uppermost mantle inferred from seismic tomography, *J. Geophys. Res.*, *107*(B3), 2050, doi:10.1029/2000JB000049.

Gorman, A. R. et al. (2002), Deep Probe: imaging the roots of western North America, *Can. J. Earth Sci.*, *39*(3), 375–398, doi:10.1139/e01-064.

Griffin, W. L., S. Y. O'Reilly, B. J. Doyle, N. J. Pearson, H. Coopersmith, K. Kivi, V. Malkovets, and N. Pokhilenko (2004), Lithosphere mapping beneath the North American plate, *Lithos*, *77*(1–4 SPEC. ISS.), 873–922, doi:10.1016/j.lithos.2004.03.034.

Gu, Y. J., and L. Shen (2015), Noise correlation tomography of Southwest Western Canada Sedimentary Basin, *Geophys. J. Int.*, *202*(1), 142–162, doi:10.1093/gji/ggv100.

Gu, Y. J., A. Okeler, L. Shen, and S. Contenti (2011), The Canadian Rockies and Alberta Network (CRANE): New constraints on the Rockies and Western Canada Sedimentary Basin, *Seismol. Res. Lett.*, *82*(4), 575–588, doi:10.1785/gssrl.82.4.575.

Hammer, P., and R. M. Clowes (2007), Lithospheric-scale structures across the Alaskan and Canadian Cordillera: Comparisons and tectonic implications, *GSA Spec. Pap.*, *i*(5), 99–116, doi:10.1130/2007.2433(05).

Hammer, P. T. C., R. M. Clowes, F. a. Cook, A. J. van der Velden, and K. Vasudevan (2010), The Lithoprobe trans-continental lithospheric cross sections: imaging the internal structure of the North American continent, *Can. J. Earth Sci.*, *47*(5), 821–857, doi:10.1139/E10-036.

Hardebol, N. J., R. N. Pysklywec, and R. Stephenson (2012), Small-scale convection at a continental back-arc to craton transition: Application to the southern Canadian Cordillera, *J. Geophys. Res. Solid Earth*, *117*(1), 1–18, doi:10.1029/2011JB008431.

Hardebol, N. J., F. Beekman, and S. A. P. L. Cloetingh (2013), Strong lateral strength contrasts in the mantle lithosphere of continents: A case study from the hot SW Canadian Cordillera, *Tectonophysics*, *602*, 87–105, doi:10.1016/j.tecto.2013.03.002.

Hieronymus, C. F., Z. H. Shomali, and L. B. Pedersen (2007), A dynamical model for generating sharp seismic velocity contrasts underneath continents: Application to the Sorgenfrei-Tornquist Zone, *Earth Planet. Sci. Lett.*, *262*(1–2), 77–91, doi:10.1016/j.epsl.2007.07.043.

Hirth, G., and D. L. Kohlstedt (2003), Rheology of the Upper Mantle and the Mantle Wedge: A View from the Experimentalists, in *Inside the Subduction Factory*, edited by J. Eiler, American Geophysical Union : Washington, DC, United States.

Hirth, G., R. L. Evans, and A. D. Chave (2000), Comparison of continental and oceanic mantle

electrical conductivity: Is the Archean lithosphere dry?, *Geochemistry, Geophys. Geosystems*, *1*(12), 2000GC000048, doi:10.1029/2000GC000048.

Hope, J., and D. Eaton (2002), Crustal structure beneath the Western Canada Sedimentary Basin: constraints from gravity and magnetic modelling, *Can. J. Earth Sci.*, *39*(3), 291–312, doi:10.1139/e01-060.

Hope, J., D. W. Eaton, and G. M. Ross (1999), Lithoprobe seismic transect of the Alberta Basin: Compilation and overview, *Bull. Can. Pet. Geol.*, *47*(4), 331–345.

Huismans, R. S., and C. Beaumont (2003), Symmetric and asymmetric lithospheric extension: Relative effects of frictional-plastic and viscous strain softening, *J. Geophys. Res.*, *108*(B10), 2496, doi:10.1029/2002JB002026.

Hyndman, R. D. (2010), The consequences of Canadian Cordillera thermal regime in recent tectonics and elevation: A review, *Can. J. Earth Sci.*, *47*(5), 621–632, doi:10.1139/E10-016.

Hyndman, R. D. (2015), Tectonics and structure of the queen charlotte fault zone, Haida Gwaii, and large thrust earthquakes, *Bull. Seismol. Soc. Am.*, *105*(2B), 1058–1075, doi:10.1785/0120140181.

Hyndman, R. D., and C. A. Currie (2011), Why is the North America Cordillera high? Hot backarcs, thermal isostasy, and mountain belts, *Geology*, *39*(8), 783–786, doi:10.1130/G31998.1.

Hyndman, R. D., and T. J. Lewis (1999), Geophysical consequences of the Cordillera-Craton thermal transition in southwestern Canada, *Tectonophysics*, *306*(3–4), 397–422, doi:10.1016/S0040-1951(99)00068-2.

Hyndman, R. D., C. A. Currie, and S. P. Mazzotti (2005), Subduction zone backarcs, mobile belts, and orogenic heat, *GSA Today*, *15*(2), 4–10, doi:10:1130/1052-5173(2005)015.

Hyndman, R. D., C. A. Currie, S. Mazzotti, and A. Frederiksen (2009), Temperature control of continental lithosphere elastic thickness, Te vs Vs, *Earth Planet. Sci. Lett.*, *277*(3–4), 539–548, doi:10.1016/j.epsl.2008.11.023.

Kao, H., Y. Behr, C. A. Currie, R. Hyndman, J. Townend, F. C. Lin, M. H. Ritzwoller, S. J. Shan, and J. He (2013), Ambient seismic noise tomography of Canada and adjacent regions: Part I. Crustal structures, *J. Geophys. Res. Solid Earth*, *118*(May), 5865–5887, doi:10.1002/2013JB010535.

Karato, S. I. (2010), Rheology of the deep upper mantle and its implications for the preservation of the continental roots: A review, *Tectonophysics*, *481*(1–4), 82–98, doi:10.1016/j.tecto.2009.04.011.

Karato, S. I., and P. Wu (1993), Rheology of the Upper Mantle: A Synthesis, *Science (80-.).*, *260*(5109), 771–778, doi:10.1126/science.260.5109.771.

King, S. D., and D. L. Anderson (1998), Edge-driven convection, *Earth Planet. Sci. Lett.*, *160*(3–4), 289–296, doi:10.1016/S0012-821X(98)00089-2.

Lenardic, A. (2003), Longevity and stability of cratonic lithosphere: Insights from numerical simulations of coupled mantle convection and continental tectonics, *J. Geophys. Res.*, *108*(B6), 2303, doi:10.1029/2002JB001859.

Lenardic, A., L. Moresi, and H. Muhlhaus (2000), The role of mobile belts for the longevity of deep cratonic lithosphere: The crumple zone model, *Geophys. Res. Lett.*, *27*(8), 1235–1238.

Mackwell, S. J., M. E. Zimmerman, and D. L. Kohlstedt (1998), High-temperature deformation of dry diabase with application to tectonics on Venus, *J. Geophys. Res. Solid Earth*, *103*(B1), 975–984, doi:10.1029/97JB02671.

Malvern, L. E. (1969), *Introduction to the mechanics of a continuous medium*, Prentice-Hall, Inc., Englewood Cliffs, N.J.

McClelland, W. C., and J. S. Oldow (2004), Displacement transfer between thick- and thin-skinned décollement systems in the central North American Cordillera, *Geol. Soc. London, Spec. Publ.*, *227*(1), 177–195, doi:10.1144/GSL.SP.2004.227.01.10.

Mercier, J. P., M. G. Bostock, J. F. Cassidy, K. Dueker, J. B. Gaherty, E. J. Garnero, J. Revenaugh, and G. Zandt (2009), Body-wave tomography of western Canada, *Tectonophysics*, *475*(3–4), 480–492, doi:10.1016/j.tecto.2009.05.030.

Monger, J., and R. Price (2002), The Canadian Cordillera : Geology and tectonic evolution, *CGES Rec.*, *27*(2), 17–36, doi:10.13140/2.1.4483.1520.

Moresi, L., and V. Solomatov (1998), Mantle convection with a brittle lithosphere: throughts on the global tectonic styles of the Earth and Venus, *Geophys. J. Int.*, *133*(3), 669–682, doi:10.1046/j.1365-246X.1998.00521.x.

Poudjom Djomani, Y. H., S. Y. O'Reilly, W. L. Griffin, and P. Morgan (2001), The density structure of subcontinental lithosphere through time, *Earth Planet. Sci. Lett.*, *184*(3–4), 605–621, doi:10.1016/S0012-821X(00)00362-9.

Poudjom Djomani, Y. H., W. L. Griffin, S. Y. O'Reilly, B. J. Doyle, Y. H. Poudjom Djomani, W. L. Griffin, S. Y. O'Reilly, and B. J. Doyle (2005), Lithospheric domains and controls on kimberlite emplacement, Slave Province, Canada: Evidence from elastic thickness and upper mantle composition, *Geochemistry, Geophys. Geosystems*, *6*(10), doi:10.1029/2005GC000978.

Pysklywec, R. N., O. Gogus, J. Percival, A. R. Cruden, and C. Beaumont (2010a), Insights from geodynamical modeling on possible fates of continental mantle lithosphere: collision, removal, and overturn, *Can. J. Earth Sci.*, *47*(4), 541–563, doi:10.1139/E09-043.

Pysklywec, R. N., S. M. Ellis, and A. R. Gorman (2010b), Three-dimensional mantle lithosphere deformation at collisional plate boundaries: A subduction scissor across the South Island of New Zealand, *Earth Planet. Sci. Lett.*, *289*(3–4), 334–346, doi:10.1016/j.epsl.2009.11.022.

Ross, G. M. (2002), Evolution of Precambrian continental lithosphere in Western Canada: results from Lithoprobe studies in Alberta and beyond, *Can. J. Earth Sci.*, *39*(3), 413–437, doi:10.1139/e02-012.

Ross, G. M., R. R. Parrish, M. E. Villeneuve, and S. A. Bowring (1991), Geophysics and geochronology of the crystalline basement of the Alberta Basin, western Canada, *Can. J. Earth Sci.*, *28*(4), 512–522, doi:10.1139/e91-045.

Ross, G. M., J. Broome, and W. Miles (1994), Potential fields and basement structure, *atlas West. Canada Sediment. Basin*, 41–47.

Ross, G. M., D. W. Eaton, D. E. Boerner, and W. Miles (2000), Tectonic entrapment and its role in the evolution of continental lithosphere: An example from the Precambrian of western Canada, *Tectonics*, *19*(1), 116, doi:10.1029/1999TC900047.

Salters, V. J. M., and A. Stracke (2004), Composition of the depleted mantle, *Geochemistry, Geophys. Geosystems*, *5*(5), doi:10.1029/2003GC000597.

Savage, M. K. (1999), Seismic anisotropy and mantle deformation: what have we learnt from shear wave splitting?, *Rev. Geophys.*, *37*(98), 65–106.

Shapiro, S. S., B. H. Hager, and T. H. Jordan (1999), Stability and dynamics of the continental tectosphere, *Lithos*, *48*(1–4), 115–133, doi:10.1016/S0419-0254(99)80008-1.

Silver, P. G., and W. E. Holt (2002), The mantle flow field beneath western North America., *Science*, *295*(5557), 1054–1057, doi:10.1126/science.1066878.

Simony, P. S., and S. D. Carr (2011), Cretaceous to Eocene evolution of the southeastern Canadian Cordillera: Continuity of Rocky Mountain thrust systems with zones of "in-sequence" mid-crustal flow, *J. Struct. Geol.*, *33*(9), 1417–1434, doi:10.1016/j.jsg.2011.06.001.

Tréhu, A. M., M. Scheidhauer, K. M. M. Rohr, B. Tikoff, M. A. L. Walton, S. P. S. Gulick, and E. C. Roland (2015), An abrupt transition in the mechanical response of the upper crust to transpression along the queen charlotte fault, *Bull. Seismol. Soc. Am.*, *105*(2B), 1114–1128, doi:10.1785/0120140159.

Wang, H., J. van Hunen, D. G. Pearson, and M. B. Allen (2014), Craton stability and longevity: The roles of composition-dependent rheology and buoyancy, *Earth Planet. Sci. Lett.*, *391*, 224–233, doi:10.1016/j.epsl.2014.01.038.

Wang, Q. (2010), A review of water contents and ductile deformation mechanisms of olivine: Implications for the lithosphere-asthenosphere boundary of continents, *Lithos*, *120*(1–2), 30–41, doi:10.1016/j.lithos.2010.05.010.

van Wijk, J., J. van Hunen, and S. Goes (2008), Small-scale convection during continental rifting: Evidence from the Rio Grande rift, *Geology*, *36*(7), 575–578, doi:10.1130/G24691A.1.

van Wijk, J. W., W. S. Baldridge, J. van Hunen, S. Goes, R. Aster, D. D. Coblentz, S. P. Grand, and J. Ni (2010), Small-scale convection at the edge of the Colorado Plateau: Implications for topography, magmatism, and evolution of Proterozoic lithosphere, *Geology*, *38*(7), 611–614, doi:10.1130/G31031.1.

Wyld, S. J., P. J. Umhoefer, and J. E. Wright (2006), Reconstructing northern Cordilleran terranes along known Cretaceous and Cenozoic strike-slip faults : Implications for the Baja British Columbia hypothesis and other models, in *Paleogeography of the North American Cordillera: Evidence For and Against Large-Scale Displacements*, edited by J. W. Haggart, R. J. Enkin, and J. W. . Monger, pp. 277–298, Geological Association of Canada, Special Paper 46, Toronto, ON.

Yuan, H., and B. Romanowicz (2010a), Depth dependent azimuthal anisotropy in the western US upper mantle, *Earth Planet. Sci. Lett.*, *300*(3–4), 385–394, doi:10.1016/j.epsl.2010.10.020.

Yuan, H., and B. Romanowicz (2010b), Lithospheric layering in the North American craton., *Nature*, *466*(7310), 1063–1068, doi:10.1038/nature09332.

Yuan, H., B. Romanowicz, K. M. Fischer, and D. Abt (2011), 3-D shear wave radially and azimuthally anisotropic velocity model of the North American upper mantle, *Geophys. J. Int.*, *184*(3), 1237–1260, doi:10.1111/j.1365-246X.2010.04901.x.